A TECHNICAL FRAMEWORK FOR GROUP STUDIES OF DIFFUSION TENSOR IMAGING

A THESIS SUBMITTED TO
THE GRADUATE SCHOOL OF INFORMATICS OF
MIDDLE EAST TECHNICAL UNIVERSITY

BY

MEHMET ÖZER METİN

IN PARTIAL FULFILLMENT OF THE REQUIREMENTS
FOR
THE DEGREE OF DOCTOR OF PHILOSOPHY
IN
MEDICAL INFORMATICS

AUGUST 2022

Approval of the thesis:

A TECHNICAL FRAMEWORK FOR GROUP STUDIES OF DIFFUSION TENSOR IMAGING

Submitted by Mehmet Özer Metin in partial fulfillment of the requirements for the degree of **Doctor of Philosophy in Health Informatics Department, Middle East Technical University** by,

Date: 23/08/2022

I hereby declare that all information in this document has been obtained and presented in accordance with academic rules and ethical conduct. I also declare that, as required by these rules and conduct, I have fully cited and referenced all material and results that are not original to this work.

Name, Last name : Mehmet Özer Metin

Signature

ABSTRACT

A TECHNICAL FRAMEWORK FOR GROUP STUDIES OF DIFFUSION TENSOR IMAGING

Metin, Mehmet Özer
Ph.D., Department of Health Informatics
Supervisor: Assoc. Prof. Dr. Yeşim Aydın Son
Co-Advisor: Assoc. Prof. Dr. Didem Gökçay

August 2022, 120 pages

Diffusion tensor imaging (DTI) is an ideal tool to investigate white matter abnormalities. In this study, novel techniques that use non-scalar metrics have been proposed for group-based DTI analysis. Utilization of directional statistics to evaluate group differences is the main achievement of this thesis. Directional statistics can encapsulate much more information than scalar metrics about the diffusion tensors extracted from groups of diffusion weighted images. We have introduced two new approaches to analyze group differences. The first method augments probabilistic fiber tractography with a new visualization technique to carry out group-based DTI analysis for connectivity-based hypothesis testing. Probabilistic fiber tractography is extended with a new method to visualize FA values versus arc-length. This method not only enables hypothesis testing of probabilistic tracts but also provides multi-resolution visualization. The second method introduces a new technique called tract profiling and directional statistics (TPDS). We have investigated different directional statistical models to find the best fit. During the experiments, we confirmed that carrying out directional statistical analysis along the tract is much more effective than voxel- or skeleton-guided directional statistics. As a case study, the method has been applied to identify connectivity differences of patients with major depressive disorder. The results obtained with the directional statistic-based analysis are consistent with those of

Network Based Statistics (NBS), but additionally, we found significant changes in the right hemisphere striatum, ACC, and prefrontal, parietal, temporal, and occipital connections as well as left hemispheric differences in the limbic areas such as the thalamus, amygdala, and hippocampus. Comparison with the output of the network-based statistical toolbox indicated that the benefit of the proposed method becomes much more distinctive as the tract length increases.

Keywords: Diffusion tensor imaging, group based dti analysis, directional statistics

ÖZ

GRUP ÇALIŞMALARI İÇİN DIFÜZYON TENSÖRÜ GÖRÜNTÜLEME ALTYAPISI

Metin, Mehmet Özer
Doktora Lisans, Sağlık Bilişimi Bölümü
Tez Yöneticisi: Doç. Dr. Yeşim Aydın Son
Tez Eş-Danışmanı: Doç. Dr. Didem Gökçay

Ağustos 2022, 120 sayfa

Difüzyon tensör görüntüleme (DTI), beyaz cevher anormalliklerini araştırmak için ideal bir araçtır. Bu çalışmada, grup tabanlı DTI analizi için skaler olmayan metrikleri kullanan yeni teknikler önerilmiştir. Grup farklılıklarını değerlendirmek için yönlü istatistiklerin kullanılması bu tezin ana başarısıdır. Yönlü istatistikler, difüzyon ağırlıklı görüntü gruplarından çıkarılan difüzyon tensörleri hakkında skaler ölçümlerden çok daha fazla bilgiyi kapsayabilir. Grup farklılıklarını analiz etmek için iki yeni yaklaşım getirdik. İlk yöntem, bağlantı tabanlı hipotez testi için grup tabanlı DTI analizini gerçekleştirmek için yeni bir görselleştirme tekniği ile olasılıksal fiber traktografisini güçlendirir. Olasılıksal fiber traktografisi, yay uzunluğuna karşı FA değerlerini görselleştirmek için yeni bir yöntemle genişletildi. Bu yöntem, yalnızca olasılıklı yolların hipotez testini sağlamakla kalmaz, aynı zamanda çok çözünürlüklü görselleştirme sağlar. İkinci yöntem, yol profili oluşturma ve yön istatistikleri (TPDS) adı verilen yeni bir teknik sunar. En uygun olanı bulmak için farklı yönlü istatistiksel modelleri araştırdık. Deneyler sırasında, yol boyunca yönlü istatistiksel analiz yapmanın voksel veya iskelet kılavuzlu yönlü istatistiklerden çok daha etkili olduğunu doğruladık. Bir vaka çalışması olarak yöntem, majör depresif bozukluğu olan hastaların bağlantı farklılıklarını belirlemek için uygulanmıştır. Yönlü istatistik tabanlı analizle elde edilen sonuçlar, Ağ Tabanlı İstatistikler (NBS) ile tutarlıdır, ancak ek olarak, sağ hemisfer striatum, ACC ve

prefrontal, parietal, zamansal ve oksipital bağlantılarda önemli değişiklikler bulduk. talamus, amigdala ve hipokampus gibi limbik bölgelerdeki sol hemisferik farklılıklar. Ağ tabanlı istatistiksel araç kutusunun çıktısı ile karşılaştırma, önerilen yöntemin faydasının, yol uzunluğu arttıkça çok daha belirgin hale geldiğini göstermiştir.

Anahtar Sözcükler: difüzyon tensor görüntüleme, difüzyon görüntülemeyle grup analizi, yönsel istatistik

To my parents who devoted themselves to their children

ACKNOWLEDGMENTS

I would like to sincerely thank my co-advisor, Assoc. Prof. Dr. Didem Gökçay, for her guidance and support throughout this study. She never lost her confidence in me and patiently helped me all these years to complete my thesis. I also want to thank Prof. Dr. Gözde Ünal and Prof. Dr. Vilda Purutçuoğlu, for their technical guidance throughout the thesis follow-up meetings. I would also like to thank Assoc. Prof. Dr. Yeşim Aydın Son for administering my thesis submission processes due to a legal obligation mandated by the METU senate. Finally I thank Assist. Professors Dr. Burçak Otlu Sarıtaş and Dr. Hayriye Aktaş Dinçer for serving as members of my thesis committee. The comments and questions raised by all professors were very beneficial in the completion of the manuscript.

I appreciate METU (Middle East Technical University), and TUBITAK (Turkish National Science Foundation) for partially funding my studies through two research projects (Project numbers BAP-07-04-2012 and 109E081 for which Assoc. Prof. Dr. Gökçay was the principal investigator). I would also like to express my gratitude to Assoc. Prof. Bora Baskak from Ankara University, Prof. Ergin Atalay from Bilkent University and Dr. Zeynep Başgöze respectively for diagnosis of the MDD patients, data acquisition at the UMRAM center and data collection.

This thesis work is dedicated to my wife, Idil, who has been a constant source of support and encouragement during the challenges of my thesis studies and our lives. We got married during my studies, and now have been married for 12 years. When I look back over those years, I cannot believe what we have achieved together. Thank you for giving me two wonderful children who have made my life a heaven. I am truly thankful for having you in my life.

To my children, Nisan and Tamay, thank you both for your understanding when I was distracted or not fully present for you during this study. I believe we have many years ahead, and great times to spend together.

TABLE OF CONTENTS

PLAGIARISM iii
ABSTRACT iv
ÖZ vi
ACKNOWLEDGMENTS ix
TABLE OF CONTENTS x
LIST OF TABLES xiii
LIST OF FIGURES xiv
LIST OF ABBREVIATIONS xvii
CHAPTERS
1. INTRODUCTION 1
1.1. Scope of the Thesis 3
1.2. Outline of the Thesis 5
2. BACKGROUND AND RELATED WORK 7
2.1. Diffusion Tensor Imaging In Group Studies 7
2.1.1. ROI Based Studies 8
2.1.2. Voxel-Wise Comparison 9
2.1.3. Fiber Tract Analysis 14
2.1.4. Tensor Based Metrics and Statistics 18
2.1.4.1. Riemannian Framework for Tensor Computing 19
2.1.4.2. Log- Euclidean Metrics 20
2.1.5. Fiber Classification and Segmentation 22
2.2. Major Depression Disorder 25
2.2.1. Neuropathology of Major Depression Disorder 29
2.2.2. White Matter Abnormalities in Major Depression Disorder 31
2.2.3. DTI Studies of Major Depression Disorder 31
3. HISTOGRAM BASED GROUP ANALYSIS METHOD AND RESULTS 35
3.1. Method 35
3.1.1. Method Pipeline 35

3.2. Experiments and Results 41
3.2.1. Subjects and Data Acquisition 41
3.2.2. Results 41
4. TRACT PROFILING AND DIRECTIONAL STATISTICS METHOD AND RESULTS 47
4.1. Method 47
4.1.1. Directional Distributions and Parameter Estimates 48
4.1.1.1. Fisher Directional Statistics 48
4.1.1.2. Kent Distribution 49
4.1.1.3. Watson Distribution 50
4.1.1.4. Bingham Distribution 52
4.1.1.5. Parameter Estimation and Confidence Ellipse 53
4.1.2. Directional Statistic Distribution Fitting 54
4.1.2.1. Method Pipeline 54
4.1.2.2. Pre-processing Step 55
4.1.2.3. PDD Generation 55
4.1.2.4. Distribution Fitting 56
4.1.2.5. Probability Density Function Evaluation 56
4.1.2.6. Goodness of Fit Score (GoF) Evaluation 56
4.1.3. Tract Profiling and Directional Statistics 57
4.1.3.1. Pre Processing 57
4.1.3.2. Tract Profiling 58
4.1.3.2.1. Overlapping Fiber Calculation 59
4.1.3.2.2. Medial Line Generation 60
4.1.3.2.3. Calculations of Tract Cross Sections 63
4.1.3.3. Directional Statistics 63
4.2. Experiments and Results 65
4.2.1. Subjects 65
4.2.2. Data Acquisition 65
4.2.3. Directional Statistic Distribution Fitting 65
4.2.4. Pipeline 70
4.2.5. Results 75
4.2.5.1. Analysis of the Strengths of VBA, TBSS and TPDS in Tract Modeling 76

4.2.5.2. Analysis of the Group Difference Maps generated by NBS and TPDS 77
4.2.5.3. Comparison of VBA and TBSS with TPDS using Directional Statistics 78
4.2.5.4. Comparison of the Group Differences in Connectivity Maps Using Network Based Statistics and TPDS 80
5. CONCLUSION AND FUTURE WORK 83
5.1. Future Work 88
REFERENCES 89
APPENDICES 103
APPENDIX A. DIFFISION TENSOR IMAGING 103
APPENDIX B. B-SPLINE CURVES 118
APPENDIX C. SOURCE CODE AND INSTRUCTIONS 119
CURRICULUM VITAE 120

LIST OF TABLES

Table 1: Histogram based analysis of amygdala connections. 42
Table 2: GoF scores and ANOVA test results for ROI's. 70
Table 3: Region of interest areas. 75
Table 4: Comparison of VBA and TBSS with TPDS 79

LIST OF FIGURES

Figure 1: Different skeletonisation stages. 13
Figure 2: ALS analysis with TBSS 14
Figure 3: Algorithm for fiber tract-oriented statistics for quantitative diffusion tensor MRI analysis 16
Figure 4: Tract-based morphometry for white matter group analysis 17
Figure 5: Group analysis of fiber tract statistics 17
Figure 6: Goodlett parametrization of fiber tracts 18
Figure 7: Swelling effect of averaging tensors. 18
Figure 8: Riemannian metric 19
Figure 9: Basic standard operations in a Riemannian manifold 20
Figure 10: Differences of Euclidian and Riemannian metrics. 21
Figure 11: Interpolation differences between Riemannian and Log-Euclidian metrics 22
Figure 12: Regularization differences between Riemannian and Log-Euclidian metrics 22
Figure 13: Fiber clustering overview 23
Figure 14: Segmentation obtained from recursive bipartitioning of the fiber traces 24
Figure 15: The results of Maddah's algorithm for clustering 25
Figure 16: Anatomical circuits of mood disorders 26
Figure 17: Putative sources of MDD. 27
Figure 18: Mayberg's Model of Depression. 28
Figure 19: Corticolimbic-insular-striatal pallidal- thalamic circuitry for psychiatric disorders 29
Figure 20: ROI based MDD analysis 32
Figure 21: VBA and TBSS based MDD analysis 32
Figure 22: Overall pipeline 36
Figure 23: FA values that passes on the tracts. 38
Figure 24: 3d Histogram for fiber tracts of one subject 38

Figure 25: Heatmap for the same histogram in 2d. 39
Figure 26: Map for fiber tracts for each FA and fiber length match. 40
Figure 27: Map for p values for a connection histogram. 40
Figure 28: Amygdala connection graphs 41
Figure 29: Left amygdala with entorhinal cortex. 43
Figure 30: Left amygdala with temporal pole. 43
Figure 31: Left amygdala with insula. 44
Figure 32: Left amygdala with hippocampus. 44
Figure 33: Right amygdala with medial orbitofrontal. 45
Figure 34: Right amygdala with entorhinal cortex. 45
Figure 35: Right amygdala with putamen. 46
Figure 36: Right amygdala with hippocampus. 46
Figure 37: Watson Distribution. 51
Figure 38: Bingham Distribution. 52
Figure 39: Overall pipeline of pre processing method. 57
Figure 40: Cross sectional Tract bundle 59
Figure 41: Medial line of cross sectional area between 2 ROIs (green and purple) after pruning and b-spline curve fitting. 62
Figure 42: Principal diffusion directions in a cross-sectional profile area from only one subject. 63
Figure 43: Parameter Estimation and Confidence Ellipse. 64
Figure 44: PDD for ROI's. 67
Figure 45: Visualization of Fiber Tracts. 68
Figure 46: PDDs' in 2D view. 69
Figure 47: T1 image registration on DWI b0. 71
Figure 48: T2 image registration on DWI b0. 72
Figure 49: JHU white matter atlas. 72
Figure 50: JHU white matter atlas registered on subject's DWI bo image. 73
Figure 51: The white matter areas registered on T1 image. 73
Figure 52: JHU atlas white matter tracts and areas. 74
Figure 53: Gray matter areas registered on T1 image. 74
Figure 54: Comparison of VBA/TBSS with TPDS data processing pipeline. 76
Figure 55: Map of ROIS with statistically different connectivity between control and patient groups. 81

Figure 56: Scatter diagram of z-score of tract lengths versus significantly different clusters. 82

LIST OF ABBREVIATIONS

ACC	Anterior Cingulate Cortex
ADC	Apparent Diffusion Coefficient
ALS	Amyotrophic lateral sclerosis
AWS	Axonal Water Fraction
BET	Brain Extraction Tool
CLIPST	Striatal Pallidal- Thalamic circuitry
CSF	Cerebrospinal fluid
DICOM	Digital Imaging and Communications in Medicine
DLPFC	Dorsolateral prefrontal cortex
DTI	Diffusion tensor imaging
DWI	Diffusion Weighted Imaging
EM	Expectation Maximization
FA	Fractional Anisotropy
FMRI	Functional magnetic resonance imaging
FSL	FMRIB Software Library
FWHM	Full width at half maximum
GAP-43	Growth-associated Protein-43
GLM	Generalized linear model
GOF	Goodness of Fit Score
IRTK	Image Registration Toolkit
ITK	Insight Toolkit
LCSPT	Limbic–Cortical–Striatal–Pallidal–Thalamic
LTC	Limbic–Thalamo–Cortical
MD	median anisotropy
MDD	major depressive disorder
MT	Mean Tensors

NBS	Network Based Statistics
NMR	nuclear magnetic resonance
NRRD	Nearly Raw Raster Data
PCA	Principal Component Analysis
PD	Principal Directions
PDD	Principal Diffusion Direction
PET	positron emission tomography
ROI	regions of interest
SNR	Signal to Noise Ratio
TBM	Tract-Based Morphometry
TPDS	tract profiling and directional statistics
VBM	voxel based morphometry technique
VSC	Voxel Scale Connectivity
VTK	Visualization Toolkit
WM	White Matter

CHAPTER 1

INTRODUCTION

Solving connectivity of the brain can be the key to understand different patterns of brain structures. High-level brain functions require high-level of connectivity patterns and brain areas interact with each other through unique paths of execution. To identify these paths of execution, studying neural cells and their connection maps is insufficient. Although there are previous efforts, such as studies about primitive animals (e.g. Caenorhabditis Elegans for which the network of 302 neurons was completely charted using dissection and electron microscopy (Brenner 1973)), finding connectivity at the microscopic neuronal/axonal scale in the human brain is beyond this technology. A possible map of those connections will consist of 1016 edges and 1011 nodes (Hagmann et al. 2007). This kind of detailed information brings incomputable and mostly irrelevant information.

Functional connectivity is defined as combination of elements that builds a system, regardless of whether there exist direct structural links or connections (Sporns, 2007). Functional connectivity is related to patterns of time-series where different areas correlate in multiple different time scales. Directions or structural model of the components are not relevant in functional connectivity, it only captures statistical correlations or independence of different brain areas. Such analyses allow the characterization of neural interactions during particular cognitive or motor tasks. Functional networks are generated based on functional connectivity maps. FMRI and PET techniques map distinct spatial map distributions and connect temporally correlated brains regions (Poldrack and Sandak 2004).

Structural connectivity can be defined as synaptic connections of neurons or networks of physical pathways. The cerebral cortex can be represented as densely coupled clusters that are also globally interconnected. These brain regions can be correlated with other brain regions by analyzing network hubs. Structural connectivity is based on classification of those network hubs. Interpretation of such connectivity matrices based on connectivity patterns and network characteristics require large-scale connectivity analysis and mapping of cerebral cortex (Sporns et al., 2004).

In cases where global organization of brain structures is more important than the organization of a specific structure, connectivity analysis can provide the most

important source of knowledge. Development and aging studies are the most notable studies where functional and structural connectivity analysis can be of great importance. In addition, psychological diseases such as attention deficit hyperactivity disorder and depression are known to be related with many different areas of the brain. There are various hypotheses claiming that a disease condition is mostly caused by the connectivity pattern, not the specific structures. So in order to differentiate the pathogenesis and its underlying cause, connectivity analysis can be utilized.

On the other hand, connectivity analysis requires a robust metric to compare a disease state with a control state. Diffusion tensor imaging arise to be the only tool to understand white matter abnormalities that effects connectivity. It enables analyzing the white matter tissue structure, gives visibility regarding the geometry of major fiber bundles and quantitative information about it. One can measure diffusion characteristics such as tensor orientation, anisotropy etcetera (Goodlett et al. 2009). Since the self-diffusivity of water molecules depends on their local environment, tissue architecture can be identified by the diffusion tensors. Diffusibility metrics also enable group comparison to identify different clinical anomalies (Zhu et al. 2010).

White matter abnormalities can be studied by investigating how white matter tracts change. Statistically differentiated orientation and integrity of the tracts can show possible illnesses (Sexton, Mackay, and Ebmeier 2009). Basser et. al. (1994) defines diffusion tensor as the covariance matrix of diffusion coefficients. It can be calculated from the gradient directions of diffusion per voxel (Basser, Mattiello and Lebihan 1994). Here, diffusion tensor is non-scalar and represented as matrix. It also provides neural tract directional information and scalar descriptors such as FA: functional anisotropy, RA is standard deviation of the tensor eigenvalues normalized by Apparent Diffusion Coefficient (Basser and Pierpaoli, 2011). Both RA and FA represent the degree of anisotropy, whereas the trace of the diffusion tensor expresses overall diffusion magnitude (Alexander et al. 2007). MD is in fact average of the eigenvalues of the diffusion tensor (Alexander et al. 2007). Since these scalar metrics are just descriptors of the covariance matrix of diffusion coefficients, they do not contain information about the full tensor distribution. As a matrix descriptor, these scalar values can be computed from different eigenvalue combinations so one can not interpret the full representation of the tensor. Using only scalar values do not consider the information on diffusion directions.

The largest eigenvector of the tensor, principal diffusion direction (PDD), represents the main fiber direction within a specific voxel and it is assumed that the diffusion is restricted in any direction perpendicular to the nerve fibers (Le Bihan et al. 2001). PDD has been used mainly in Directionally Encoded Color (DEC) maps that only enable visual comparison at individual subject level (Pajevic and Pierpaoli 1999). Hence it is not suitable for quantitative group analysis. In order to evaluate PDD, which is a vector, statistics over vectors is needed.

Directional statistics is conducted on vectors and directions based on observations on compact Riemannian manifolds (Pennec 2006). Hence it can encapsulate much more information than scalar metrics about the diffusion. Without the limitation of scalar statistics, one can evaluate dispersion and coherence values among various populations, fit directional models to the data and perform hypothesis testing for group based studies.

In the literature, directional statistics have been used to characterize fiber orientation distribution functions to estimate fiber dispersion quantitatively via fanning and bending fiber geometries throughout the brain (Tariq et al. 2016) (Sotiropoulos, Behrens, and Jbabdi 2012). In addition, directional statistics have also been utilized to extract bundle specific metrics from crossing fiber models (Riffert et al. 2014) and fiber tractography (Parker, Haroon, and Wheeler-Kingshott 2003). However, Watson distribution, which has been used in previous directional statistics in group analysis contain limited parameters (Schwartzman, Dougherty, and Taylor 2005a) (Hutchinson et al. 2012). Watson distribution is a bi-modal probability distribution on a two-dimensional unit sphere S2 in R3 which is symmetrical around mean direction, where each direction and its negative have the same probability. In our previous study (Metin and Gökçay 2014), it has been shown that Bingham distribution better fits into PDD distributions for white matter tracts and improves the depiction of variability among subjects in anisotropic tensors areas, such as fiber crossings. This is because Bingham distribution is a generalization of Watson distribution: it is bi-modal and elliptic around mean direction.

1.1. Scope of the Thesis

The aim of this study is to propose new group analysis methods that deal with not only scalar metrics but also work in vector space. The first method that has been proposed is histogram based group analysis method. In this study, a group analysis method, has been developed based on diffusion imaging that uses connectivity as well as diffusibility information (fractional anisotropy). A fully automatic pipeline has been developed (Metin and Gokcay 2013).

The second method which is named as Track Profiling Directional Statistics (TPDS), proposes a new tract-based framework using directional information in diffusion tensors to improve statistical group analysis (Metin and Gokcay 2021). For this purpose, 1) we have generated a new data structure called tract profile by clustering fibers across subjects, 2) we have developed a method based on directional statistics to compare WM differences of different groups across each tract profile. In order to demonstrate the superiority of the proposed framework, we compared the tract profiling method with two widely used techniques, TBSS (Smith et al. 2006) and VBA (Van Hecke et al. 2009). Furthermore, we ran a third comparison with the Network Based Statistic (NBS) toolbox (Zalesky, Fornito, and Bullmore 2010) which utilizes non-parametric statistical testing to identify the

components of an NxN undirected connectivity matrix that differ significantly between two distinct populations.

Applications of these new methods are implemented on major depressive disorder (MDD). MDD is accounted as one of the first causes that lower the living standards (WHO, 2001). However the pathogenesis of it is not very well known (Drevets, Price and Furey 2008). Because pathological conditions are not likely to be associated with gross brain pathology, a controlled animal or human experiment environment is not possible, Noninvasive techniques are critical to discover connectivity patterns that relate to MDD (Drevets 2004).

To demonstrate the histogram based group analysis method, amygdala connections have been chosen for analysis. Since Amygdala is regarded as one of the most important structure that effects emotion, the connectivity analysis of Amygdala can be important discriminative factor that changes between MDD and control subjects. For MDD patients, it can be assumed that the pathways between Amygdala and neighboring structures will be affected. Histogram based group analysis method in this study could not be regarded as a distinct cut from other group analysis methods. However, connectivity based approach, analysis depends on not only FA values but also fiber tract lengths, which is addressed by the second method.

To demonstrate the strength of TPDS in identification of differences of structural connectivity in Major Depressive Disorder, a small data set (n=30) is used. Although depression has traditionally been viewed as an affective disorder, the last few decades of research have shown that MDD is also associated with considerable disturbances in cognitive functioning, including executive functions, attention, memory and psychomotor speed (McClintock et al. 2010) (Castaneda et al. 2008). In MDD, multidimensional, systems-level differences are reported in discrete, but functionally integrated pathways (Mayberg 2003). Therefore, differences in MDD can be expected to cover a wide range of WM tracts. So far, especially white matter disturbances and connectivity differences have been analyzed using DTI based analysis in MDD (McClintock et al. 2010; Kieseppä et al. 2010; Seminowicz et al. 2004; Zou et al. 2008; Cullen et al. 2010; Helm et al. 2018). Most of these studies state that loss of integrity occurs in the WM fiber tracts of the frontal, temporal, and cingulate cortex of MDD patients. White matter integrity can be described as biophysical white matter changes as a result of micro structural characteristic in both intra and extra axonal environments of WM such as axonal water fraction (AWF), intra-axonal diffusivity, extra-axonal axial and radial diffusivities. More specifically, reported abnormalities in the connectivity of the DLPFC, ACC circuits (Helm et al. 2018), as well as subcortical regions complement other findings specified in affective disorders (Sexton, Mackay, and Ebmeier 2009).

1.2. Outline of the Thesis

This thesis is organized as follows. The next chapter contains background information about group analysis studies in Diffusion Tensor Imaging. First, the metrics, the methods and pitfalls for group analysis using DTI are summarized. Furthermore, Major Depression Disorder and previous group analysis methods that use DTI for these disorders are described. In Chapter 3 and 4, the methods and the results that has been proposed and implemented have been presented. In Chapter 3 a novel method, histogram-based group analysis using DTI has been described and the results has been discussed. In Chapter 4, the main contribution of this thesis has been presented. Track based directional statistics (TPDS) method has been proposed and the implementation results has been discussed. In Chapter 5, further discussions, future work and conclusion has been presented. Background information about the basics of diffusion weighted imaging and diffusion tensor imaging is given in appendix A. B-spline curves has been described in appendix B and the references regarding implementation has been given in appendix C.

CHAPTER 2

BACKGROUND AND RELATED WORK

2.1. Diffusion Tensor Imaging In Group Studies

Diffusion tensor imaging (DTI) enables analyzing the white matter tissue structure, and provides visibility and quantitative information about the geometry of major fiber bundles. One can measure metrics such as diffusion characteristics through tensor orientation, anisotropy etc.(Goodlett et al. 2009). Since the self-diffusivity of water molecule is sensitive to changes in its local environment, the diffusion tensor acts as a probe of tissue architecture. Hence, the diffusion properties extracted by DTI proves to be an effective source to be used in group studies in clinical analysis.

Diffusion tensor imaging (DTI) has been used to analyze and differentiate brain white matter architecture between normal and pathologic cases. Mainly for disorders such as schizophrenia, autism, Alzheimer's disease, normal development, and depression (Khurd et all. 2006). Such studies use statistical analysis of the anatomical structures in diffusion tensor images of diseased and normal brains. In the literature there are various methods to do group analysis using DTI or DWI data. These methods can be classified into ROI based methods, Voxel Based Analysis, Fiber Tract Based Analysis.

ROI based studies are the oldest techniques that have been used. The regions of interest (ROI) are manually placed in the brain and scalar measures such as mean anisotropy or fractional anisotropy are derived from the diffusion tensors within the ROI to be analyzed. However manually placing ROI's requires intensive anatomical knowledge and could be subject to user bias. A possible solution is registering all subjects to a common segmented atlas, select a well-known white matter structure as a template ROI and reverse the warping on the template ROI to find a subject's mapped ROI. Tractography can also be used for placing ROI's and evaluating the group differences.

Voxel-wise comparison is based on the well-known voxel based morphometry technique (VBM), originally developed for finding local changes in grey matter density in T1-weighted structural brain images. The voxel-wise analysis starts with normalizing the images to a common template to align voxels together in all of the images, and then applying hypothesis testing at each voxel. In early studies the analysis mostly depended on scalar quantities derived from the diffusion tensors using univariate statistics However recent studies show that multivariate approaches provide richer information

than univariate statistics by using either diffusion tensor itself as a multivariate unit or eigenvalues and eigenvectors of the tensor.

Fiber tract based analysis is another approach to compute the quantitative parameters of interest along the tracts (Gerig, Gouttard and Corouge 2004; Fillard and Gerig,2003). The idea behind this method considers the underlying anatomical unit in diffusion tensor images as a fiber tract, not a voxel (Mahnaz et al., 2007). The most important point of fiber tract based analysis is that if the researcher is confident in comparing the same tract between each subject, any statistics would represent the characteristics of that tract, so the findings result from different characteristics of the specific tracts rather than the overall anatomy/shape of the individual brains. The properties of fiber tracts can be scalar values derived from tensors such as MD, FA or Trace or can be solely dependent on tensors or shape information like curvature and torsion of the specific tract.

Diffusion Tensor Image is by nature a non-scalar image and it potentially offers rich information beyond the scalar descriptors of tensors such as FA, MD and trace. There is an important information loss by just taking only scalar values into the consideration, and neglecting the tensor structure. In addition the researcher should also have a priori knowledge of expected changes due to the pathological cases (Khurd et all. 2006). Multivariate statistical analysis that uses tensor information will be the main concern. However since diffusion tensors are symmetric positive definite matrices, the tensor domain is non-linear and conventional vector space techniques can not be used. In order to use tensors in the group-wise analysis, one must define necessary operations such as distance, interpolation, filtering, and hypothesis testing on tensors. Different tensor metrics and statistics have been proposed for this purpose. By the help of these metrics and statistics, a multivariate analysis is possible based solely on tensors, which can also be utilized for ROI based, voxel based and tract based analysis. Registration of diffusion tensor imaging and tensor interpolation can also be more precise by using these metrics.

The tractography of DTI images will result in 1D fiber tracts that in fact do not represent the real anatomical bundle. So fiber tract classification and segmentation should be done in order to automatically label the individual bundles and assign to an anatomical bundle. These classifications and segmentation can be used in Fiber tract analysis and connectivity analysis (cortico – cortical connectivity analysis) that also can be used for group-wise analysis. This can only be done by generating segments of the trajectories into bundles and creating correspondence between points on trajectories within a bundle (Mahnaz et al., 2007).

2.1.1. ROI Based Studies

ROI methods begin by identifying anatomical brain regions and comparing the anisotropy or the extent of the region. Then the ROI analysis method can be done by voxel-wise comparison or tract-based statistical techniques. The placement of the ROI can have a significant effect on the results of the analysis. In the fully manual approach, an anatomical expert can select the same ROI's for all subjects or register subject images

on to an atlas (structural or FA images), then select ROI from an atlas image and apply warping to the subject ROI with the same parameters. In either case the ROI based analysis is problematic considering the facts in the following (Zhang et al. 2010).

- Placing the exact ROI for each subject is a time consuming and very labor intensive task for large group data sets.
- The ROIs are drawn in 2D in one of the three orthogonal views and are expanded to the other angles. However most of the structures can not be defined by 2D planes as smoothly as the structure itself (e.g. the corpus callosum and thalamic radiation). Sometimes it is also not basically possible to define in 2D if the shape is so complex. Cortico-cortical tracks, optic radiations are such examples.
- DTI images have low resolution so even small changes in the orientation plane or positions of slices can result in variability of the measurements. This becomes critical if the structure is small.
- If the ROI's are not in high accuracy or covers larger structures, it is common that some voxels will belong to other fiber tracts or even gray matter and CSF. This effects the success ratio of the analysis significantly.
- Considering those pitfalls stated above, whole brain analysis based on different regions or structure is not possible or effective.

Apart from these problems, there are some automatic ROI placement methods that can be used in ROI based analysis. Zhang et al. (2008) has created automated placements of 3D region of interests. 3D ROIs are pre-defined by an expert and then the atlas with pre-defined ROUs are linearly or non-linearly warped to each subject's data. Although the proposed method has been designed for automated tractography, it can also be used for ROI based voxel by voxel statistics. Zhang et al. (2010), created an atlas guided method to automate ROI placement. They used DTI-based human brain atlas (Oishi et al., 2009), that has 130 pre-segmented gray and white matter areas. The study focused on thalamic radiation and short association tracts that have been difficult to systematically reconstruct with manual ROIs. There also exist probabilistic maps of a comprehensive set of tracts.

Using either manual or automatic ROI placement, the next step will be hypothesis testing. Within the ROIs, diffusion properties such as FA or mean diffusivity (MD) are averaged to create a single statistic for each group. The group differences can be investigated using univariate tests like t-test.

2.1.2. Voxel-Wise Comparison

Voxel-based morphometry looks for localized differences in grey matter density between two groups of subjects and it has been used in many structural imaging studies. Adaptation of this for DTI group studies can be simply summarized as follows (Smith et, al, 2006):

- Align all subjects' structural and FA images to standard space template image (Atlas image). Optionally, FA image is first registered to structural image (intra subject registration) and then the structural images of different subjects can be registered on the template image (inter subject registration).
- Smooth the output data to eliminate the effects of misalignment of structures. When the registration is imperfect, smoothing is used, because smoothing makes the data more Gaussian distributed. In most of the studies, 4 to 16-mm full-width half maximum (FWHM) smoothing is applied.
- Carry out voxelwise statistics, using any relevant covariates for the design matrix. A simple univariate statistic can be used where, each voxel is processed separately and represented by a 1D vector of values.
- Threshold the resulting image using T, F or Z statistics taking into account multiple comparison correction. The final step will be clustering of the voxels that are above the threshold.

In the literature, the main diversity of these steps is in selecting voxelwise statistics (step 3) and hypothesis testing methods (step 4). For voxelwise statistics, scalar values such as Fractional Anisotropy (FA), Apparent Diffusion Coefficient (ADC), Voxel Scale Connectivity (VSC) (Parker et al., 2002), and the coherence measure (Klingberg et al., 2000), have been used extensively to compare diffusivity across groups of subjects (Lim and Helpern, 2002).

For example, Nagy et. al.(2003) uses FA and the coherence metrics to study the abnormal white matter microarchitecture of brain tissues of prematurely born infants (Nagy et al., 2003). Kubicki et al. (2002) uses FA values and analyze temporal–frontal connections, Reporting that left-greater-than-right asymmetry in FA values have been found (Kubicki et al., 2002). Counsell et al. found that ADC values in infants with overt white matter pathology have higher ADC values compared to healthy infants (Counsell et al., 2003).

However, the diffusion tensor itself has much more richer information than any scalar representative. For example, FA values measure only the degree of anisotropy but not the orientation of eigenvectors of a diffusion tensor. Hence the mapping of eigenvalues to FA values is non-unique; for the same FA values, different sets of the eigenvalues can be found or vice versa. This loss of information can conceal between-group differences. ADC as well is a linear combination of eigenvalues that provides information about overall diffusivity, but it also suffers in detecting group differences. Like FA values, ADC values also suffer from representing direction of the diffusivity. As a result, voxelwise statistics that use only scalar values such as FA or ADC provide little insight into differences in local fiber trajectory across groups.

There also exists non-scalar voxelwise statistics efforts in the literature. Schwartzman et. al. (2005) compares principal directions (PDs) for each voxel and Martin et al. (1999) compares eigenvalues. Representing the tensor as a six dimensional element of vectors and using vector distance operation on means of the groups is another proposed method (Whitcher et al, 2007). However determination of tensor could not be error-free

due to the noise in DTI dataset so estimation techniques has been used to find positive definite tensor by the definition of tensor model as stated in Appendix-A.

The tensor metrics and operations on these metrics becomes an important point if one wishes to use full information coming from tensor on voxelwise statistics. Basser and Pajavic (2003) proposed a tensor-variate statistical framework for DTI by placing diffusion tensors on a Euclidean manifold (Basser and Pajevic 2003). However the Euclidean metric is not appropriate for diffusion tensors because DTI datasets are commonly assumed to follow a Gaussian distribution and the distribution of noise, but tensors are not positive definite always, because positive-definite tensors are only a subspace of Euclidean space.

Arsigny et al. (2005) used Log-Euclidean metric, where the tensors are transformed into symmetric matrices using logarithmic transformations and derived statistical analysis based on those. Finally they used exponential transformations to generate positive-definite tensors (Arsigny et al, 2005). Another framework is called Reimannian metric (Pennec et al, 2006). On Riemannian manifolds, the distance function can be defined with affine-invariance using rotation, scale, shear, inversion invariance where it can only operate on tensors belonging to positive-definite symmetric matrices. The discussion about tensor based metrics and statistics will be described in section 2.1.4.

Univariate two-sample hypothesis tests are generally used in group comparison. For each voxel, scalar values such as FA, MD are extracted and used in comparison. Two-sample t-test can be chosen if FA values is normally distributed. Otherwise; the alternative hypothesis tests like permutation, bootstrap or rank-based nonparametric tests can be used. For multivariate testing, Hotelling T2, Cramér, log-Cramér and permutation tests can be used. Hotelling T2 test is much more suitable to be applied on Euclidian manifold, Cramér test is suitable for Reimannian manifolds and log-Cramér is suitable for log-Euclidian space (Whitcher et al, 2007).

Bansal et. al. (2007) proposes a different strategy for multivariate voxel-wise analysis. They did not use any metrics described above to calculate Mean Tensors (MT), however they computed statistical properties of MT using Central Limit Theorem and then calculated the probability distribution of the eigenvalues and eigenvectors (Bansal et al, 2007). From MT they calculated eigenspace components and computed covariance matrix. Finally standard multivariate statistical procedures like Hotelling T2 tests has been applied on the distribution of eigenspace components to detect between-group differences in tensor morphology at each voxel.

The main problem of voxel-wise comparison studies related with DTI is the alignment problem. The registration of subject's data to common space must be totally successful. The registration algorithm must resolve topological variabilities and also exactly align even very fine structure of each brain. This is a critical step for voxel-wise analysis since even a small misalignment could end up with significantly underestimated parameters. Simon et al. (2005) and Vangberg et al. (2005) confront this problem in their studies. Simon et al. (2005) states that apparent FA changes as being in fact due to changes in

ventricle size and Vangberg et al. (2005) states that the results are strongly suggestive of a shift of the pyramidal tract, rather than a true change in WM integrity. To resolve misalignment, spatially smoothing data before computing voxelwise statistics has been proposed. However, the smoothing also brings new problems, Jones et al. (2005) states that the final result depends on amount of smoothing but there is no a common method to decide on smoothing amount. Jones et al. (2005) investigate this in detail and show that the final results depend very strongly on the amount of smoothing. Different smoothing extents (from 0- to 16-mm FWHM) are applied, but no consistent group differences have been found across the different tests. (Park et al.,2004) also investigated asymmetry in schizophrenia, using 3-, 6-, and 9- mm FWHM smoothing and the results are variant in each case. Van Hecke et al (2010), investigate isotropic and anisotropic smoothing for Voxel-Based DTI analyses in a simulation study and found that the sensitivity and the specificity values also depend on anisotropic smoothing kernels in a VBA study. They stated that the VBA sensitivity and specificity are significantly reduced when the data sets are smoothed isotopically with a FWHM larger than 3 mm (Van Hecke et al., 2010).

Tract Based Spatial Statistics (TBSS) package is the most used voxel-wise analysis tool to analyses the group differences in the literature. TBSS tackles the alignment and smoothing problem for voxel-wise statistics by combining strengths of VBM-style analyses and Tractography-based approaches (Smith et al., 2006). VBM-style analyses are fully automated for investigating whole brain but alignment and smoothing are problematic. On the other hand, Tractography-based approaches work in the space of individual subject's tractography results and do not require smoothing but do not work on the whole brain and require user intervention. TBSS introduces "group mean FA skeleton" that represents centers of all group fiber bundles. The main steps for TBSS analysis are as follows:

- *Preprocess:* The diffusion tensors are calculated using simple least squares fit of the tensor model and brain extraction is done using BET tool in FSL software (Smith 2002).
- *Alignment:* A common registration target is defined (one of the subject's image) and all subjects' FA images are aligned to this target using nonlinear registration. At this stage, perfect alignment is not expected or required. TBSS uses 'Image Registration Toolkit' (IRTK) which is nonlinear registration tool based on free-form deformations and B-Splines (Rueckert et al., 1999). They limit high-dimensional warping so that the overall structure of registered image is not lost. The choice of the registration target is not random, instead the most typical subject of the entire group is chosen. To find this most typical subject, It registers every subject to every other subject, summarizes each warp field by its mean displacement, and select the target subject as being the one with the minimum mean distance to all other subjects.
- *FA Skeleton:* From all aligned FA images, the mean is computed and skeletonization is applied over this mean FA image. A threshold is applied to suppress low mean FA areas. The different skeletonization stages can be found in Figure 1.

- *Projecting Subject Images on to Skeleton:* Each subject's (aligned) FA image is projected onto the skeleton. In case of misalignment, skeleton is filled with FA values from the nearest relevant tract center.
- *Voxel-wise Statistics:* Voxel wise statistics is carried out across subjects on the skeleton space FA data. Univariate linear modeling has been proposed to process each skeleton voxel independently, applying the general linear model (GLM, i.e., multiple regression) across subjects. An unpaired t test can be used to test for significant local FA differences between a group of patients and a group of controls.

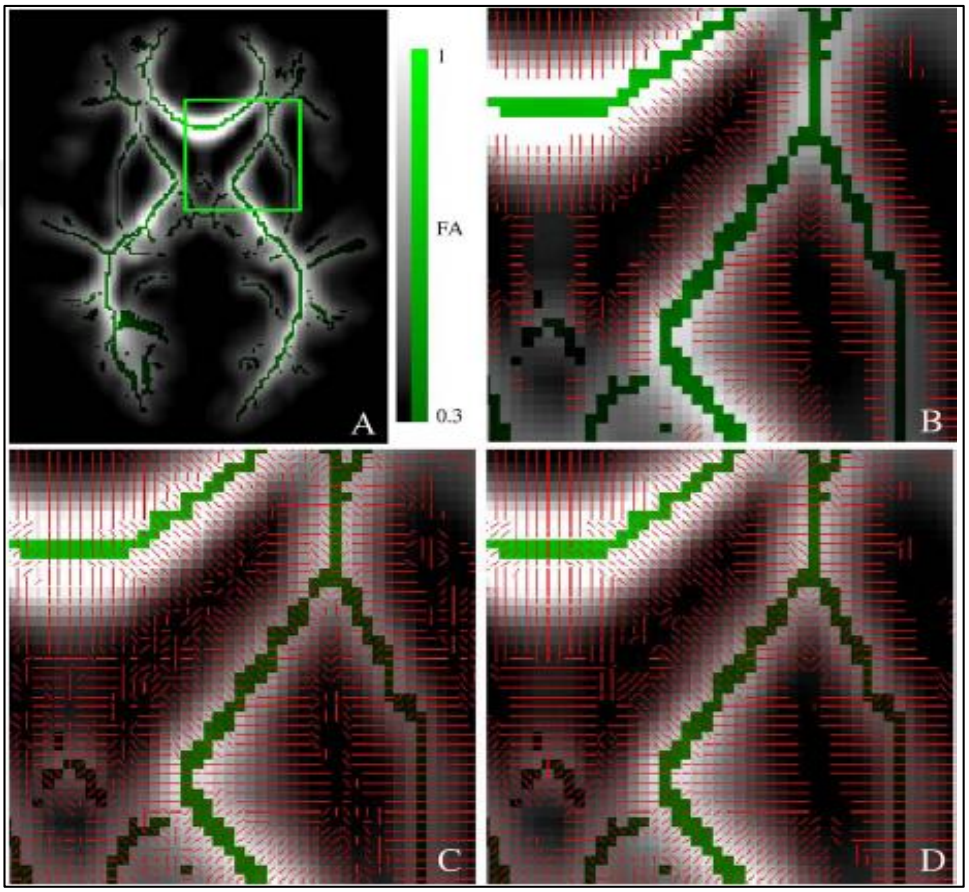

Figure 1: Different skeletonization stages. (A) Original mean FA image with final skeleton and the ROI used for the remaining sub-images. (B) Skeletonization stage 1, using local FA centre-of-gravity to find tract perpendiculars. (C) Skeletonization after stage 2, using FA image second-derivative to find remaining perpendiculars. (D) Result of smoothing the perpendicular direction vector image. Note that the tract appears more than a single voxel thick in some places, because of its 3D nature; where the fiber bundle surface lies partially parallel to the plane being viewed, it will not appear thin, though would do if viewed with a different 3D slicing (Smith et al. 2006).

Smith et al. (2006) have applied TBSS on three different white matter diseases; schizophrenia, ALS and multiple sclerosis. The have analyzed data from 33

schizophrenics and 36 age-matched controls. After applying the TBSS preprocessing, they carried out a region-of-interest analysis on mean FA skeleton voxels in the superior cingulum bundle using unpaired t-test. They also analyzed data from 13 ALS patients and 20 controls. After applying the TBSS preprocessing, they carried out GLM analyses. Figure 2 shows the result: in blue where FA is reduced in ALS compared with controls—the majority of the mean FA skeleton shows reduction, including most of the corpus callosum and pyramidal/ corticospinal tracts. Red shows where FA is negatively correlated with ALS progression rate; this is confined to the pyramidal/corticospinal tract, clearly seen in coronal and axial view.

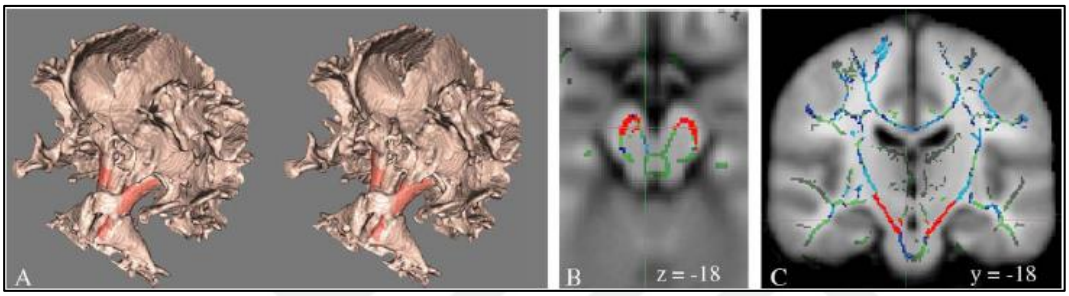

Figure 2: ALS analysis with TBSS (Smith et al. 2006).

2.1.3. Fiber Tract Analysis

If the area of interest is well-known and if the hypothesis depends on a set of fiber tract differences for group studies, a better approach than voxelwise or ROI based analysis can be fiber tract analysis, in which the quantitative parameters of interest along the trajectories can be computed. In this case, the researcher has the opportunity to build a hypothesis that depends only on diffusivity of the fiber tract and/or the shape of the fiber tract itself. Majority of tractography-based analyses calculate the mean in the entire track of scalar values such as fractional anisotropy (FA) or the mean diffusivity (MD) (Pagani et al., 2005; Heiervang et al., 2006; Jones et al., 2006; Wakana et al., 2007;O'Donnell, Westin, and Golby 2009a). As an alternative, other studies measure mean FA or other scalars in regions of interest (ROIs) within tracts (e.g. Pierpaoli et al., 1996; Kubicki et al., 2003). The main algorithm behind fiber tract analysis that calculates mean differences of fiber tracts is as follows.

1. Perform tractography on each subject either using deterministic or probabilistic methods
a. Through visual dissection, build the tract by determining the ROI's and perform tractography.
b. Determine the tract using atlas, register the subject image on to atlas, select ROI's and perform tractography.

c. Register each subject on to a mean image and select ROI's to perform tractography.
2. Segment the tracts/trajectories into fiber bundles. This method is not necessary if the fiber tract has been computed deterministically. But for probabilistic tractography methods, it is necessary. Classification and segmentation of fiber tracts will be described in section 2.1.5.
3. Obtain correspondence between points on trajectories within a bundle. Do quantitative analysis on these points, either on correspondence points or by calculating a mean value (FA, MD, etc.) for each tract. Curvatures and other shape features (widths, volumes, areas) of the entire bundle can also be investigated.

Each step in this algorithm proposes new challenges in implementing tract oriented statistics in population. In the first step, the main challenge is to find a consistent spatial parameterization within and between populations. Even when tractography seeds are set for each image, the natural variability of brain size and shape prohibits an automatic consistent parameterization for arc length models of diffusion.

The second step, namely segmentation and classification of tracts, is also problematic and will be described in section 2.1.5. The last step consists of one of the most important and challenging tasks for fiber tract based analysis is finding trajectory correspondences along the length of the fibers for each subject.

There are mainly two different approaches: the first one of them is parameterizing the tracts by arc length, the second one is by registering the subject on common space (atlas). Previously mentioned tract based spatial statistics (TBSS) can also be considered within registration based correspondence matching.

One of the important works on fiber tract based analysis is done by Corouge, et al. (2005). In this study, the preprocessing step has been done by tensor estimation and fiber tractography. To build template shape, fibers are reparametrized by cubic B-spline curves. First, an origin, which can be reliably identified across subjects, is defined for each fiber tract (Corouge, et al, 2005). The origin can be either a geometric criterion, e.g., a cross-section with minimal area, or anatomical information such as an intersection with the midsagittal plane. Points with the same arc-length along the fiber tract are matched and the alignment of all curves in the training set is achieved by Procrustes analysis (Goodall, et all, 1991).

After aligning the shapes, the mean shape is estimated by averaging the spatial coordinates at each corresponding location over the tract (Corouge, et al, 2005). The statistics of the diffusion tensor is calculated over cross-sections along the mean curve. The mean tensors are computed by interpolation (with 2x2x2 neighbors) and group averaging on Riemannian Manifolds. The group comparison between the subjects can be done on average diffusion tensor using FA, MD that has been computed from the mean tensors.

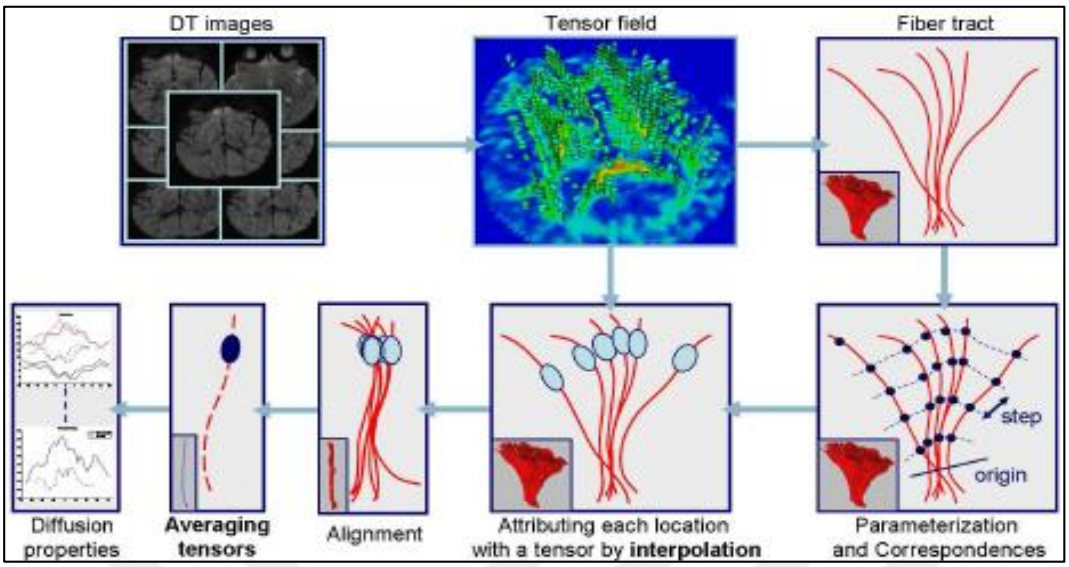

Figure 3: Algorithm for fiber tract-oriented statistics for quantitative diffusion tensor MRI analysis (Corouge, et al, 2005).

O'Donnell et al. (2009) have performed quantitative analysis of DTI data along the white matter tracts using tract-based morphometry (TBM). In his work, he presented an automatic TBM method for white matter analysis in groups building analogy between the voxel-based morphometry method (in which local statistical analyses are performed on features derived from scalar MR intensities), and local statistical analysis of features derived from DTI (O'Donnell, Westin, and Golby 2009b). Their analysis not only considers microstructural morphometry such as FA, but also macroscopic morphological features regarding the entire curvatures and shape features (widths, volumes, areas) of the entire bundle (O'Donnell et al., 2009).

At first step, affine registration has been applied to the subject images and the resulting transformation have been applied to the fibers extracted from whole brain tractography. Fiber bundles are then segmented simultaneously in all subjects via group fiber clustering (O'Donnell and Westin 2007). The second step calculates the prototype fiber representing each fiber bundle. For this issue 3 methods have been proposed as follows:

Method (1) Maddah's (2008) proposal to choose the longest fiber in the bundle (M. Maddah, Grimson, and Warfield n.d.).

Method (2) Choose the fiber with the greatest length weighted by local "fiber density". This will also eliminate very long outlier tracks

Method (3) Use fiber affinity metric to choose the fiber that is the most representative of the bundle's trajectory across all subjects (O'Donnell, Westin, and Golby 2009b).

Figure 4b shows the outputs of different methods. Red fiber bundle shows method 1: longest, blue shows method 2: fiber-density-weighted longest and light green method

3: embedding. This prototype bundle was parameterized using the arc length. To find the correspondence of points for different subject's fiber bundles, optimal point match method (OP) (Kuhn, 1955) has been used for optimal assignment that rewards match found in directions nearly perpendicular to the prototype. At this step, all fiber bundles of different subjects have been parameterized and corresponding points have been found as seen in Figure 4b. At the end, to measure the descriptive statistics, mean FA across all fibers was calculated for each arc length coordinate. To do the statistical analysis in the group, for each arc length, a two-tailed paired t-test was employed

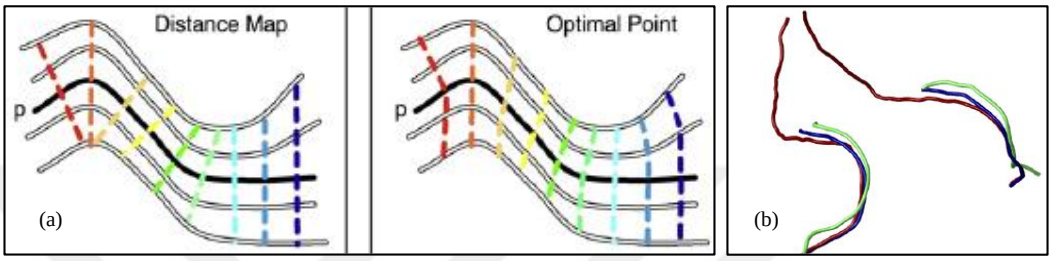

Figure 4: Tract-based morphometry for white matter group analysis (O'Donnell et al., 2009).

Another interesting method has been proposed by Goodlett et al. (2009). A new parametrization technique has been introduced based on arc length of atlas fiber tracts. The atlas is generated by mapping all subjects' images. The diffusion properties within a fiber bundle are then computed based on this parametrization. The sample points are chosen on the parametrized tracts. Diffusion properties such as FA, MD are computed on the sample points and modeled as continuous spatial functions of arc length, where the tract functions are multivariate functions which map arc length to orthogonal measures of tensor shape. To identify group differences, non-parametric statistic testing with permutation testing based on the Hotelling T2 statistic is used (Goodlett et al., 2009). The overall algorithm is given in Figure 5 and parametrization is in Figure 6.

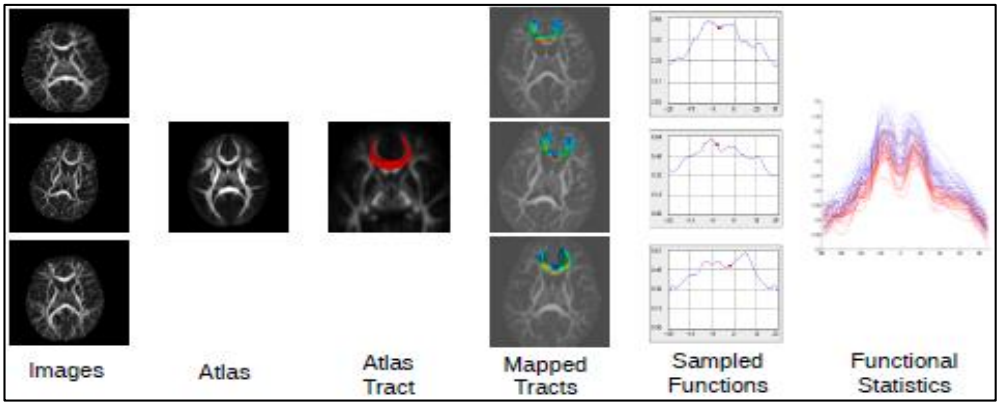

Figure 5: Group analysis of fiber tract statistics (Goodlett et al., 2009).

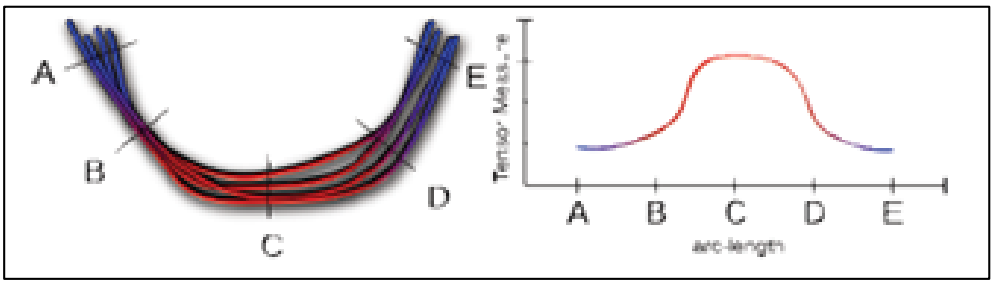

Figure 6: Goodlett parametrization of fiber tracts, the sampled points are computed using arc length and tensor specific properties are computed and fitted to a function (Goodlett et al., 2009).

2.1.4. Tensor Based Metrics and Statistics

In order to compare group studies, we need a computation schema that derives statistics; compare or correlate among metrics. DTI is a multidimensional image and it is also non-Euclidean. The Euclidean computation on tensor matrix has mainly two negative effects. First, Euclidean computations can result in null or negative eigenvalues of tensors, but by definition, the tensor is a symmetric positive definite matrix. This is also correct considering the physical properties of water diffusion: a zero diffusion is impossible and a negative diffusion is undefined. To avoid this, computations will be limited to only the first eigenvector or orientation. Second, tensor's determinant is a direct measure of the dispersion of the associated local water molecules movement, however if we average the tensors in Euclidean space, this might lead very often to a tensor swelling effect: the determinant (and thus the dispersion) of the Euclidean mean can be larger than the original determinants (Arsigny et al, 2005). By definition, diffusion tensors are covariance matrices of Brownian motion of water molecules, if we add more dispersion, because of introducing more diffusion, it becomes physically unacceptable (Arsigny et al, 2005). The swelling effect can be seen in Figure 7. In this figure white ellipsoids are averaged and blue ellipsoids represent linear computations (swelling effect) and red ellipsoids are without swelling effect.

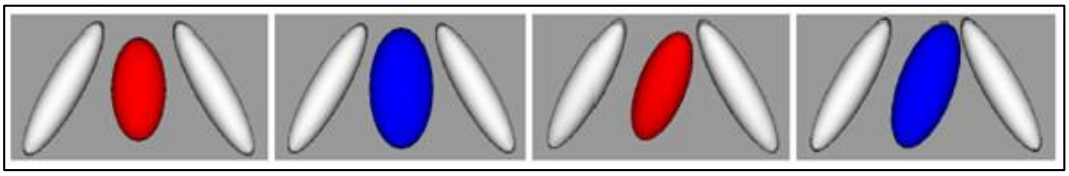

Figure 7: Swelling effect of averaging tensors.

In the literature, there exists a number of computational frameworks that can work on tensors. Pennec et. al (2006) proposed a computational framework that uses Riemannian manifolds (by Do Carmo et al., 1992) and developed an extensive calculus for performing computations on tensors consisting of averaging,

interpolation and filtering (Pennec et al. , 2006). Arsigny et al. (2005) introduced a log-Euclidean metric. They first transformed each tensor using logarithmic transformation so Euclidean calculations became possible in that space. Therefore, standard operations for means and variances were possible. Fletcher and Joshi (2004) developed the notion of principal geodesic analysis (PGA), which extended principal component analysis to manifolds, by using an affine–invariant metric on the space of symmetric positive–definite tensors (Fletcher et al., 2004). There were also efforts based on manifold learning techniques that provided frameworks for analyzing tensor information (Khurd et al, 2006; Brun, 2006).

2.1.4.1. Riemannian Framework for Tensor Computing

In the geometric framework, Riemannian metric is a continuous collection of scalar products on the tangent space at each point of the manifold. On any curve on the manifold, we can use instantaneous speed vector and its norm on each point to compute the instantaneous speed (Pennec, 2017). Integration of those vectors along the curve reveals the length. On Riemannian manifold, the distance between two points can be computed by the minimum length among the curves joining these points. The curves realizing this minimum for any two points of the manifold are called geodesics. In Figure 8 left side shows that the tangent planes at points x and y of the sphere S are different: the vectors v and w of TxM cannot be compared to the vectors t and u of TyM. However by defining the scalar product on each tangent plane, the geodesics starting at x are straight lines in the exponential map and the distance along them is conserved (Pennec et. al, 2006).

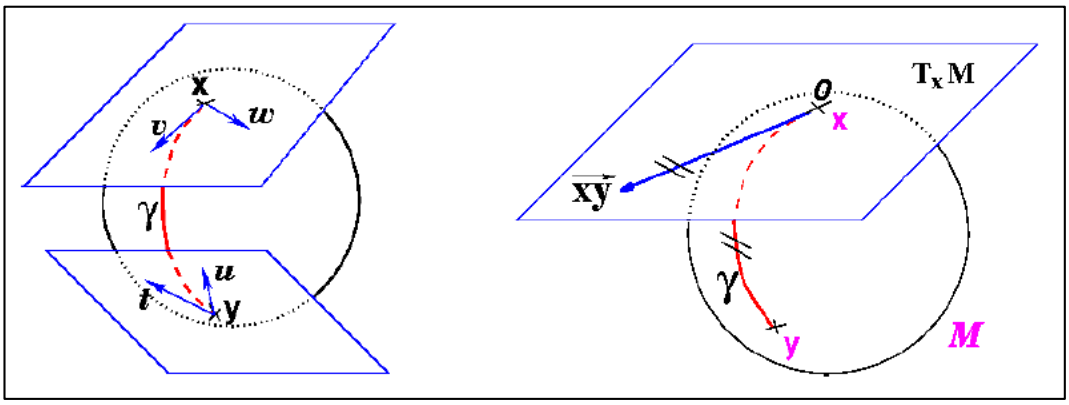

Figure 8: Riemannian metric (Pennec et. al., 2006).

Additions and subtractions of the vectors in a Riemannian framework can be derived by bipoint, an antecedent of vector. Riemannian manifold loses global comparison of the vectors in that case. The vectors can only be compared locally. This means that all vectors should keep information about which points of the manifold owns the vector. However, one can also see a vector $\overrightarrow{xy}$ (attached at point x) as a vector

of the tangent space at that point. Such a vector may be identified to a point on the manifold using the geodesic starting at x with tangent vector $\overrightarrow{xy}$, i.e. using the exponential map: y = expx ($\overrightarrow{xy}$). Conversely, the logarithmic map may be used to map almost any bipoint (x, y) into a vector $\overrightarrow{xy}$ = logx(y) of TxM (Pennec et al., 2006). This keeps local mapping and allows local comparison so addition and subtraction via logarithmic can easily be defined the necessary operations on Riemannian manifolds, as seen in Figure 9.

	Vector space	Riemannian manifold
Subtraction	$\overrightarrow{xy} = y - x$	$\overrightarrow{\mathrm{xy}} = \log_{\mathrm{x}}(\mathrm{y})$
Addition	$y = x + \overrightarrow{xy}$	$\mathrm{y} = \exp_{\mathrm{x}}(\overrightarrow{\mathrm{xy}})$
Distance	$\mathrm{dist}(x, y) = \lVert y - x \rVert$	$\mathrm{dist}(\mathrm{x}, \mathrm{y}) = \lVert \overrightarrow{\mathrm{xy}} \rVert_{\mathrm{x}}$
Mean value (implicit)	$\sum_i \overrightarrow{\bar{x}x_i} = 0$	$\sum_i \log_{\bar{\mathrm{x}}}(\mathrm{x}_i) = 0$
Gradient descent	$x_{t+\varepsilon} = x_t - \varepsilon \nabla C(x_t)$	$\mathrm{x}_{t+\varepsilon} = \exp_{\mathrm{x}_t}(-\varepsilon \nabla C(x_t))$
Linear (geodesic) interpolation	$x(t) = x_1 + t\,\overrightarrow{x_1 x_2}$	$\mathrm{x}(t) = \exp_{\mathrm{x}_1}(t\,\overrightarrow{\mathrm{x}_1\mathrm{x}_2})$

Figure 9: Basic standard operations in a Riemannian manifold (Pennec et. al, 2006).

By using these operations and their derivations Pennec proposes an affine invariant metric that works on the space of positive define symmetric matrices (tensors) with a very regular manifold structure (Pennec et. al, 2006). He proposes a globally consistent orthonormal coordinate system (There is one and only one geodesic joining any two tensors) that is very close to a vector space, except that the space is curved. So interpolation, filtering, diffusion and restoration of tensor fields is possible by doing regular vector operations. They have also proposed simple statistical operations on tensors.

2.1.4.2. Log- Euclidean Metrics

Arsigny state that the Riemannian framework needs complex calculations, so it is not efficient for tensor computations (Arsigny et al. 2005). They propose a new lightweight computational framework that has not affine-invariant metric but has a metric that is invariant by similarity (orthogonal transformation and scale affine invariant) called Log-Euclidean. This framework results in classical Euclidean computations in the domain of matrix logarithms (Arsigny et al., 2005).

In their paper (Arsigny et al., 2005), they first define the Logarithm for tensors where a tensor S has a unique symmetric matrix logarithm L = log(S). This verifies S = exp(L), where exp is the matrix exponential. Each symmetric matrix is associated to a tensor by the exponential. Then they build a Vector Space on Tensors to create a one-to-one mapping between the tensor space and the vector space of symmetric matrices. By these, one can transfer the space to tensors with the addition "+" and the scalar multiplication "." Using the matrix exponential. This defines on

tensors the logarithmic multiplication “x” and the logarithmic scalar multiplication “dot”, given by:

$$\begin{cases} S_1 \; x \; S_2 = \exp(\log(S_1) + \log(S_2)) \\ \delta \; dot \; S = \exp(\, \delta \, .\log(S)) = \; S^{\delta} \end{cases}$$

Then they define Log-Euclidean Metric from a Euclidean norm $\|.\|$ on symmetric matrices as follows: $dist(S_1, S_2) = \|\log(S_1) - \; \log(S_2)\|$.

The comparison of these frameworks can be seen below. Figure 10 shows the differences between Euclidean and Riemannian metrics. Top left image is original image with some noise, top right show Gaussian filtering on Euclidean metric, bottom left Gaussian filtering on Riemannian metric. Bottom right shows anisotropic filtering on Riemannian metric. It can be seen that anisotropic filtering on Riemannian gives the best result and Gaussian filtering on Euclidean metric is the worst.

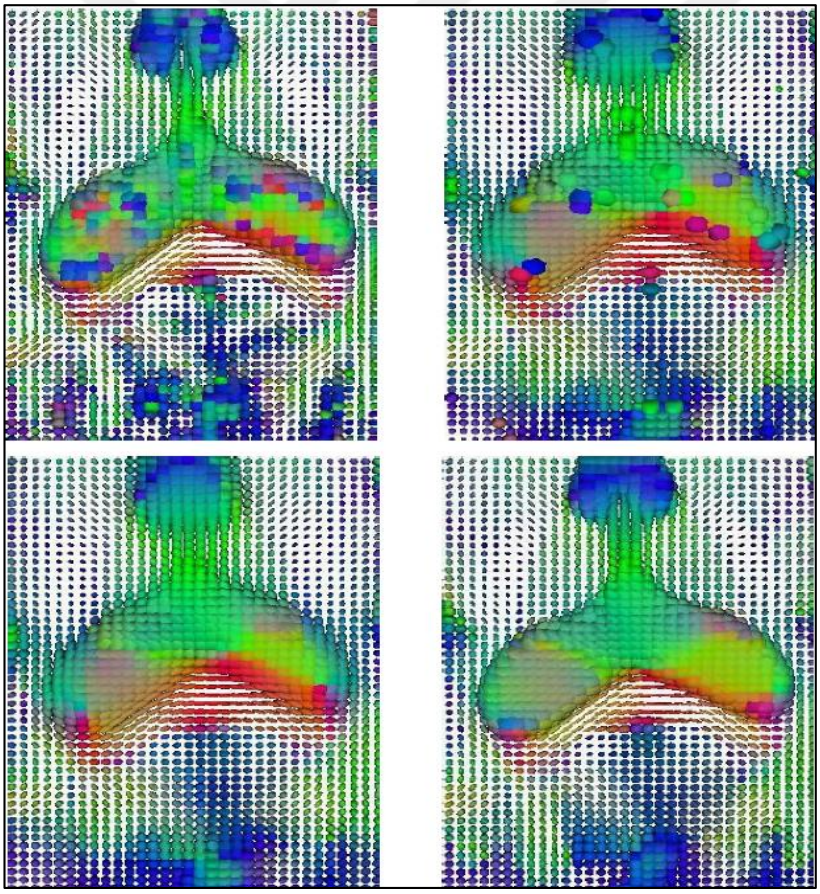

Figure 10: Differences of Euclidian and Riemannian metrics (Pennec et. al, 2006).

Figure 11 shows Bilinear interpolation of 4 tensors at the corners of a grid. Left: Euclidean interpolation. Middle: affine-invariant interpolation. Right: Log-Euclidean interpolation. In both Riemannian frameworks, as opposed to the Euclidean case, swelling effect of the tensor is not observed where Log-Euclidean tensor means are slightly more anisotropic than their Riemannian counterparts.

Figure 11: Interpolation differences between Riemannian and Log-Euclidian metrics (Arsigny et al., 2005).

Figure 12 shows regularization of a synthetic DTI slice. The original tensors are deformed by adding a noise. The original data is properly reconstructed in the Log-Euclidean case, as opposed to the Euclidean case with the swelling effect.

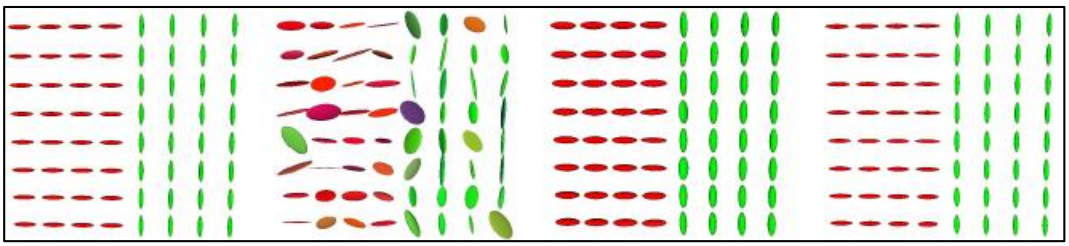

Figure 12: Regularization differences between Riemannian and Log-Euclidian metrics, Left: original synthetic data. Middle left: noisy data. Middle right: Euclidean regularization. Right: Log-Euclidean regularization. (Arsigny et al., 2005).

2.1.5. Fiber Classification and Segmentation

Computing the quantitative parameters of interest along the trajectories instead of within a specified region makes more sense as the underlying anatomical unit in DTI is a fiber tract, not a voxel. The ideal case is to do the computation on an anatomical bundle of a fiber tract, by calculating the fiber tracts that ends up the trajectories (Mahnaz et al., 2007). The important problem to resolve is to segment the trajectories into bundles and obtain correspondence between points on trajectories within a bundle.

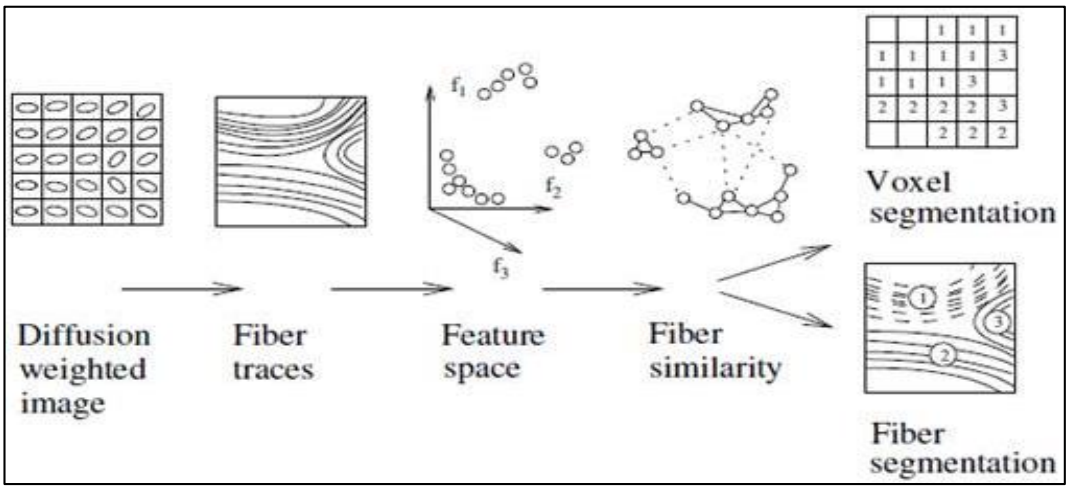

Figure 13: Fiber clustering overview (Brun et al., 2004).

The necessary steps for fiber clustering are given in Figure 13. Starting from diffusion weighted image, fiber traces are constructed using deterministic or probabilistic tractography algorithms. After fiber traces have been made, for each fiber tract a feature vector is computed. The feature vector can consist of diffusion related values as well as morphological descriptors such as shape, curvature, etc. After mapping each fiber tract to the feature space, clustering algorithms like k-means, K-nearest neighbors, normalized cuts, etc. can be applied to cluster the data. After clustering, voxel segmentation and fiber segmentation can be done on voxel space or fiber tracts.

Brun et al. (2004) stated that the pairwise comparison of all fiber traces could be a time-demanding task so they proposed that the problem can be handled in three steps (Brun et al., 2004). First, they map fiber traces to Euclidean feature space preserving some but not all information about fiber shape and connectivity. Brun et. al. (2004) proposes that a fiber trace can be represented as a set of points in space where each point can be represented as a 9-dimensional feature vector by calculating the mean vector m and the covariance matrix C of the points building up the fiber trace. Brun et. al. (2004) also use Gaussian kernel for comparison of points in Euclidean space and finally, build a undirected weighted graph G = (V;E), where the nodes correspond to the points to be clustered and each edge has weight w(i; j) which represent the similarity between point i and j. They apply normalized cut algorithm to cluster the fiber tracts. The result of Brun's algorithm is given in Figure 14.

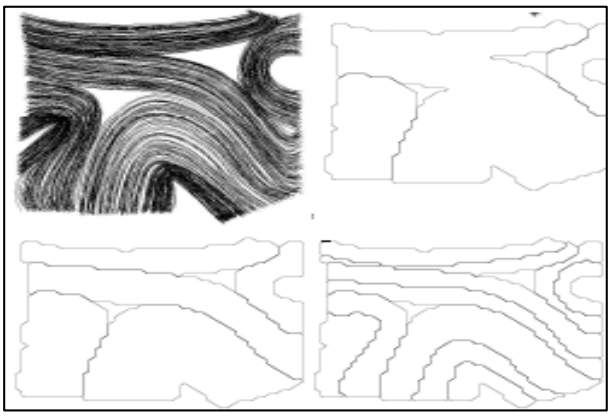

Figure 14: Segmentation obtained from recursive bipartitioning of the fiber traces. Maximum value of the Ncut set to 0.2, 2.5 and 4.5 respectively (Brun et al., 2004).

There are several other papers that have addressed clustering the fiber tracts into bundles. Some of the interesting ones are as follows. Batchelor et al. (2006) compared several mathematical tools including link, principal component analysis (PCA) and the Euclidean distance of Fourier descriptors to study the relative spatial configurations of trajectory pairs and indicated that these measures could be used in classifying and clustering the reconstructed fiber curves (Batchelor et al., 2006). Gerig et al. (2004) and Corouge et al. (2004) introduced Hausdorff and similar distance metrics to implicitly model tract's shape characteristics. Shimony et al. (2002) used fuzzy c-means clustering and Gaffney et al. (2003) used curve clustering techniques.

Apart from clustering, point-by-point correspondence between the trajectories of each cluster is also an important issue especially for fiber tract based analysis. Ding et al. (2003) proposed a quantification method by finding the corresponding segments of every trajectory. The tracks are all started from corresponding seed points that originate from a small ROI. But that approach might not be suitable for whole brain fiber analysis (Ding et al., 2003). Another method with a similar approach came from Batchelor et al. (2006) where a proper choice of the seed points is made and the same sampling of the arc-length of the fiber bundle is done. Batchelor et al (2006) used Procrustes algorithm to register the trajectories.

The main problem of these algorithms is that they have strict constraints over the selected ROI, therefore seed points can not be applied for whole brain analysis. All solutions lack curve matching algorithms that enable analysis of the longer tracts over gross areas (Maddah et al., 2007). Maddah et al. (2007) proposes a statistical model of the fiber bundles that has been calculated as the mean and standard deviation of a parametric representation of the trajectories. In this model, the cluster of the trajectories are built by defining a Gamma mixture model and expectation maximization (EM) is applied to separate the cluster. The group analysis is then performed based on the points of distance maps for each cluster center. In addition,

a posterior membership function is defined to do the probabilistic assignment of the trajectories. The results of Maddah's algorithm is given in Figure 15.

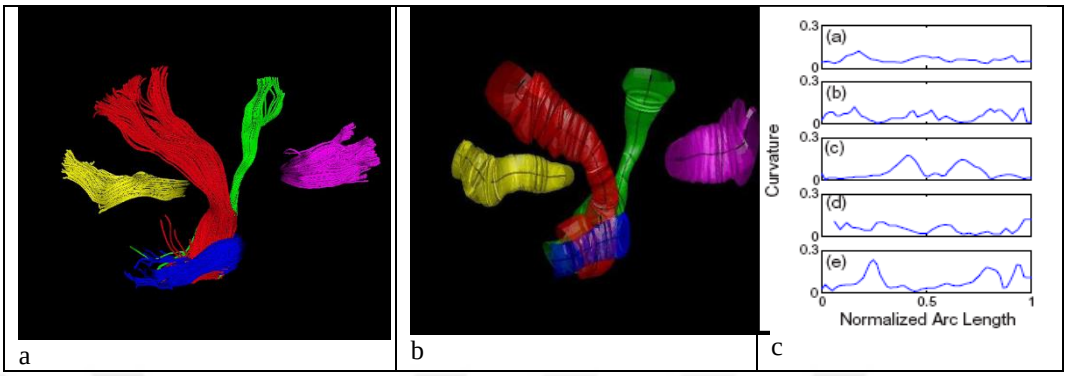

Figure 15: (a) Trajectories of 5 different clusters used for quantitative analysis: Splenium (yellow), corticospinal (red), corticobulbar (green), middle cerebellar peduncle (blue), and genu (magenta). (b) A model representation of the bundles as the mean trajectory and the isosurfaces corresponding to spatial variation of the clusters (c) Curvature of the cluster center along its normalized arc length for fiber bundles shown (Maddah et al., 2007).

2.2. Major Depression Disorder

Gelder et al. (2001) proposes classification of primary mood disorders to be done according to the nature and severity of symptoms during each episode, and by the course of the illness (Gelder et al., 2001). Major depression is the main subtype of the unipolar mood disorder category, it can be defined as one or more episodes of low mood and/or anhedonia as well as cognitive and somatic symptoms like fatigue, loss of appetite, sleep disorders (Harrison, 2002).

Drevets et. al. (2008) described MDD as a mood disorder that effects brain systems involved in the regulation of mood and emotional expression, reward processing, attention, motivation, stress responses, social cognition and neurovegetative function (e.g., sleep, appetite, energy, libido). Although depression has traditionally been viewed as an affective disorder, the last few decades of research have shown that MDD is also associated with considerable disturbances in cognitive functioning, including executive functions, attention, memory and psychomotor speed (McClintock et al., 2010; Castaneda et. al., 2008).

Studies point out that MDD mainly effects the brain networks responsible from regulating the evaluative, expressive and experiential aspects of emotional behavior (Phillips et al. 2003). These circuits include the limbic-cortical-striatal-pallidal-thalamic circuits (LCSPT), the orbital and medial prefrontal cortex (OMPFC), amygdala, hippocampal subiculum, ventromedial striatum, mediodorsal and midline thalamic nuclei and ventral pallidum (Drevets et al., 2008). The conditions that alter

transmission through these circuits in various ways can produce the pathological emotional symptoms (Drevets et al. 2008).

One of the well-structured neurocircuitry representations is provided by Drevets et al. (2001). They represent the regions implicated by studies of depression arising in the context of neurodegenerative illness or cerebrovascular disease. The studies implicate limbic–thalamo–cortical (LTC) circuits, involving the amygdala, medial thalamus, and orbital and medial PFC, and limbic–cortical–striatal–pallidal–thalamic (LCSPT) circuits, involving the components of the LTC circuit along with related parts of the striatum and pallidum as can be seen in Figure 16 (Drevets et al. 2001).

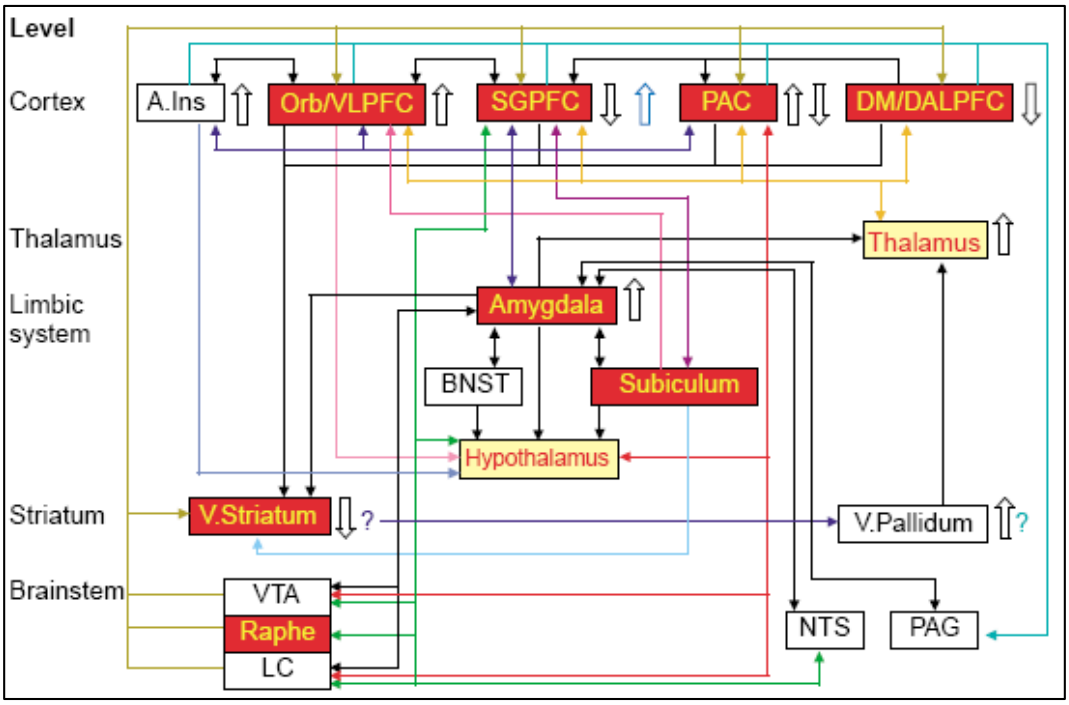

Figure 16: Anatomical circuits of mood disorders (Drevets et al. 2001).

In his work he describes these connections as follows: red rectangles represent the areas that have neuromorphometric and/or histopathological abnormalities in primary MDD and/or BD, bi-polar disease (Drevets et al. 2001). Thalamus and Hypothalamus have not been microscopically examined in mood-disordered patients, but structural abnormalities are suspected on the basis of the finding regarding third ventricle enlargement in children and adults with BD. Arrow direction shows the direction of abnormalities in CBF. The blue open arrow shows the direction of metabolic abnormalities. Solid lines show anatomical connections between structures. The direction of projecting axons (reciprocal connections have arrowheads at both ends) is indicated by closed arrows. Drevets concluded that in

MDD mainly prefrontal cortical areas are effected as shown in the figure (Drevets et al. 2001).

Other than Drevets, Mayberg (2004) states that major depressive disorder is a multidimensional, systems-level disorder. MDD affects mainly functionally integrated pathways. The MDD can be viewed as the net result of failed regulation of integrated system under circumstances of cognitive, emotional or somatic stress as can be seen in. Figure 17. Instability of this system by an unknown factor leads to disequilibrium state known as a major depressive disorder (Mayberg, 2004).

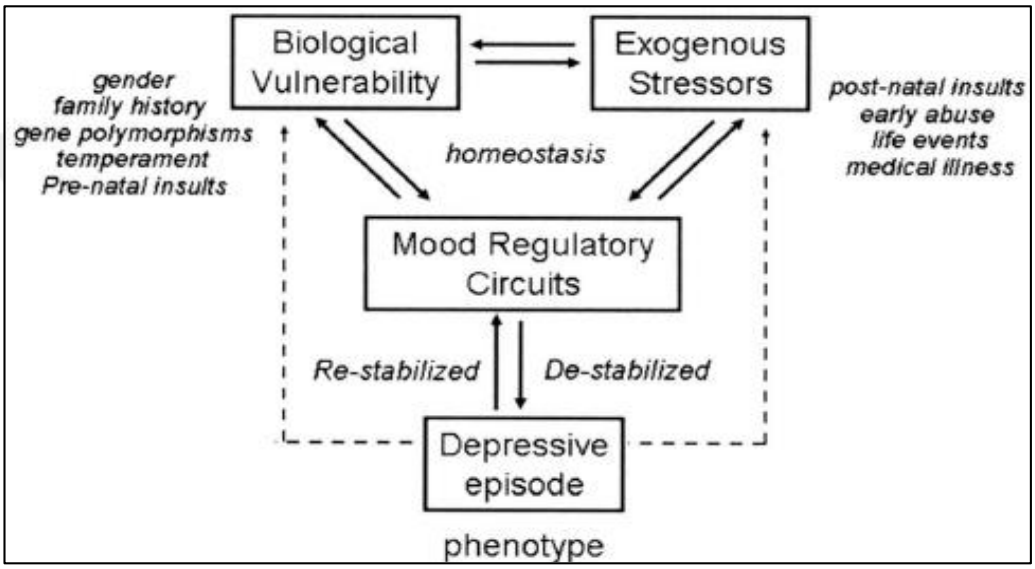

Figure 17: Putative sources of MDD. (Mayberg, 2006).

Mayberg (2004) also proposes one of the most accepted models of depression as seen in Figure 18, which is called the Limbic-cortical dysregulation model. Mayberg had collected data using PET in 3 behavioral states – base-line depressed (unipolar and Parkinson's disease patients), post-treatment (medication, cognitive therapy, placebo, surgery), and transient induced sadness (controls, patients, neurotics) – to form the basis of this schematic. Mayberg (2004) grouped the areas into 3 main compartments, cortical (blue), limbic (red) and subcortical (green). The model proposes that if there is modulation of dysfunctional limbic-cortical interactions (solid black arrows), relevant MDD patterns arises. Abbreviations: mF, medial prefrontal; dF, prefrontal; pm, premotor; par, parietal; aCg, dorsal anterior cingulate; pCg, posterior cingulate; rCg, rostral cingulate; thal, thalamus; bstem, brainstem; mOF, medial orbital frontal; Cg25, subgenual cingulate; Hth, hypothamus; Hc, hippocampus; a-ins, anterior insula; amyg, amygdala; pins, posterior insula. Numbers are Brodmann designations (Mayberg 2003).

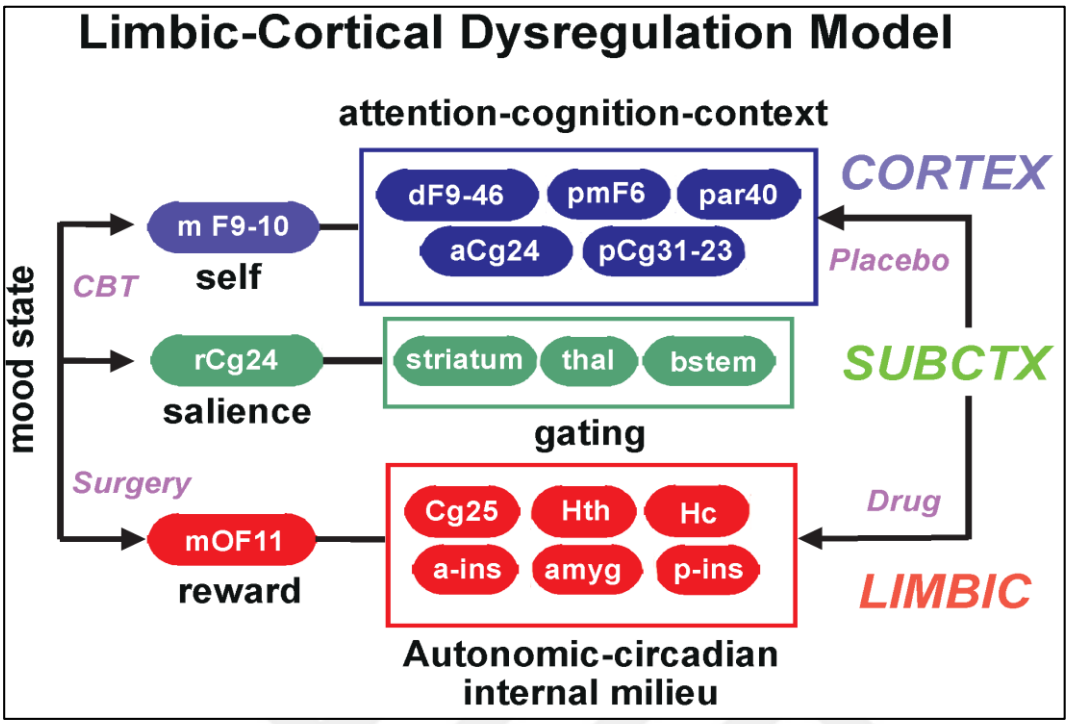

Figure 18: Mayberg's Model of Depression. (Mayberg, 2003).

Vago et al. (2011) collects various findings that use functional neuroimaging striatal pallidal- thalamic circuitry (CLIPST) as seen in Figure 19. Solid lines show anatomic connections; arrows show excitatory projections; terminal endings show strong inhibitory projections. The model also includes structures involved in the processing of fear, reward, attention, motivation, memory, stress, social cognition, and somatic functions. Depression may arise in the context of dysfunction of one or more of these regions, or because of a failure of coordinated interactions within or between the broader circuits. It is likely that different subtypes of depression are mediated by disorders localized to different brain areas and respond accordingly to different treatments.

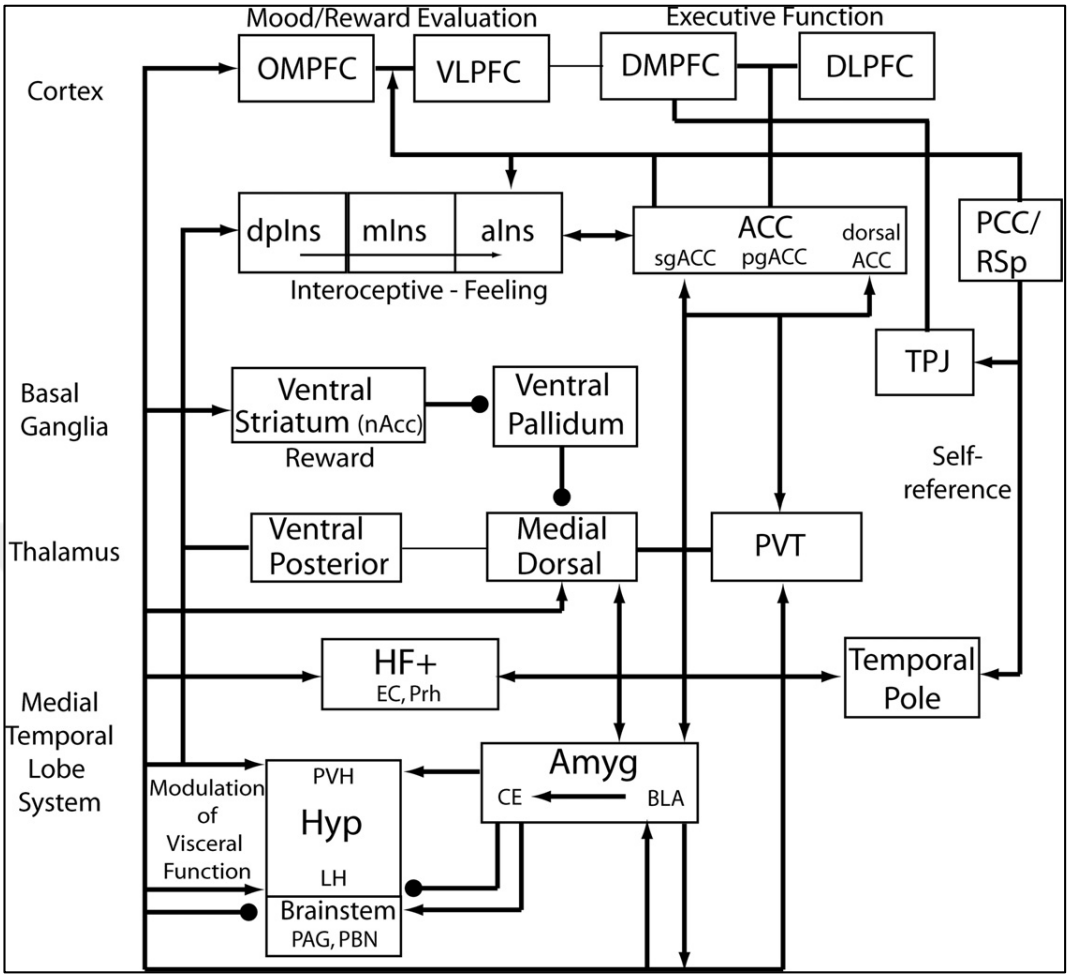

Figure 19: Corticolimbic-insular-striatal pallidal- thalamic circuitry for psychiatric disorders (Vago et al., 2011).

2.2.1. Neuropathology of Major Depression Disorder

Studies show that MDD has biological, psychological and social causes. Biological causes can be divided into two: brain chemicals and neurological abnormalities. Brain chemicals such as neurotransmitters, hormones and the endocrine system plays critical role in MDD pathology. Researchers have discovered associations between clinical depression and the function of three neurotransmitters: serotonin, norepinephrine, and dopamine, all related with functions that regulate emotions, stress, sleep, appetite, and sexuality. Limbic system and hypothalamus have been researched commonly in various researches.

On the other hand, researches on neurological abnormalities for MDD have become significantly important for MDD studies. There are several reports of cytoarchitectural alterations in white matter structures, characterized by a decrease in the number or density of glia, reductions in the size and density of neuronal populations and alterations in indices of synaptic terminals and dendrites.

Neuronal size and number: Neuronal size reflects the correlation of a neuron's efferent and afferent connections. Reduced neuronal size suggests that functional and/or structural disconnectivity can occur. Neuronal number and size changes may reflect functional implications and abnormal cell death or apoptosis (as in some neurodegenerative disorders) or may reflect altered neurogenesis (Cotter, 2003). However, the consistency of the findings are not enough to state that neuronal size or number is altered in bipolar disorder or major depressive disorder. Morphometrical analysis shows that neural size reductions have been observed in anterior cingulate cortex, the dorsolateral prefrontal cortex and the orbito frontal cortex. There may also be a reduced density of larger neurons in major depressive disorder, which explains reduced median or mean neuronal size.

Glial changes: Reduction in number and density of glial cell numbers have been observed in major depressive disorder. Glial cells have largely been ignored and traditionally been viewed as neuronal supporting cells in the central nervous system – so-called 'mind glue' – with their primary roles in glutamatergic neurotransmission, glucose metabolism and neurotrophic support (Cotter, 2003). However, recent studies have shown a cortical glial cell deficit in major depressive disorder. The changes have been observed in the orbitofrontal cortex, anterior cingulate cortex and dorsolateral prefrontal cortex. The results are verified with the functional and structural imaging, and as well as the neuropsychological investigations. Glial cells comprise three different cell types (microglia, oligodendroglia and astrocytes) and it is not yet clear which ones of these are responsible for the observed deficit in major depressive disorder. Support for the possibility that astrocyte deficits are responsible for the glial cell changes has been provided by a proteomics investigations based on the Stanley Foundation Brain series (Johnston-Wilson et al., 2000), although other researchers have also found evidence for reductions in markers of oligodendroglia.

Synaptic changes: Quantification of dendrites and synapses could reflect neuropatological changes for mood disorders. Cotter et al. (2003) reports that synaptophysin, complexin I and growth-associated protein-43 (GAP-43) are main factors. In his studies, he found that those three proteins are reduced in the anterior cingulate cortex in bipolar disorder, but only complexin II is reduced in major depressive disorder. His analysis also shows that GAP-43 and synaptophysin are not changed significantly in major depressive disorder in the prefrontal cortex. However, protein-25 and complexin I and II are found to be reduced in hippocampus in bipolar disorder, with no changes in major depressive disorder. As a result, cortical limbic regions are reported as the main areas that shows synaptic pathology (Cotter et al., 2003).

Subcortical white matter: MRI studies show that subcortical areas can be differentiated between control and patient groups' T2-weighted images for both major depressive disorder and bipolar disorders. White-matter hyperintensities are dominant in the deep white matter, around the basal ganglia and in the periventricular region (Harrison, 2002). Diffusion tensor imaging also verifies the findings where those hyperintensities show damaged areas of axonal organizations in white-matter tracts. It can be concluded that

mood disorder in these subjects may be due to interruption of the frontal cortical–subcortical connections.

2.2.2. White Matter Abnormalities in Major Depression Disorder

Evidence from recent neuroimaging and histological techniques shows that white matter abnormalities can be one of the reasons of dysfunction of the related neuro circuitry (Fields, 2008; Herrmann et al., 2008). Disruption of frontal-subcortical circuits like limbic–thalamo–cortical (LTC) circuits, involving the amygdala, medial thalamus, and orbital and medial PFC, and limbic–cortical–striatal–pallidal–thalamic (LCSPT) circuits, involving the components of the LTC circuit along with related parts of the striatum and pallidum may lead to a disconnection syndrome between frontal and subcortical regions, which correspond to the major depression (Tekin and Cummings, 2002; Alexopoulos et al., 2002). Skolov reports that expression of oligodendroglia-related genes is decreased in patients with MDD. The oligodendroglia-related genes are known to be important for forming white matter (Sokolov et al., 2007). Post-mortem studies have shown that deep WM abnormalities can occur in the dorsolateral prefrontal cortex (DLPFC) in major depressive patients (Regenold et al., 2007). Structural MRI studies in patients with major depression have revealed that increased WM hyperintensities are common and severe in frontal cortex (Taylor et al., 2003). There are also findings that are related with structural abnormalities. Ballmaier et al. (2004) reports that reduced WM volume is observed in the anterior cingulate cortex and the gyrus rectus. These findings show that integrity and connectivity of WM could affect major depression disorder and impair connection between limbic – frontal circuits that regulate emotional and cognitive functions.

2.2.3. DTI Studies of Major Depression Disorder

The earlier in-vivo studies related with MDD are mostly based on structural MRI. However recent studies have shifted to DTI where the main research topic is the white matter connectivity. Most of these studies are based on ROI analysis, although more recent ones focus on VBM and TBSS. Overall most of these studies state that the loss of integrity occurs in the WM fiber tracts of the frontal, temporal, and cingulate cortex of MDD patients (Nobuhara et al., 2004; Nobuhara et al., 2006; Taylor et al., 2004; Yang et al.,2007). ROI analysis considers only a very small region of the brain so it is subjected to miss the other related changes. There are also studies that cover whole-brain WM integrity in patients with MDD (Cullen et al., 2010; Zou et al., 2008; Yuan et al., 2007; Ma et al., 2007). Those studies are also aligned with previous findings that indicate MDD is not related with just some regions it is a result of a larger network of regional irregularities. (Drevets et al., 2008). Other related studies for MDD show reduction of FA values in parietal and occipital cortex (Yuan et al., 2007; Ma et al., 2007), in the internal capsule (Zou et al., 2008), and sagittal striatum (Kieseppa et al., 2010) or WM tracts such as superior longitudinal fasciculus (SLF) (Zou et al., 2008) and uncinate fasciculus (Cullen et al., 2010).

Sexton et al. (2015) had made an extensive review of diffusion tensor imaging studies in affective disorders. One hundred twenty citations were retrieved from EMBASE and MEDLINE. 54 of them have used diffusion tensor imaging and among them 27 articles consist comparison with healthy controls. The results are given in Figure 20 and Figure 21.

		Data Analysis				Results	
Study	Diagnosis	Method	Anisotropy	Diffusivity	ROI/Tract	Significant Difference in Anisotropy	Significant Difference in Diffusivity
Adler *et al.* (2004) (57)	BP	ROI	FA	TADC	Frontal	↓ Frontal	No significant differences
Adler *et al.* (2006) (56)	BP	ROI	FA	TADC	Frontal, posterior	↓ Frontal (L)	No significant differences
Bae *et al.* (2006) (58)	MD	ROI	FA	ADC	Frontal, CC, IC	↓ Frontal (L, R)	No significant differences
Beyer *et al.* (2005) (62)	BP	ROI	FA	ADC	Frontal	No significant differences	↑ Frontal
Frazier *et al.* (2007) (68)	BP	ROI	FA	NA	Frontal, CC, SLF	↓ Frontal (L, R), CC (R), SLF (L, R)	NA
Haznedar *et al.* (2005) (53)	BP	ROI	RA	NA	Frontal, SLF, FOF, IC	↓ IC (L, R), FOF ↑ Frontal (R)	NA
Houenou *et al.* (2007) (59)	BP	Tractography	FA	ADC	Frontal, Temporal, UF Pons, Cerebellum, P-C	No significant differences	No significant differences
Li *et al.* (2007) (10)	MD	ROI	FA	NA	Frontal	↓ Frontal (L, R)	NA
McIntosh *et al.* (2008) (64)	BP	Tractography	FA	NA	UF, ATR	↓ UF, ATR	NA
Nobuhara *et al.* (2004) (94)	MD	ROI	FA	NA	Frontal, Temporal, CC	↓ Frontal, Temporal	NA
Nobuhara *et al.* (2006) (95)	MD	ROI	FA	NA	Frontal, Temporal, Parietal, Occipital, CC	↓ Frontal, Temporal	NA
Pavuluri *et al.* (2009) (63)	BP	ROI	FA	ADC	CC, IC, SLF, ILF, ACR, CG	↓ ACR	↑ CC
Steele *et al.* (2005) (96)	MD	ROI	FA	NA	Brainstem	No significant differences	NA
Sussmann *et al.* (2009) (65)	BP	ROI	FA	NA	IC, UF	↓ IC (L), UF (L, R)	NA
Taylor *et al.* (2001) (60)	MD	ROI	FA	ADC	Frontal, Parietal, Caudate, Thalamus	No significant differences	No significant differences
Taylor *et al.* (2004) (97)	MD	ROI	FA	NA	Frontal, Occipital	↓ Frontal (R)	NA
Taylor *et al.* (2007) (69)	MD	Tractography	FA	NA	UF	No significant differences	NA
Wang *et al.* (2008) (71)	BP	ROI, VBA[a]	FA	NA	CC	↓ CC	NA
Wang *et al.* (2008) (70)	BP	ROI	FA	NA	CG	↓ CG	NA
Yang *et al.* (2007) (98)	MD	ROI	FA	NA	Frontal, Temporal, CC	↓ Frontal (L, R), Temporal (R)	NA
Yurgelun-Todd *et al.* (2007) (54)	BP	ROI	FA	Tr	CC	↑ CC	No significant differences

Figure 20: ROI based MDD analysis (Sexton 2015).

		Data Analysis			Results			
					Significant Difference in Anisotropy		Significant Difference in Diffusivity	
Study	Diagnosis	Analysis Method	Anisotropy	Diffusivity	Anatomy	Talairach Coordinates	Anatomy	Talairach Coordinates
Bruno *et al.* (2008) (61)	BP	VBA	FA	Mean diffusivity	↓ Temporal/Occipital (L)	(42, −70, −2)	↑ Frontal (L, R)	(−20, 30, 60), (18, 28, 8), (16, −26, 26)
Kafantaris *et al.* (2009) (79)	BP	VBA	FA	ADC	↓ Temporal (L, R)	(−32, −50, 3), (−47, −36, −7), (30, −59, 8)	↑ Parietal (L, R)	(−51, −26, 21), (−40, −29, 44), (−13, −62, 42), (12, −54, 52), (14, −59, 44)
					↓ Frontal (R)	(20, 18, −1)	↑ External capsule (R)	(29, −12, 16)
					↓ Occipital (L)	(−36, −59, −7)	↑ Occipital (R) ↑ Frontal (L, R)	(32, −72, 22) (−11, 19, −2), (9, 21, −4)
							↑ Temporal (L)	(−31, −61, 26)
Ma *et al.* (2007) (93)	MD	VBA	FA	NA	↓ Frontal (R) ↓ Occipito-temporal (L) ↓ Parietal (R)	(36, 49, 10) (−42, −56, −1) (24, −47, 41), (42, −65, 27)	NA	NA
Steele *et al.* (2005) (96)	MD	VBA	FA	NA	↓ Temporal (R)	(61, −36, −18)	NA	NA
Sussmann *et al.* (2009) (65)	BP	VBA	FA	NA	↓ STR ↓ UF/ILF[SVC] ↓ ATR/CC[SVC] ↓ ATR[SVC]	(−19, −7, 45) (25, 15, −2) (−19, 21, 23) (−19, 32, 22)	NA	NA
Versace *et al.* (2008) (55)	BP	TBSS	FA	Longitudinal, Radial[a]	↓ UF (R)	(13, 40, −14)	↑ Radial UF (R)	(13, 40, −14)
					↑ UF (L)	(−21, 21, 1), (−32, 16, −12), (−32, 16, −12)	↑ Longitudinal UF (L)	(−22, 25, 1)
					Optic radiation (L)	(−8, −78, 26), (−13, −76, 10), (−37, −42, −32)	↓ Radial UF (L)	(−33, 21, −17), (−37, 20, −13)
					↑ ATR (R)	(2, −8, 1)	↑ Longitudinal optic radiation (L)	(−8, −82, 27)
Yuan *et al.* (2007) (91)	MD	VBA	FA	NA	↓ Frontal (L, R) ↓ Temporal (L) ↓ Parietal (R) ↓ Occipital (L, R) ↓ Putamen (R) ↓ Caudate (R)	(−52, 19, 22), (13, 12, 47) (−57, −8, −10) (47, −52, 40) (−26, −82, −5), (34, −75, 11) (30, −10, 8) (21, 27, 4)	NA	NA
Zou *et al.* (2008) (66)	MD	VBA	FA	NA	↓ IC (L) ↓ SLF (L)	(−13, 18, 10) (−33, −47, 29)	NA	NA

Figure 21: VBA and TBSS based MDD analysis (Sexton 2015).

19 studies out of 27 are based on ROI and tractography analysis, 5 out of 27 used VBA method and only one of the studies used TBSS method. 2 studies have used both ROI and VBA analysis.

In these studies, majority of studies (21 out of 27) found at least one region that has significant reduction in anisotropy. Among those regions the frontal and temporal lobes or more specially the uncinate fasciculus, was the most common. The connections between the parietal and occipital lobes were only found to be significant by global analysis methods. In summary, there is no lateralization of anisotropy reductions. On the other hand, there are some studies that show increase in anisotropy (3 out of 27). Frontal lobe, corpus callosum, uncinate fasciculus, optic radiation and anterior thalamic radiation were found to be significantly increased and only limited to bipolar disorder.

11 out of 27 studies investigate affective disorders where 6 studies could not find difference between control and patients. Only 4 studies detected change in diffusibility in bipolar disorder.

ADC also has been used to compare control and patient images. Only 3 of those studies reported that ADC has increased. Radial and longitudinal diffusivity are also compared in some of the studies; increased radial diffusivity is found for affective disorders. Increased longitudinal diffusivity and decreased radial diffusivity were detected in regions where increased FA has been found. A global network change has been detected in superior frontal white matter, which contains fibers of the DLPFC and ACC circuits. Thus, all those findings support that for affective disorders white matter abnormalities constitute one of the factors. It is also shown that the network between frontal and subcortical regions contains the main areas that have been affected (Sexton et al. 2009).

CHAPTER 3

HISTOGRAM BASED GROUP ANALYSIS METHOD AND RESULTS

This chapter describes a novel DTI group analysis method. A fully automatized pipeline has been implemented and presented in INCF Neuroinformatics Congress in Stockhold, Sweden (Metin and Gokcay 2013). The Method has been applied to a limited set of subjects. Method section describes the preprocessing, processing and analysis pipelines, then the results are presented and discussed.

3.1. Method

The focus of this study is to develop a group analysis for diffusion imaging that uses connectivity as well as diffusibility information (fractional anisotropy). A full automized pipeline has been developed and Amygdala connections have been chosen for analysis. Since Amygdala is regarded as one of the most important structures that effects emotion, the connectivity analysis of Amygdala can be important discriminative factor that changes between MDD and control subjects. For MDD patients, it can be assumed that the pathways between Amygdala and neighboring structures will be affected.

The proposed group analysis method in this study could not be regarded as a distinct cut from other group analysis methods. However, connectivity-based approach, analysis depends on not only FA values but also fiber tract lengths can be regarded novel technique.

3.1.1. Method Pipeline

The overall pipeline has been designed using Connectome Mapper pipeline. The pipeline has been revised and improved by changing and adding some steps. The pipeline is not homogeneous, it uses FSL (FLIRT, FNIRT for registration) (Smith, 2004), Freesurfer (for segmentation and parcellation) (Fischl, 2002), Camino (Cook, 2006) for tractography. At the end of the process, the pipeline traverse connectivity graph building, FA matching, Histogram building and group analysis technique that has been implemented for this thesis work. The overall pipeline can be seen in Figure 22.

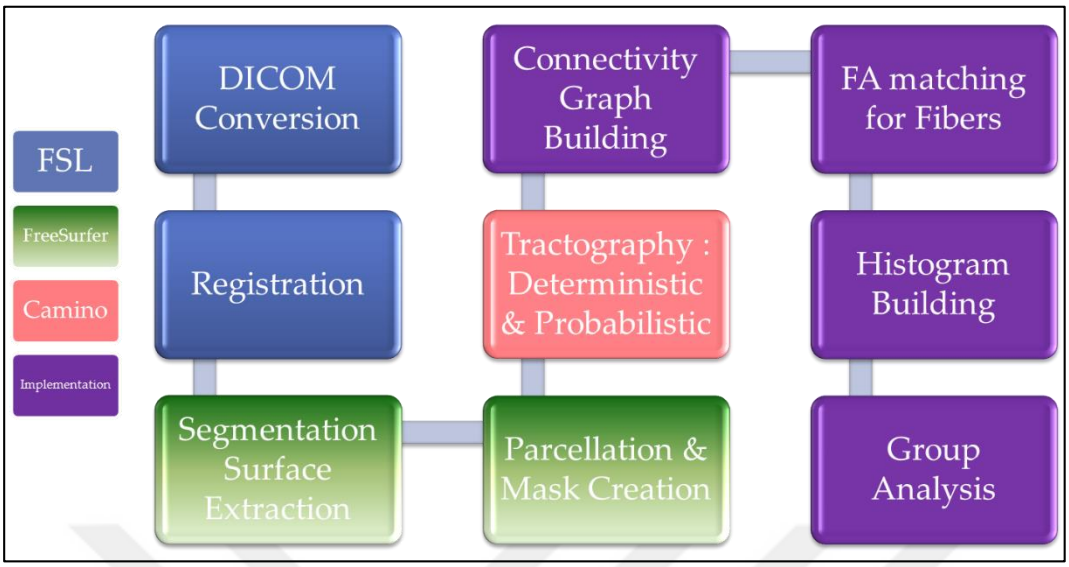

Figure 22: Overall pipeline.

The pipeline starts with converting DICOM images to NHDR and Nifti file format. NHDR file format is supported by NA-MIC (National Alliance for Medical Image Computing) and mostly used for DWI images. NHDR file is in fact an ascii file representing the header of raw data. NRRD (Nearly Raw Raster Data) file holds the combined form both raw data and ascii header. NIfTI-1 is adapted from the widely Analyze file format and is supported by Neuroimaging Informatics Technology Initiative. Nifti can be stored in dual file (.hdr & .img) or single file (.nii) storage.

The next step is correcting the motion and eddy current artifacts. The application of strong field gradients required for diffusion tensor imaging (DTI) result in eddy currents that induce significant direction-dependent distortions in the resulting images. Eddy currents in the gradient coils induce (approximate) stretches and shears in the diffusion weighted images. To create analogy Eddy current correction of DTI data can be regarded as motion correction of fMRI data.

The next step is intra subject registration of T1, T2 and DWI images. In literature, the registration has been done between T2 image and DWI B0 images, and then T1 is registered on T2. So that T1, T2 and DWI images become aligned. For all registration steps FSL's FLIRT and FNIRT routines has been used. All of the images has been registered on DWI B0 image so that we can state that all image operations has been done on diffusion step. This method eliminated the problem of transforming diffusion tensors.

The next step is applying segmentation and parcellation steps of FreeSurfer using recon_all command. These steps transform patient on uniform space and try to segment white and gray matter as well as cortical and subcortical structures. The parcellation step reveals 83 distinct cortical and subcortical structures of the brain.

The tractography step consists of sub steps, DTI tensor estimation and tractography. For the entire tractography step, Camino Tool, which has been developed by University College London, has been used. DTI tensor estimation creates (estimates) tensors from DWI image. Weighted Least Square Estimation technique with shifting negative eigenvalues option has been used. For tractography three different techniques has been used: Deterministic tractography (Mori, 2003), Bayesian stochastic tractography (Friman, 2006) and probabilistic index of connectivity probabilistic tractography (Parker, 2003; Parker, 2005).

The next steps of pipeline was developed for the thesis work. ITK, VTK, Boost Graph, GraphViz are some of the frameworks and libraries that has been used. Except from Group Analysis, all of the remaining steps are written in C++, Group Analysis step has been written using Matlab.

Connectivity Graph Building step accepts following inputs:

- Fiber tracts that are output of Camino tractography steps and in VTK Poly Data format. VTK Poly Data Format holds data in polygon representation where each fiber consists of a number of voxel points that fiber passes.
- ROI file that is the output of FreeSurfer recon_all parcellation step. The file is in NRRD format. Each ROI are represented by different integer ID.
- ROI ID: filters the start area of fiber tracts: For Example, Amgydala
- Filter: Consider only one hop neighbor.

The algorithm of Connectivity Graph Building passes for each fiber tracts, labels crossing ROI areas, building weighted directed graph, where each node represents ROI and each edge represents the number of connections (tracts) that passes ROI A and goes to ROI B. It is also possible that any fiber tracts can pass more than one ROI. If Filtering flag is set on, it filters the results where only one hop neighbor are consider that either starts or end in given ROI.

The next is FA matching for Fibers, this step accepts following inputs:

- Connectivity Graph: for each edge voxel coordinates are provided
- White matter mask that is output of FreeSurfer segmentation step. The positive integer values for voxels represents white matter areas.
- FA scalar image: that is output of DTI tensor estimation step
- Start ROI ID: filters the start area of fiber tracts: For Example, Amgydala
- End ROI ID: filters the start area of fiber tracts: For Example, Putamen
- Filter: Consider only one hop neighbor.

FA matching for fibers step passes for each fiber tracts on FA scalar image. FA images and fiber space are manually aligned so that for each voxel coordinates in Fiber tract will have corresponding FA value in FA image. This step considers only white matter areas that have been given in white matter mask. The output of FA matching is CSV file where each row holds fiber ID, voxel coordinates, FA value and tract length. Tract length is calculated during traversing the fiber tract. Filter

field filters the result as given in Connectivity Graph Building step. Figure 23 show an example visualization of matching FA values on each fiber tract.

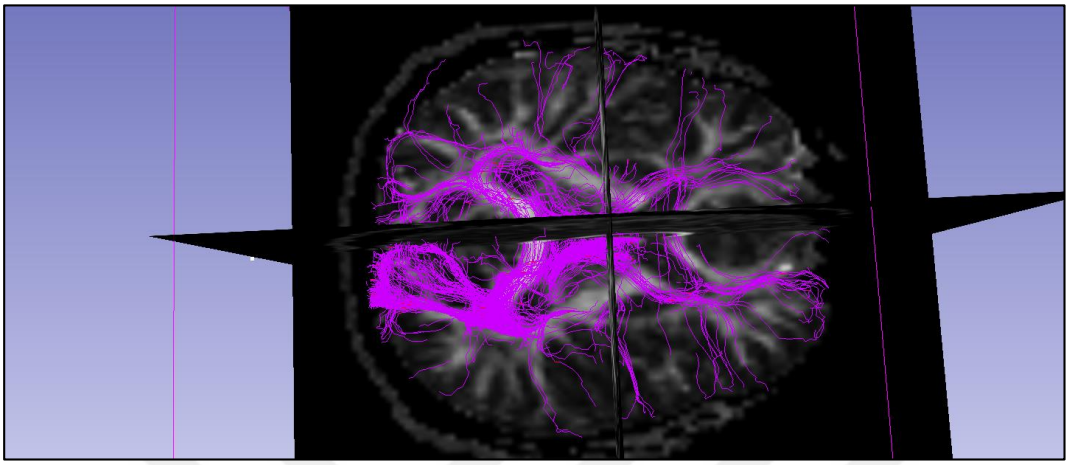

Figure 23: FA values that passes on the tracts.

The next step is histogram building. This step uses Matlab hist3 function, that builds 3D histogram by pining the elements of the m-by-2 matrix X into a m-by-n grid of equally spaced containers, and outputs a histogram. Each column of X corresponds to one dimension in the bin grid. The histogram is build according to FA values and tract lengths. So that each m-by-n grid element holds number of voxels that has specific FA value a tract lengths. Figure 24 hows an example of such 3d histogram.

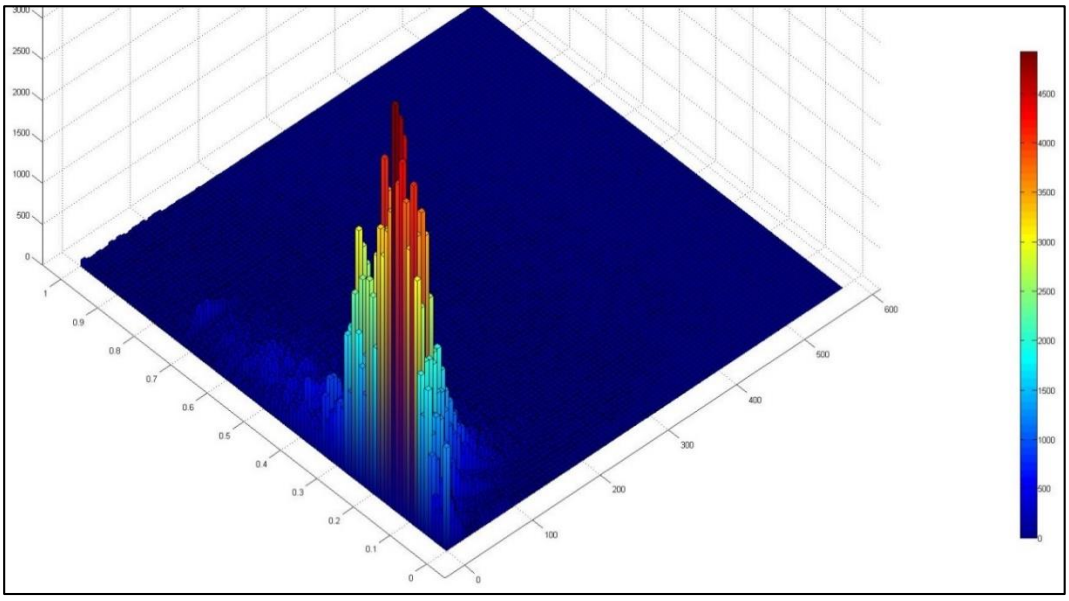

Figure 24: 3d Histogram for fiber tracts of one subject. The x-axis bins are for fiber tract length and y-axis bins are for FA values.

The histogram is projected on x-y axis to build a heat map. Y-axis represents FA values, X-axis represents tract lengths. Figure 25 shows an example of generated heat map.

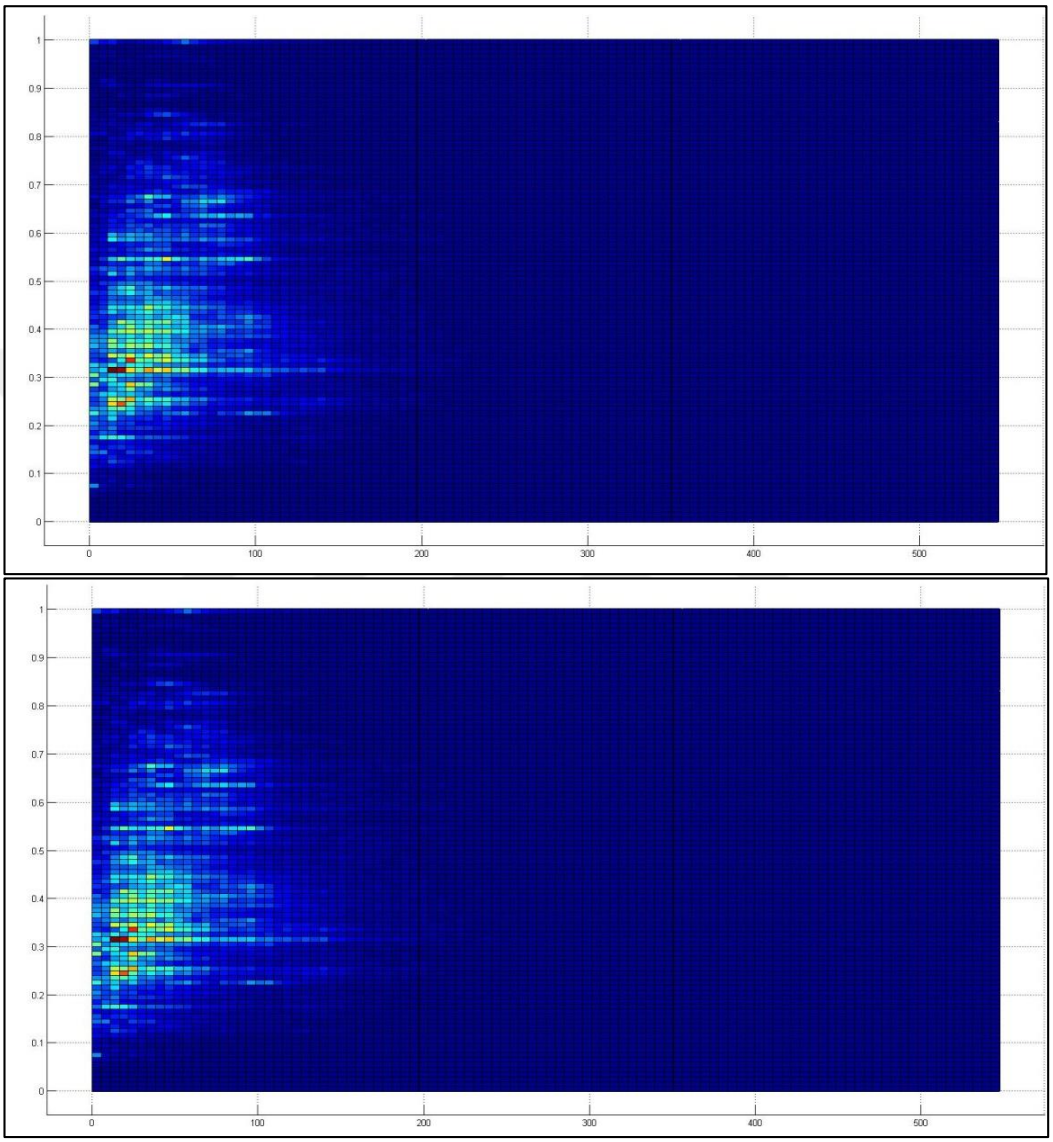

Figure 25: Heatmap for the same histogram in 2d.

After generating such heat map for all subjects, a t-test has been applied on each bins. The p value has been chosen as 0.005. Figure 26 shows a map for fiber tracts. The red squares represent the histogram pins that statically significantly differs control subjects with MDD patients. Figure 27 shows a map of p values for each histogram pins. The more reddish square represents the less p value.

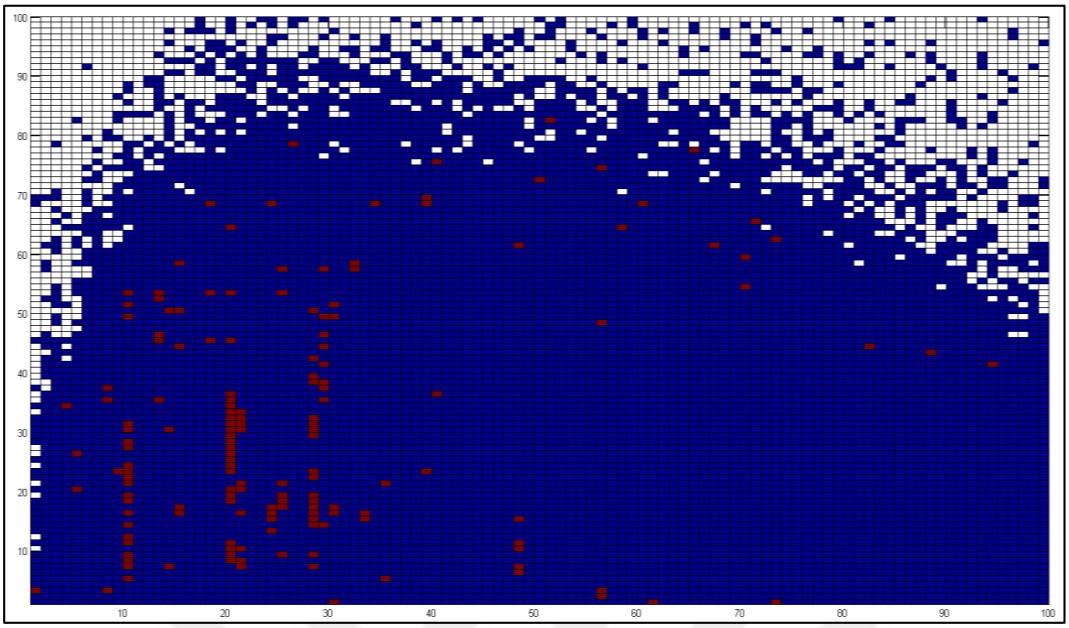

Figure 26: Map for fiber tracts for each FA and fiber length match. Red square represents the histogram pins that statistically differs control subjects with MDD patients ($p<0.05$).

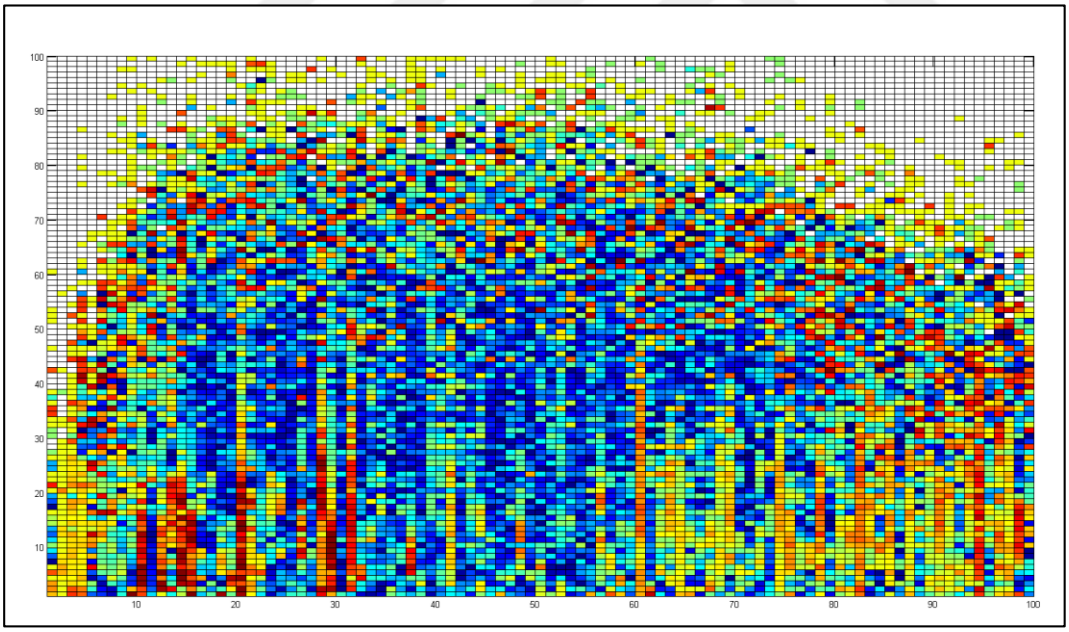

Figure 27: Map for p values for a connection histogram. The more reddish, the more significantly different values.

3.2. Experiments and Results

3.2.1. Subjects and Data Acquisition

For the test of histogram based group analysis, the data set consist of 2 MDD patients and 4 control subjects has been used. The scans have been acquired using Siemens MAGNETOM 3 Tesla scanner. Anatomical T1-weighted images were collected using a high-resolution gradient echo sequence. T2 sequence has been collected using square voxels in axial directions. DTI sequence consisted of 7 b0 and 45 gradient directions has been acquired for each subject.

3.2.2. Results

The whole pipeline that has been described in section 3.1 has been applied to 4 MDD patient and 6 control subject. The ROI are selected by evaluating the weighted graphs for each subject. It is found that the high correlation of connection numbers are common for all subject for following connections. Some of the connection graphs are given in Figure 28.

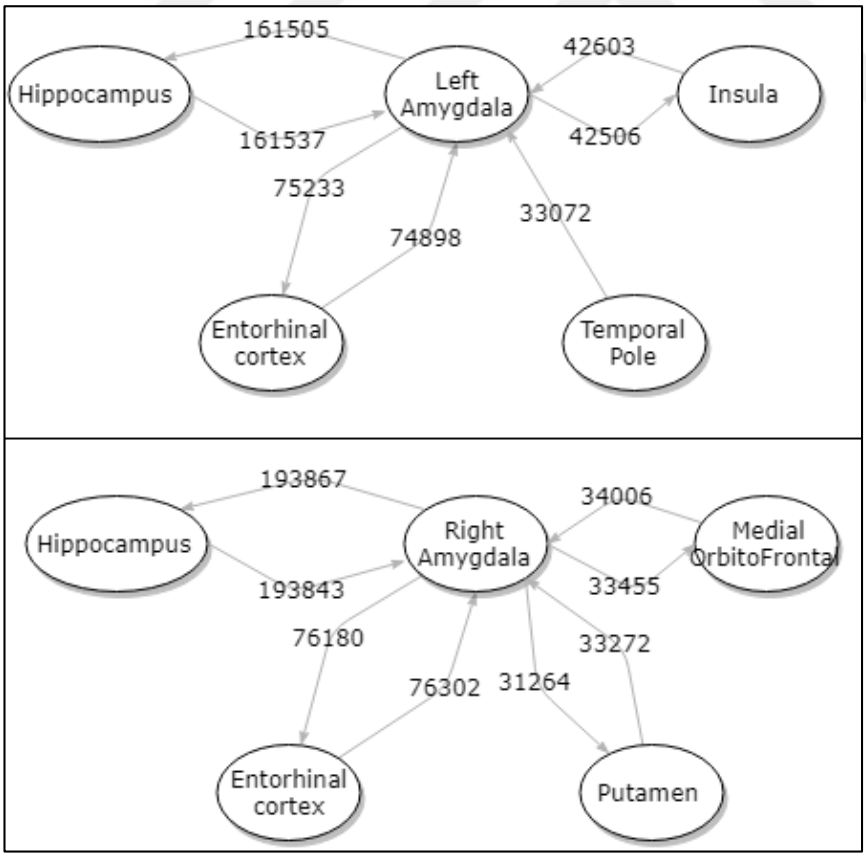

Figure 28: Amygdala connection graphs (number of connections are averaged over the subjects).

For each connection, 3d histograms are calculated and t-tests are applied for each histogram pins. As can be seen in Figure 29, for lower FA values (0.10-0.30) there is a pattern that for the MDD patients' fiber tracts regardless of the tract length FA values are significantly bigger than control patients. On the other hand for higher FA values (0.9) the MDD patients have significantly lower connections than control patients for lower tract length.

As can be seen in Figure 30 the pattern is much more significant than entorinal cortex, for lower FA values (0.10-0.30) there is a pattern that for the MDD patients fiber tracts regardless of the tract length FA values are significantly bigger than control subjects.

The situation differs with left amygdala connections with Hippocampus and Insula. Nearly all range of FA values, it can be seen that the number of fiber tracts of control subjects are significantly bigger than MDD patients.

The pattern is almost the same for right amygdala. The only connection that has higher number of connections for low FA values are Entorhinal cortex connections. The summary of the evaluation is given in following tables.

Table 1: Histogram based analysis of amygdala connections.

Left Amygdala with Entorhinal cortex		Low Tract Length	HighTract Length
	Low FA	↑	
	High FA	↓	

Left Amygdala with Temporal Pole		Low Tract Length	High Tract Length
	Low FA	↑	
	High FA	↓	

Left Amygdala with Insula		Low Tract Length	High Tract Length
	Low FA	↓	↓
	High FA	↓	↓

Left Amygdala with Hippocampus		Low Tract Length	High Tract Length
	Low FA		↓
	High FA	↓	↓

Right Amygdala to Medial OrbitoFrontal		Low Tract Length	High Tract Length
	Low FA	↓	↓
	High FA	↓	↓

Right Amygdala to Entorhinal cortex		Low Tract Length	High Tract Length
	Low FA	↑	↑
	High FA	↓	↑

Right Amygdala to Putamen		Low Tract Length	High Tract Length
	LOW FA	↓	
	HIGH FA	↓	

Right Amygdala to Hippocampus		Low Tract Length	High Tract Length
	LOW FA	↓	↓
	HIGH FA	↑	↓

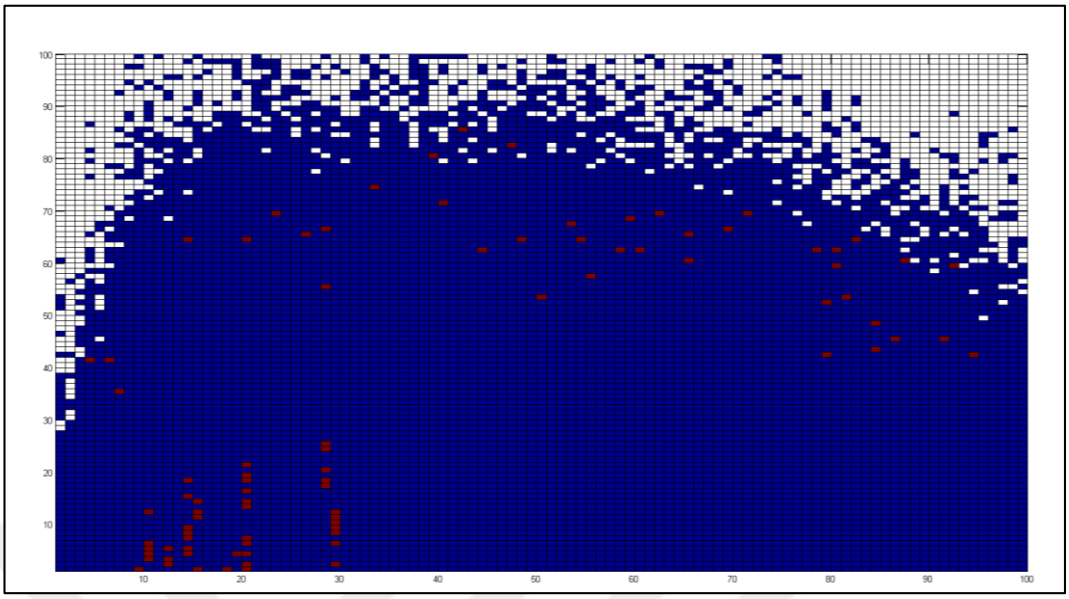

Figure 29: Left amygdala with entorhinal cortex.

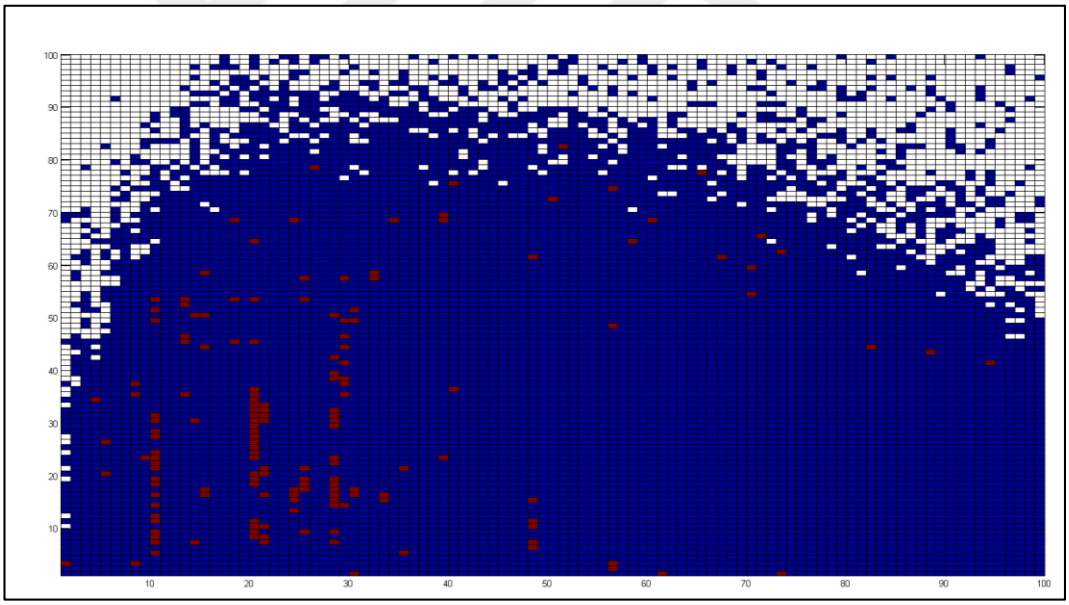

Figure 30: Left amygdala with temporal pole.

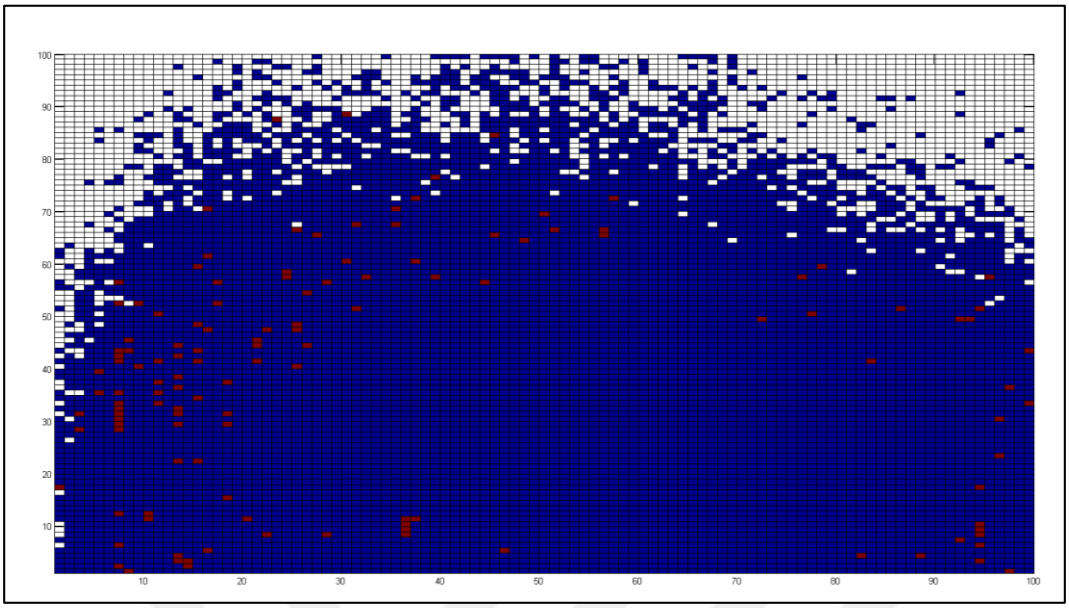

Figure 31: Left amygdala with insula.

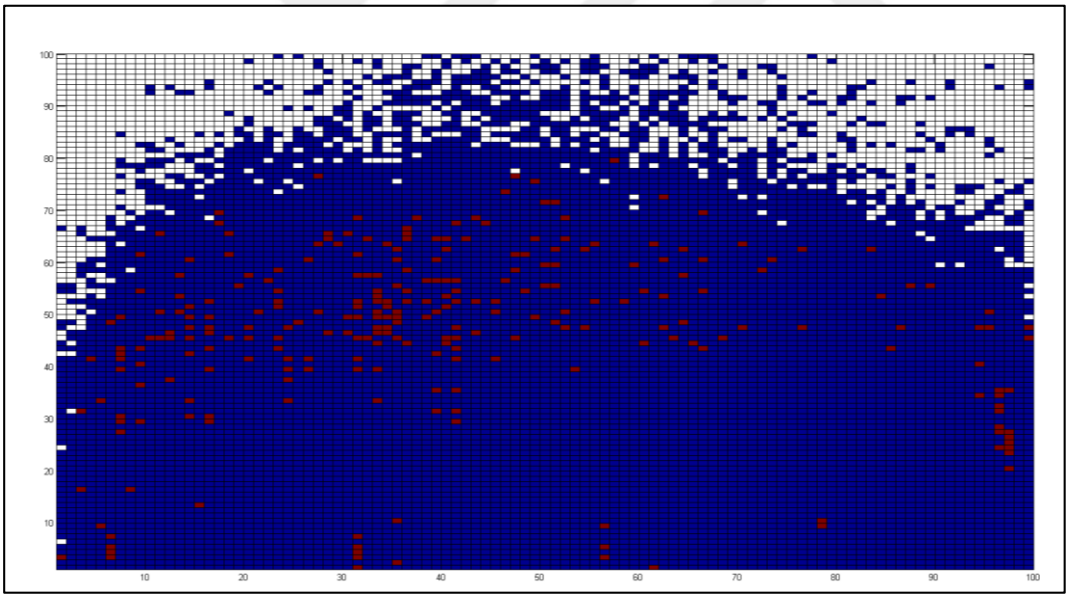

Figure 32: Left amygdala with hippocampus.

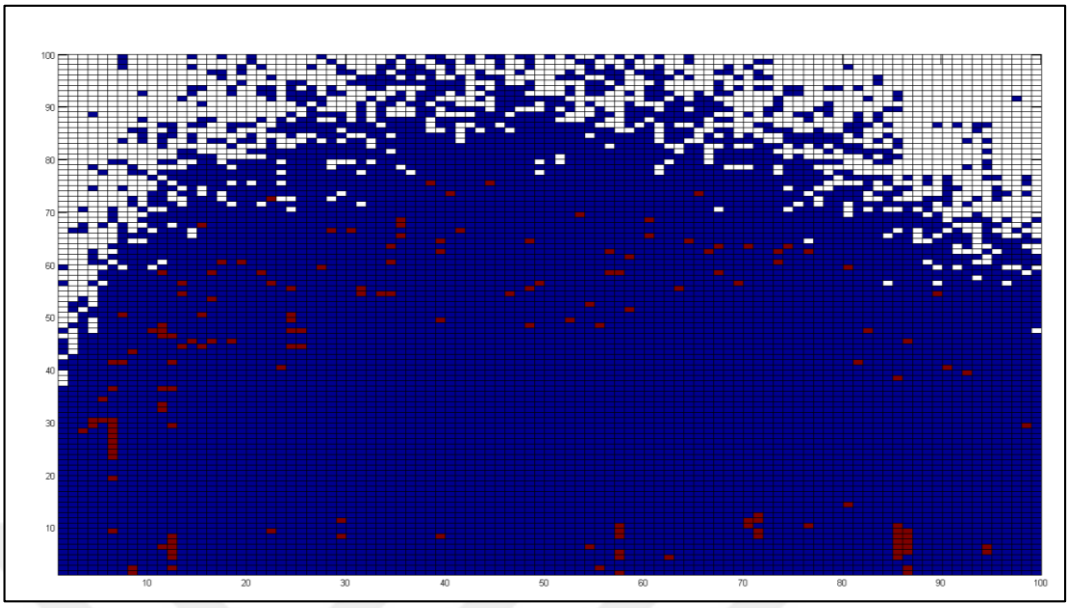

Figure 33: Right amygdala with medial orbitofrontal.

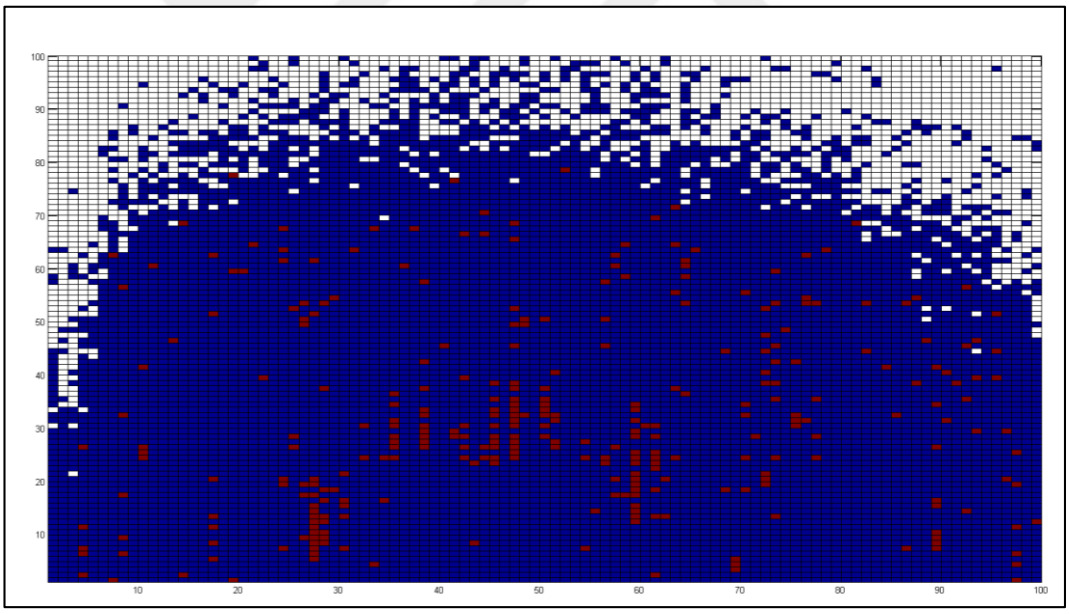

Figure 34: Right amygdala with entorhinal cortex.

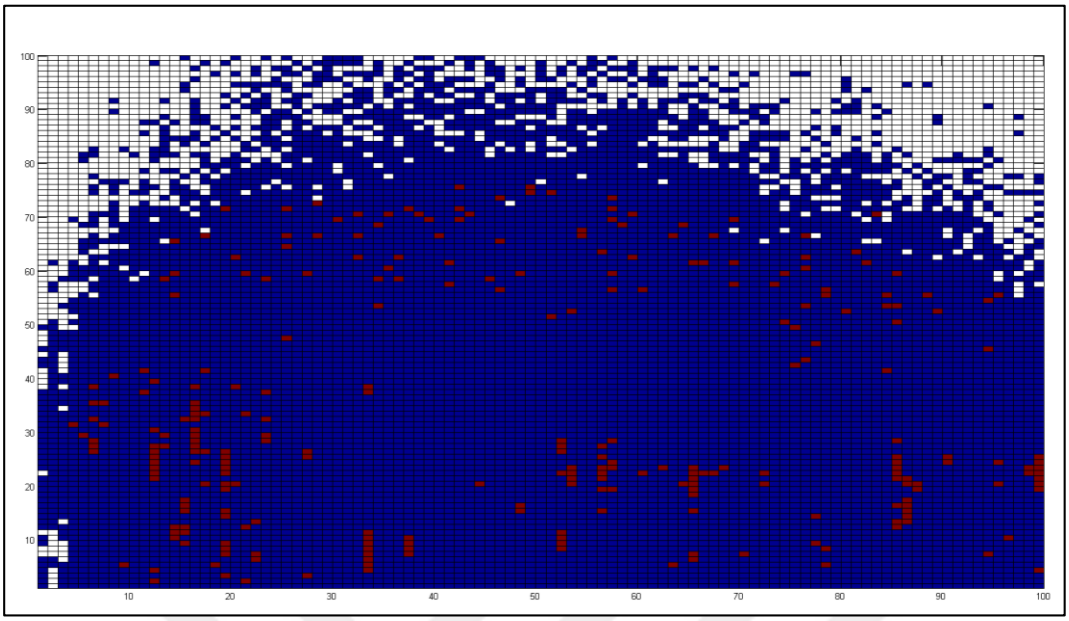

Figure 35: Right amygdala with putamen.

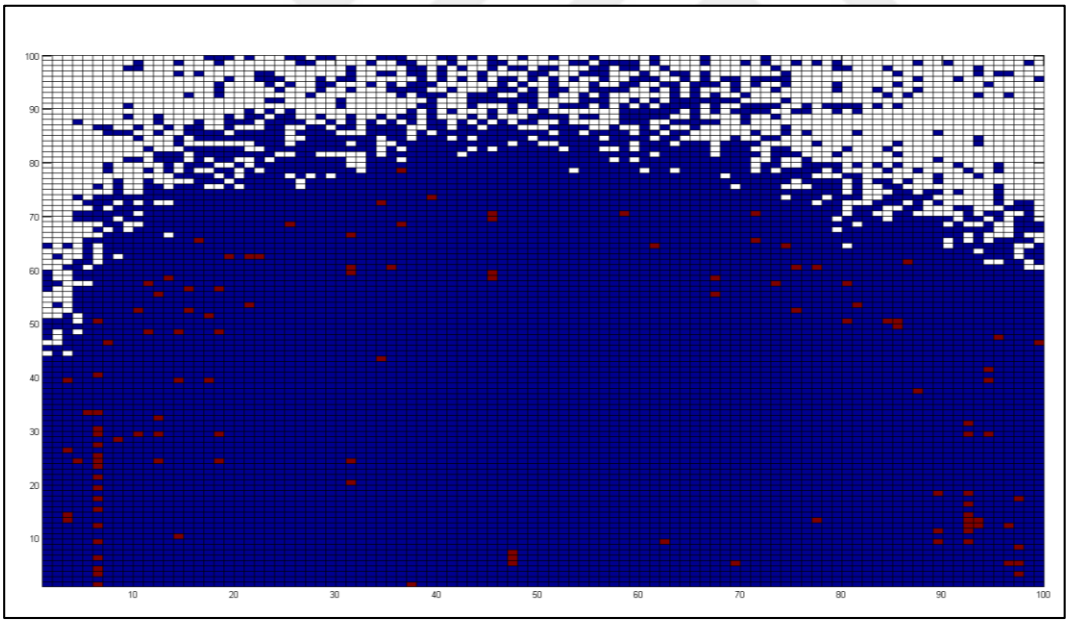

Figure 36: Right amygdala with hippocampus.

CHAPTER 4

TRACT PROFILING AND DIRECTIONAL STATISTICS METHOD AND RESULTS

This chapter describes a new DTI group analysis technique that can be applied though fiber tracts. This new method called tract profiling and directional statistics (TPDS) has been implemented. As a test set, the method has been applied to subject's dataset with control and MDD patients. A part of this study has been presented in Human Brain Mapping, Barcelona, Spain (Metin and Gökçay 2014). Later, TPDS method has been published in Frontier Neuroscience 2021 (Metin and Gokcay 2021).

4.1. Method

Directional statistics, which is a statistic of vectors and directions, deals with observations on compact Riemannian manifolds. Thus, it can encapsulate much more information than scalar metrics about the diffusion. Without the limitation of scalar statistics, one can evaluate dispersion and coherence values among the populations, fit directional statistics model to the data and hopefully does hypothesis testing for group based studies. Previously, directional statistics have been mainly used to analyze paleomagnetic data, which also consist of principal paleomagnetic direction and uses vector space.

There are a number of statistical distributions that can be used in directional data. Von Misses circular distribution is one of them which can be used for 2D data. Fisher distribution is a probability distribution on the two-dimensional unit sphere S2 in $\mathbb{R}^3$which is uni-modal and the vectors disperse around mean direction symmetrically. Dimroth-Watson distribution, which is commonly known as Watson distribution, is bi-modal and symmetrical around mean direction. Kent distribution is uni-modal and elliptical that assumes the vectors of the model are dispersed elliptically and Bingham distribution is bi-modal and elliptical (Fisher, 1993; Mardia, 2000).

Although, directional statistics have been used in analysis of DTI previously (Hutchinson, 2012; Schwartzman, 2005), To the best of author knowledge, there is no related work to evaluate which distribution fits best to describe principal

diffusion characteristics of DTI tensors. The assumptions and requirements of each directional distribution differ, that requires carefully analysis of PDD's according to directional statistics.

The objective of this work is to investigate measure of goodness of fit statistic for Fisher, Watson, Kent and Bingham distributions for different diffusion characteristics of WM and GM segments.

4.1.1. Directional Distributions and Parameter Estimates

4.1.1.1. Fisher Directional Statistics

It has been developed by R. A. Fisher for statistical analysis of vectors. Originally the statistic is defined in 2D vectors it can be easily extended to be used in 3D. If φ is taken as angle about true mean direction, the probability of a direction within an angular area, dA, can be expressed as $P_{dA}(\alpha)dA = P_{dA}(\alpha)\sin(\alpha)\,d\alpha d\phi$ this can normalized to probability distribution as

$$\int_{\phi=0}^{2\pi}\int_{\alpha=0}^{\pi} P_{dA}(\alpha)\sin(\alpha)\,d\alpha d\phi = 1$$

And the probability Pdα of finding a direction in a band of width dα between α and α + dα is given by:

$$\int_{\phi=0}^{2\pi} P_{dA}(\alpha)dA = 2\pi P_{dA}(\alpha)\sin(\alpha)d\alpha$$

This result can be simplified as $P_{dA}(\alpha) = \frac{K}{2\pi\sinh(K)}e^{(K\cos(\alpha))}$ Where K is constant that defines dispersion of the data.

In Fisher statistics, the resultant vector, R is calculated as regular vector sum of the vectors under population of vectors. The mean direction is a unit vector that is in the same direction with R.

$$\bar{x} = \frac{\sum_i x_i}{R},\ \bar{y} = \frac{\sum_i y_i}{R}, \bar{z} = \frac{\sum_i z_i}{R}$$

One measure of the dispersion of a population of directions is the precision parameter, κ. From a finite sample set of directions, κ is unknown, but a best estimate of κ can be calculated by

$$K \cong k = \frac{N-1}{N-R}$$

This means that as R come close to N K will be bigger, means that the dispersion is smaller. As R goes to 0, k come close to 1 which is uniform distribution around the sphere that means high dispersion.

The circle of confidence, p, of any fisher distribution is given below;

$\alpha_p = \cos^{-1}\left[1 - \frac{N-R}{N}\left[(\frac{1}{p})^{\frac{1}{N-1}} - 1\right]\right]$ for p=0.05 means the circle of 95% confidence

$\alpha_{95} \cong \frac{140}{\sqrt{kN}}$

Finally the standard derivation is

$$S^2 = \frac{1}{N-1}\sum_{i=1}^{N} {\Delta_i}^2$$

where Δ_i is the angle between ith vector and mean direction.

4.1.1.2. Kent Distribution

Kent, is a probability distribution on the two-dimensional unit sphere S2 in R3 (Kent, 1982). It is the analogue on the two-dimensional unit sphere of the bivariate normal distribution with an unconstrained covariance matrix. Kent distribution is 5-parameter probability distribution where the density function is given below.

$$K_{k,\beta,\gamma_1,\gamma_2,\gamma_3} = C(k,\beta)e^{\{kX.\gamma_1+\beta[(X.\gamma_2)^2-(X.\gamma_3)^2]\}}$$

where X is a random 3D unit vector that specifies a point on the 2D sphere.

k is concentration parameter The concentration of the density increases with k.

β determines the ellipticity of the equal probability contour of the distribution ,f β=0, the Kent distribution becomes the von Misses-Fisher distribution on the 2D sphere.

γ1 the mean direction

γ2 the main axis of the elliptical equal probability contours

γ3 the secondary axis of the elliptical equal probability contours

The normalizing factor C(k, β) is approximately given by

$$C(k,\beta) = \frac{\sqrt{(k-2\beta)(k+2\beta)}}{2\pi e^k}$$

The Kent distribution is equivalent to a Gaussian distribution with unrestricted covariance. It is generalization of von Mises-Fisher distribution where it covers non-circular distributions of the data.

To estimate Kent distribution parameters (k, β):

For given sample $(x_1, \dots, x_2)$, let $\bar{x}$ is mean direction and R is resultant vector, as calculated in Fisher statistics, define matrix H using polar coordinates of $\bar{x}$ (θ, ϕ)

$$H = \begin{bmatrix} \cos\theta & -\sin\theta & 0 \\ \sin\theta\cos\phi & \cos\theta\cos\phi & -\sin\phi \\ \sin\theta\sin\phi & \cos\theta\sin\phi & \cos\phi \end{bmatrix}$$

B matrix will be $B = H^T S H$ where S is covariance matrix of given sample, then

$$\bar{\alpha} = \frac{1}{2} tan^{-1}\left(\frac{2b_{23}}{b_{22} - b_{33}}\right) where\ b_{ij}\ is\ i{:}\,row\ and\ j{:}\,column\ element$$

The matrixes K, G, V are computed as follows

$$K = \begin{bmatrix} 1 & 0 & 0 \\ 0 & \cos\bar{\alpha} & -\sin\bar{\alpha} \\ 0 & \sin\bar{\alpha} & \cos\bar{\alpha} \end{bmatrix},$$ G =HK, and $V = G^T S G$,

Finally the estimates are defined as

$$k = (2 - 2\bar{R} - (v_{22} - v_{33})^{-1}) + (2 - 2\bar{R} + (v_{22} - v_{33})^{-1})$$
$$\beta = \frac{(2 - 2\bar{R} - (v_{22} - v_{33})^{-1}) - (2 - 2\bar{R} + (v_{22} - v_{33})^{-1})}{2}$$

where v_{22}, v_{33} are elements of V matrix and v_{ij} denotes ith row and jth column element.

4.1.1.3. Watson Distribution

Watson distribution, also known as Dimroth-Watson's distribution, is one of the axial distributions in Directional Statistics. Watson distribution assumes that diametrically opposite points have the same probability and probability density function of axial distributions possesses antipodal symmetry. f(-l,-m,-n) = g(l,m,n). The probability distribution of random vectors belongs to Watson's family is spherical on sphere.

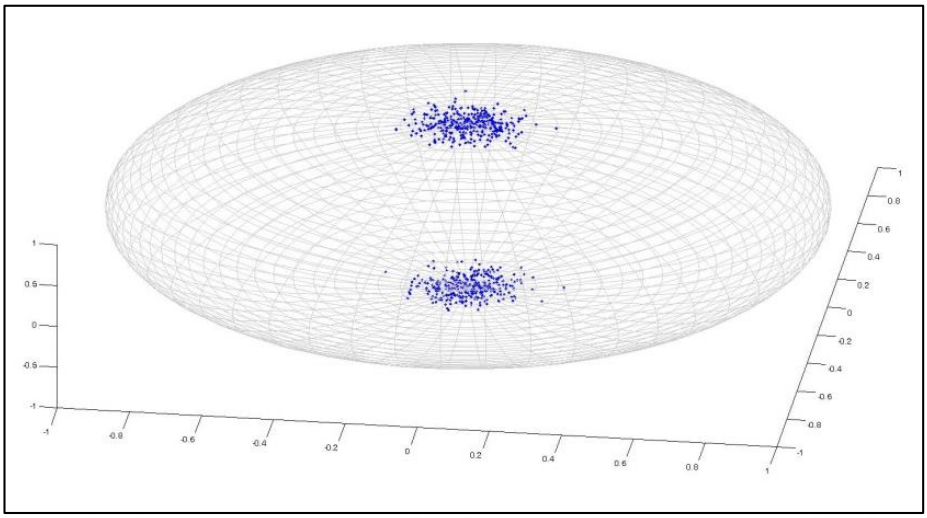

Figure 37: Watson Distribution.

The probability distribution function of Watson distribution can be given as;

$$Watson\ Distibution\ W_p(x;\mu,\kappa) = c_p(\kappa)e^{\kappa(\mu^T x)^2};\ c_p(\kappa) = \frac{\Gamma\left(\frac{p}{2}\right)}{2\pi^{p/2}M\left(\frac{1}{2},\frac{p}{2},\kappa\right)}$$

where x is unit random vector, p is dimension, μ is mean vector, κ is concentration value, M is Kummer's confluent hypergeometic function, Γ: is gamma function and p is dimension of the distribution. To estimate maximum likelihood of this function, we take logarithm, then log-likelihood function is

$$l(\mu,\kappa \pm x_1,\dots,\pm x_n) = \kappa\sum_{i=1}^{n}(x_i^T\mu)^2 - nlog\ M\left(\frac{1}{2},\frac{p}{2},\kappa\right)$$

$$= n\left\{\kappa\mu^T\bar{T}\mu - logM\left(\frac{1}{2},\frac{p}{2},\kappa\right)\right\}$$

where $\bar{T}$ is the scatter matrix of given data. Differentiation with respect to κ gives

$$D_p(\kappa) = \hat{\mu}^T\bar{T}\hat{\mu}; for\ p = 3; = \frac{M(1.5,3.5,\kappa)}{3 * M(0.5,1.5,\kappa)}$$

And to find maximum likelihood estimate of it we need a derivative of $D_p(\kappa)$ for p=3

$$D_3' = \frac{M(2.5,3.5,\kappa)}{5M(0.5,1.5,\kappa)} - \frac{1}{9} * \left(\frac{M(1.5,2.5,\kappa)}{M(0.5,1.5,\kappa)}\right)^2$$

Newton-Rapson method can be used to find maximum values for $D_p(\kappa)$ and used the biggest eigenvalue of scatter matrix, t1, for a bipolar distribution or t3 for a girdle distribution.

4.1.1.4. Bingham Distribution

Bingham distribution is another example of axial distribution where it also possesses antipodal symmetry but as different from Watson distribution, the assumption of spherical dispersion on sphere is loosened, to allow for elliptical dispersion on unit sphere. It is the most general equivalent of the normal distribution for axial data. Bingham Distribution is defined as trivariate normal distribution on a unit sphere. Different than Watson distribution, it has three orthogonal directions as μ_1, μ_2, μ_3 and concentration values (κ_n) for each orientation vector (Kent 1982).

Concentration values define dispersion of the distribution where

1. $\kappa_1 = \kappa_2 = 0$ results in a spherical distribution of axes
2. $\kappa_1 = \kappa_2 \ll 0$ results in a symmetric bipolar distribution
3. $\kappa_1 < \kappa_2 \ll 0$ results in an asymmetric bipolar distribution
4. $\kappa_1 \ll \kappa_2 < 0$ results in an asymmetric griddle distribution
5. $if\ \kappa_1 \ll 0\ and\ \kappa_2 = 0$, then Watson distribution is obtained

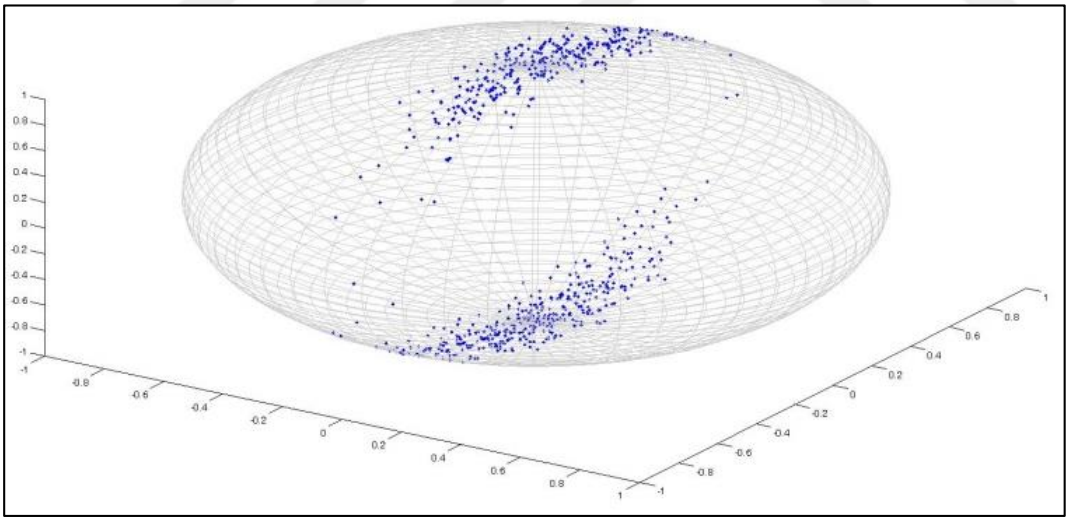

Figure 38: Bingham Distribution.

$$Bingham\ Distibution\ B_p(x;K) = c_p(K)e^{x^T Kx};\ c_p(K) = \frac{\Gamma\left(\frac{p}{2}\right)}{2\pi^{p/2}F\left(\frac{1}{2},\frac{p}{2},K\right)}$$

where x is unit random vector, p is dimension K is 3x3 orthogonal orientation matrix with concentration values, F denoted the confluent Hypergeometric function of matrix argument, Γ: is gamma function and p is dimension of the distribution. For given random sample $\pm x_1, \dots, \pm x_n$, the log-likelihood function can be written as:

$$l(K; \pm x_1, \dots, \pm x_n) = n \left\{ \log tr(A\bar{T}) - logF(\frac{1}{2}, \frac{p}{2}, K) \right\}$$

We can write K and $\bar{T}$ in polar form as $= UKU^T$, $\bar{T} = VtV^T$ with U and V are orthogonal K=diag($\kappa_1, \dots, \kappa_p$) and $t = (\bar{t}_1, \dots, \bar{t}_p)$ where $\kappa_1 \geq \cdots \geq \kappa_p$ and $\bar{t}_1 \geq \cdots \geq \bar{t}_p$. As suggested by Bingham himself, following approximations can be used.

For bipolar case:

$$d = \bar{t}_2 - \bar{t}_3, \qquad s = \bar{t}_1 + \bar{t}_2, \qquad \kappa_0 = -D_3^{-1}(\bar{t}_1)$$
$$\kappa_1 \approx 0, \kappa_2 \approx \kappa_0 + \delta,\ \kappa_3 = \kappa_0 - \delta$$

In the gridle case:

$$d = \bar{t}_1 - \bar{t}_2, \qquad s = \bar{t}_1 + \bar{t}_2, \qquad \kappa_0 = -D_3^{-1}(\bar{t}_3)$$

$$\kappa_1 \approx 0, \kappa_2 = -2\delta, \kappa_3 = \kappa_0 - \delta$$

where $\delta = \frac{2d\kappa_0}{s(\kappa_0 - 1.5) + 1}$

4.1.1.5. Parameter Estimation and Confidence Ellipse

The maximum likelihood estimates of concentration parameters κ_1, κ_2 can be obtained from maximizing the log-likelihood function, where w_n are the eigenvalues of the principle eigenvector of the orientation matrix :

$$F = -Nlog(4\pi) - N\ logd(k_1, k_2) + \ k_1 w_1 k_2 w_2$$

Maximum likelihood estimators of k1,k2 in the Bingham distribution for given eigenvalues ω1,ω2 can be estimated as calculated by Mardia and Zemroch [42].

The confidence ellipse around the mean direction within specified percentage (%) of estimated concentration values of distribution as

$e_{\%}^{mn} = \sqrt{\left[\frac{X_{\%}^2}{2N(\Delta_{mn})}\right]}$ for $\Delta_{mn} = (\kappa_m - \kappa_n)(w_m - w_n)$ and $X_{\%}^2$ is chi-squared value for two degrees of freedom and % is p value for confidence interval.

For p=0.01 and having κ_3=0 [41], ends up with the semi axes of confidence eclipse about the mean direction associated with w_3 as below:

$e_{32} = -1.517 \frac{1}{k_2 N(w_3 - w_{2)}}$ and $e_{31} = -1.517 \frac{1}{k_1 N(w_3 - w_{1)}}$

4.1.2. Directional Statistic Distribution Fitting

Directional statistics can used for many areas in Diffusion Tensor Imaging. The one of the ongoing research areas of DTI is the analysis steps, where there is still lack of solid evaluation method to be used for group-wise analysis. There are vast of work in tractography and connectivity analysis but for group-wise analysis, the researchers still uses scalar metrics and statistics. Directional statistics, on the other hand, uses vectors and inference based on vectors can be possible.

However, in order to use all of the power that directional statistics offers, carefully analysis should be done and different types of directional distribution should be evaluated for different areas of brain across subjects. The research focus of this study is to find which directional statistics distribution describes which area of the brain best.

By considering the assumptions and limitations of directional distributions along with diffusion properties of the brain, following hypothesis are declared and this study is designed to assess these hypothesizes:

Hypothesis I: Due to bi-polarity of principal diffusion directions, Fisher and Kent distributions cannot be applied directly.

Hypothesis II: For WM area that has a low probability of crossing fibers and most of the fibers are concentrated along major fiber directions, Bingham distribution will fit better. Watson distribution will be rejected due to symmetrical constraint around mean direction.

Hypothesis III: For WM area that has high probability of crossing fibers and for GM area, the distribution tends to be symmetrical so Watson distribution will fit better.

In this study, all of distributions given above have been tested against each other and goodness of fit scores has been analyzed for different parts of brain areas with different diffusion properties.

4.1.2.1. Method Pipeline

The current method that has been implemented is a modification and extension of my previous group analysis method. It roots from the same code base that uses some of the Camino libraries (Cook, 2006).

For the analysis of goodness of fit scores for distributions following pipeline has been executed for all of the subjects.

1. *Pre-processing Step:* T1, T2, DWI b0 and DTI images are registered on to each other; grey and white matter masks are constructed and neuroanatomical labeling is performed for on both cortical, subcortical and white matter areas.
2. *PDD Generation:* For the given ROI, primary diffusion directions have been extracted for each voxel using primary eigenvector of the diffusion tensor. This composes the data to fit.
3. *Distribution Fitting:* Four different models have been constructed using Fisher, Kent, Watson and Bingham and distributions are fitted using maximum likelihood methods.
4. *Probability Density Function Evaluation:* For each model, theoretical p.d.f has been computed using estimated parameters.
5. *Goodness of Fit Score (GoF) Evaluation:* Pearson's Chi Square tests have been used for goodness of fit test to test whether observed frequency distribution differs from a theoretical distribution.
6. *Comparison of Distributions:* Chi Square test statistics for each ROI have been compared using ANOVA.

4.1.2.2. Pre-processing Step

Dicom Conversion and correcting the motion and eddy current artifacts are handled in first step. The application of strong field gradients required for diffusion tensor imaging (DTI) result in eddy currents that induce significant direction-dependent distortions in the resulting images. Eddy currents in the gradient coils induce (approximate) stretches and shears in the diffusion weighted images.

Registration: The next step is intra subject registration of T1, T2 and DWI images. In literature, the registration has been done between T2 image and DWI B0 images, and then T1 is registered on T2. So that T1, T2 and DWI images become aligned. For all registration steps FSL's FLIRT and FNIRT routines has been used. All of the images has been registered on DWI B0 image so that we can state that all image operations has been done on diffusion step. This method eliminated the problem of transforming diffusion tensors.

Segmentation & Surface Extraction & Parcellation and Mask Creation: The next step is applying segmentation and parcellation steps of FreeSurfer using recon_all command. These steps transform patient on uniform space and try to segment white and gray matter as well as cortical and subcortical structures. The parcellation step reveals 83 distinct cortical and subcortical structures of the brain and white matter areas.

4.1.2.3. PDD Generation

For each voxel in a given ROI eigen decomposition has been made. A diffusion tensor in a symmetric, square matrix form (3x3) has been acquired from DTI image

that is generated in previous steps. The eigen decomposition has been done as described below:

Calculate D V= λ V where D is diffusion tensor in a symmetric, square matrix form (3x3), V is the the eigenvector, a vector corresponding to an orientation (3x1) and λ is the eigenvalue, a scalar constant. For a 3x3 matrix, there are 3 sets of orthogonal eigenvector and eigenvalue solutions. Using a tridiagonal reduction followed by a QL solution results in the eigenvalues and vectors. The biggest eigen value – vector pair has been chosen as the principal direction of the voxel.

4.1.2.4. Distribution Fitting

For all of the directional distributions under test, Fisher, Kent, Watson and Bingham, maximum likelihood estimation methods have been implemented according to the routines and formulas given in following literatures (Fisher, 1993; Mardia, 2000; Kent, 1982). The necessary computation steps are given in Appendix-A.

Additional routines such as bi-polarity tests, uniformity tests, randomness tests are also implemented. For special mathematical functions such as Bessel function, gamma function, Kummer's confluent hypergeometic function and confluent Hypergeometric function of matrix argument special Java libraries have been found and used. To evaluate Fisher and Kent distribution parameters, we need to correct bi-polarity of the PDD so for such cases the data had separated into two modes and one mode had flipped to antipode.

4.1.2.5. Probability Density Function Evaluation

After estimating the necessary distribution parameters in previous step, the theoretical probability density function has been iteratively evaluated for each distribution. For this issue a synthetic random vector data has been generated. Each vector, totally 700, has different direction and almost uniformly distributed along sphere. So that by using the estimated parameters and probability density functions given in Appendix-A for the distributions, the probabilities can be estimated for each direction. For Watson and Bingham distribution the probabilities are symmetric along the axis of the distributions.

4.1.2.6. Goodness of Fit Score (GoF) Evaluation

In order to apply Pearson's Chi Square tests to test whether observed frequency distribution differs from a theoretical distribution, following steps applied on the original data and synthetic random vector data and respective probability distributions.

- For Fisher and Watson distribution, the sample mean direction, $\bar{R}$, has been evaluated as given in Appendix-A.
- For Kent and Bingham distribution, the axis of moment of Inertia of sample, $\bar{t}$, has been evaluated using scatter matrix of the distribution S. For bi-polar case, it is the biggest eigenvector and for girdle case, it is the smallest eigenvector.
- The transformations $\bar{\theta}, \bar{\phi}$ has been evaluated in order to shift either $\bar{R}$ or $\bar{t}$ to positive z axis.
- The transformation has been applied to original and synthetic data.
- The angle θ has been calculated as the angle between positive x axis and the projected vector on x-y plane. $0 < \theta < 2\pi$
- The observed frequencies and expected frequencies as $\theta_1 < \theta < \theta_2$, where the number frequency bins is 50 and θ_2-$\theta_1 \approx 7.2^o$
- The Pearson's Chi Square is applied.

4.1.3. Tract Profiling and Directional Statistics (TPDS)

In this study, we propose a new tract-based framework using directional information in diffusion tensors to improve statistical group analysis, named as Track Profiling Directional Statistics (TPDS). For this purpose, 1) we have generated a new data structure called tract profile by clustering fibers across subjects, 2) we have developed a method based on directional statistics to compare WM differences of different groups across each tract profile. Overall, this new DTI group analysis method is called tract profiling with directional statistics (TPDS).

4.1.3.1. Pre Processing

We have implemented a fully automated pipeline to perform pre-processing as illustrated in Figure 39.

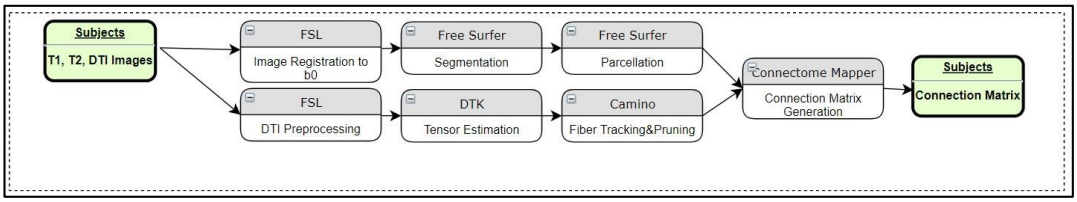

Figure 39: Overall pipeline of pre processing method.

The overall pipeline has been designed using the Connectome Mapper (Daducci et al. 2012). At the individual subject level, pre-processing steps are performed using several software toolkits. The first step is intra subject registration of T1, T2 and DWI images using FSL's FLIRT as described in (Jenkinson and Smith 2001)(Jenkinson et al. 2012). The registration is first done between the T2-weighted

image and DWI B0 images, and then the high resolution T1-weighted image is registered to the T2-weighted image. To eliminate the problem of transforming diffusion tensors, all of the images are registered to the DWI B0 image. This way, all image operations are performed on the diffusion image. For segmentation and parcellation of regions of interest (ROI), FreeSurfer (Fischl et al. 2002) has been used. These steps transform the subject's MRI to uniform space and segment white and gray matter as well as cortical and subcortical structures based on the underlying atlas. The parcellation algorithm (Fischl et al. 2004) reveals 83 distinct cortical and subcortical structures of the brain using Desikan-Killiany Atlas (Desikan et al. 2006).

DTI processing begins with motion and eddy current artifact correction in FSL. Tensor estimation is done by Diffusion Toolkit (DTK) (Wang et al. 2007) and for tractography (Cook et al. 2005)(Parker, Haroon, and Wheeler-Kingshott 2003), streamline fiber-tracking algorithm in Camino has been used.. Each voxel in the parcellated image are selected as seeds. 83 distinct cortical and subcortical areas are masked, and the generated binary image is used as the seed file of the algorithm for particular ROIs. For tracking, Forth-order Runge-Kutta method has been chosen to propagate the tracks using a constant step size. Nearest-neighbor interpolation is applied around local voxel data. A minimum length criterion, 10 mm, is enforced to eliminate premature tract termination due to low SNR and low pathway anisotropy (Behrman-Lay et al. 2015). Each fiber bundle is pruned so that it only contains fibers connecting relevant regions. Number of streamlines depends on size of the ROI. No additional elimination technique has been applied other than minimum length. These steps are illustrated in the second row of Figure 39.

Using the Connectome mapper (Daducci et al. 2012), a connection matrix is generated to calculate the connectivity of the areas via the fiber tracts obtained in the first and second rows of figure 1. After this step, the fiber tracts that connect corresponding brain areas will be bundled to construct relevant fiber bundles. In order to perform group analysis, one last step is necessary: the corresponding bundles of all subjects must be aligned. Therefore, both control and patient images are registered to ICBM DTI 81 Atlas using affine registration. The transformation obtained during this registration is applied to the fiber bundles as seen in the last row of Figure 39.

4.1.3.2. Tract Profiling

Tract profiles are cross sections of the fiber tracts that connect the ROIs specified by the connection matrix generated in pre-processing. For the connections in each ROI pair, a fiber bundle is formed based on the intersections of cross-sectional areas of all subjects' DWI. Then the medial line of the fiber bundle is computed. Finally, a cross sectional profile is generated along the medial line so that the distribution of PDDs along each cross section is aggregated separately for each subject group.

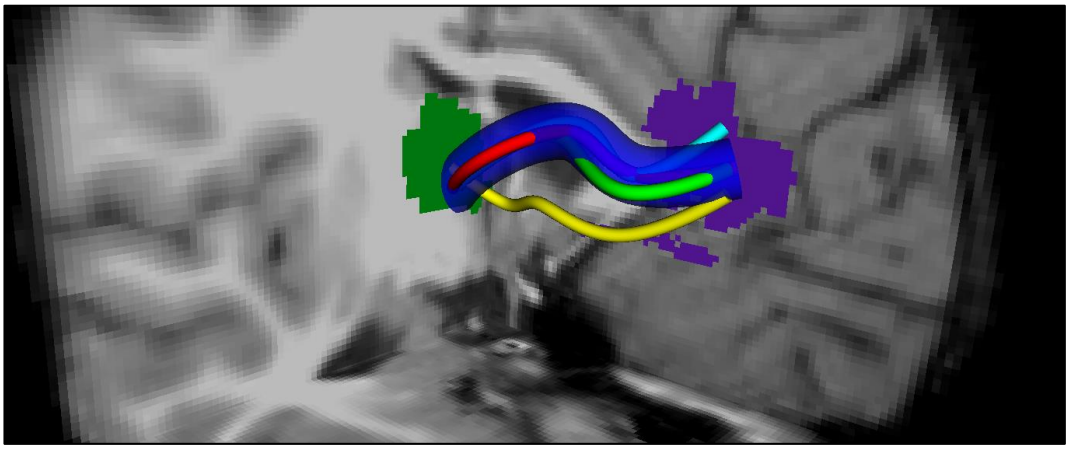

Figure 40: Cross sectional Tract bundle (b-spline representation) that covers all tracts connecting two regions. The outlier voxels (on the Tracts) are omitted.

4.1.3.2.1. Overlapping Fiber Calculation

Overlapping fibers/voxels are calculated across all of the subjects. This is done for each fiber bundle by calculating its maximum overlap. During this process, some specific bundles might be left out as outliers. In Figure 40, the overlapping fiber bundle is shown between the two ROIs Thalamus (green) and Rostral Anterior Cingulate (purple). The bundles shown with the yellow, cyan, green and red colors are marked as outliers and left out of the overlapping area.

Let p be a point in the 3D image, Z^3 where each voxel is represented as *p*. The adjacency can be defined as

$N_j(p)$ for j=6,18,26 the set of point j-adjacent to the point *p*.

The sequence of points (x_0, x_1, …, x_n) is a j-path of length $n \geq 0$ from the point x_0 to point x_n in a non-empty set of points X if each point of the sequence is in X and x_i is j-adjacent to x_{i-1} for each $1 \leq i \leq n$. The connectivity can be defined as j-connected if there is a j-path in X between them.

The voxel image can be represented as *3D binary (m,n) image* $\mathcal{P}$ where $\mathcal{P} = (Z^3, m, n, B)$ (Kong and Rosenfeld 1989). Each element in Z^3 is called a point of $\mathcal{P}$ and each point in $B \subseteq Z^3$ is called a black point and assigned 1, Each point in $Z^3 \setminus B$ is called a white point and assigned 0. *m* holds black points and *n* holds white points.

In order to be used in multi-subject analysis adaptation of the definition is needed. For a given ROI pairs *(i,j)*, Let $\mathcal{P}_0, \mathcal{P}_1, \ldots, \mathcal{P}_k$ *a set in S* where S is super set of all subjects in group analysis where k is number of subjects. *Tn(i,j)* can be defined as a set of points in $\mathcal{P}_n$ where it belongs a tract connecting ROI i and j. So definition of black point can be also be extended as follows, a point in $\mathcal{P}$ is assigned as black

point if and only if it is also black point for all sets in $\mathcal{P}_0, \mathcal{P}_1, \ldots, \mathcal{P}_k \in S$ *for a given ROI i and j;*

A black point is called *border point* if it is 6-adjacent to at least one white point. A black point is called *end-point* if it has exactly one black 26-neighbor. Black point p is simple in $(Z^3, 26, 6, B)$ if and only if all the following conditions hold (Palágyi et al. 2001):

1. The set $N_{26}(p) \cap (B \setminus \{p\})$ is not empty. (p is not isolated point)
2. The set $N_{26}(p) \cap (B \setminus \{p\})$ is 26 -connected
3. The set $(Z^3 \setminus B) \cap N_6(p)$ is not empty. (p is a border point)
4. The set $(Z^3 \setminus B) \cap N_6(p)$ is 6 -connected in the set $(Z^3 \setminus B) \cap N_{18}(p)$

4.1.3.2.2. Medial Line Generation

The skeleton of the overlapping bundles is calculated. The curve skeleton is a 1D set which runs through the center of the overlapping bundles in such a way that it preserves the topological properties of the overlapping area. Connectivity conditions are defined as follows. The sequence of points (x0, x1, …, xn) is a j-path of length $n \geq 0$ from the point x0 to point xn in a non-empty set of points X if each point of the sequence is in X and xi is j-adjacent to xi-1 for each $1 \leq i \leq n$. The adjacency can be defined as Nj(p) the set of points j-adjacent , to the point p, where j = 6, 18, 26. Connectivity can be defined as j-connected if there is a j-path between them in X.

In order to construct the aforementioned skeleton, first of all curve thinning (Blum H. 1967) (Kong and Rosenfeld 1989) is used on Ꝑ. The medial line of the fiber bundles was generated as depicted in (Palágyi et al. 2001). As such, in each iteration, border points of Ꝑ were deleted until no more deletion was possible. The algorithm is implemented as sequential iterations where each step checks for six sub routines for each of 6-directions that are immediate neighbors of a black point in Ꝑ. In each iteration border points are deleted upon satisfying a condition called simple point condition . In this way, the object is shrunk uniformly in each direction. The operation will continue until no more shrinking is possible for each direction. By adding connectivity conditions, the skeleton ends up with medial line in the near center of the object. In Figure 41 the example medial line for the fiber bundle is shown with dark blue.

```
procedure THINNING (X,Y)
Y = X
repeat
        modified = 0
        modified = modified + ITERATE(Y, Point3d(0,0,1));
        modified = modified + ITERATE(Y, Point3d(0,0,-1));
        modified = modified + ITERATE(Y,Point3d(0,1,0));
        modified = modified + ITERATE(Y,Point3d(0,-1,0));
```

```
        modified = modified + ITERATE(Y,Point3d(1,0,0));
        modified = modified + ITERATE(Y,Point3d(-1,0,0));
until modified > 0;
function ITERATE (Y, Point3d direction)
        modified = 0
        for each point p in Y do
                if (p+direction) is Border Point then
                        Np= GET_26_NEIGHBORS (Y, p);
                        If not Np is endpoint and Np is simple
                                Insert p in List:L
        while List:L is EMPTY do
                p = GET_FROM_LIST
                Np= GET_26_NEIGHBORS (Y, p);
                If not Np is endpoint and Np is simple
                        Set_Zero (Y,p);
                        modified++;

return modified
```

The algorithm is implemented as sequential iterations where each step checks for six sub routines for each 6-directions. In each iterations border points are deleted if it satisfies simple point condition. In this way, the object is shrunk uniformly in each direction. The operation will continue till no more shrinking is possible for each direction. By adding connectivity conditions, the skeleton ends up with medial line in the near center of the object.

Finally the resulting medial line is smoothed by generating a b-spline representation as follows. In order to generate b-spline representation of the medial line, the voxel coordinates on the medial line are represented as data points $\{P_k\}, k \in MedialLine$. A B-spline curve that fits the data is parameterized by $t \in [0,1]$, where $X(t) = \sum_{i=0}^{n} N_{i,d}(t)Q_i$, the control points Q_i are unknown quantities that has been evaluated using least-squares fitting method described below:

For *n* control points $\hat{Q} = \begin{bmatrix} Q_0 \\ Q_1 \\ \vdots \\ Q_n \end{bmatrix}$, and m sample points $\hat{P} = \begin{bmatrix} P_0 \\ P_1 \\ \vdots \\ P_m \end{bmatrix}$, the least square error function between B-Spline curve and sample points is the scalar valued function:

$$E(\widehat{Q}) = \frac{1}{2}\sum_{k=0}^{m}\left|\sum_{j=0}^{n} N_{j,d}(t_k)Q_j - P_k\right|^2$$

To minimize the error function, E, where it is quadratic in the components of $\hat{Q}$, it is a graph a paraboloid, so it has global minimum that can be found when all its first order derivates are 0. The first order partial derivatives can be written as control points, Q_i

$$\frac{\partial E}{\partial Q_i} = \sum_{k=0}^{m} \left(\sum_{j=0}^{n} N_{j,d}(t_k) Q_j - P_k \right) N_{j,d}(t_k)$$

$$\frac{\partial E}{\partial Q_i} = \sum_{k=0}^{m} \sum_{j=0}^{n} N_{i,d}(t_k) N_{j,d}(t_k) Q_j - \sum_{k=0}^{m} N_{i,d}(t_k)\, P_k$$

It can be written as $\sum_{k=0}^{m} \sum_{j=0}^{n} a_{k,i} a_{k,j} Q_j - \sum_{k=0}^{m} a_{k,i}\, P_k$ where $a_{k,i} = N_{k,d}(t_k)$ for $0 \leq i \leq n$, by setting the partial derivatives to zero vector, it leads to the system of equations:

$$0 = \sum_{k=0}^{m} \sum_{j=0}^{n} a_{k,i} a_{k,j} Q_j - \sum_{k=0}^{m} a_{k,i}\, P_k = A^T A \hat{Q} - A^T \hat{P}$$

Where $A = [a_{rc}]$ is a matrix with m+1 rows and n+1 columns.

$$\hat{Q} = (A^T A)^{-1} A^T \hat{P} = [(A^T A)^{-1} A^T] \hat{P} = X \hat{P}$$

Since A is tridiagonal where it has contiguous set of upper bands and lower bands, the equation can be solved with Cholesky decomposition and the vector of control points $\hat{Q}$ can be found.

The spline is then sliced with 2-mm regular intervals so that planes that are perpendicular to the spline are obtained (Figure 41). Since derivative of spline is 1 less order of yet another b-spline where new control points as

$Q_i = \frac{p}{u_{i+1+1} - u_{i+1}} (P_{i+1} - P_i)$ from the surface tangent, normal vector has been computed and cross-sectional areas has been extracted.

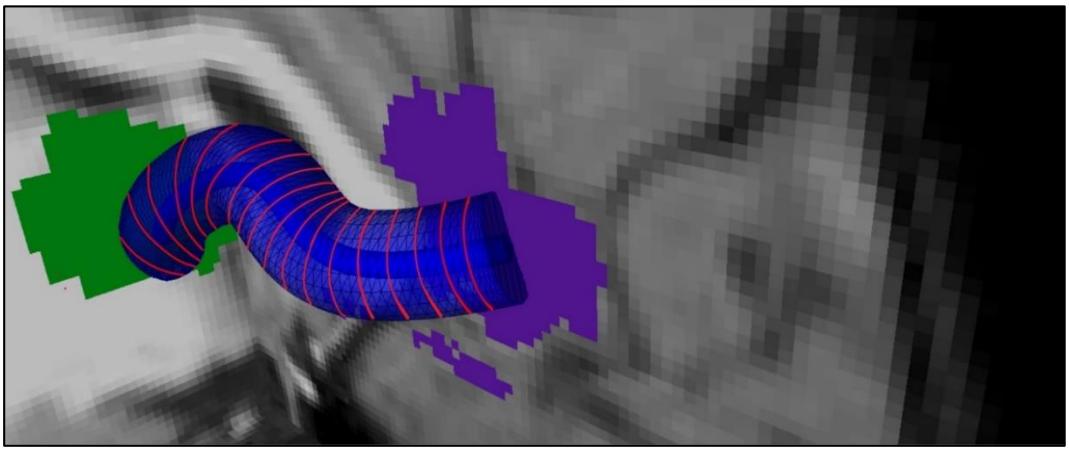

Figure 41: Medial line of cross sectional area between 2 ROIs (green and purple) after pruning and b-spline curve fitting.

4.1.3.2.3. Calculations of Tract Cross Sections

The skeleton is sliced with 2-mm regular intervals so that cross sectional areas that are perpendicular to the b-spline are obtained using normal vectors computed from the surface tangents in Figure 41 For each voxel in Ꝑ that intersects with these cross-sectional areas, PDDs that represent individual subjects are added as tract profiles representing that slice. Hence for a tract with J slices, there are J tract profiles that contain PDDs which are representative of the subject group. An example tract profile (i.e. slice) from a single subject is shown in Figure 42. The PDDs from the subjects for a specific group are aggregated as follows. At each slice, there are fixed number of voxels, and at each voxel, there can be multiple PDDs, each coming from a different subject, depending on whether the subject's tract goes through that voxel or not.

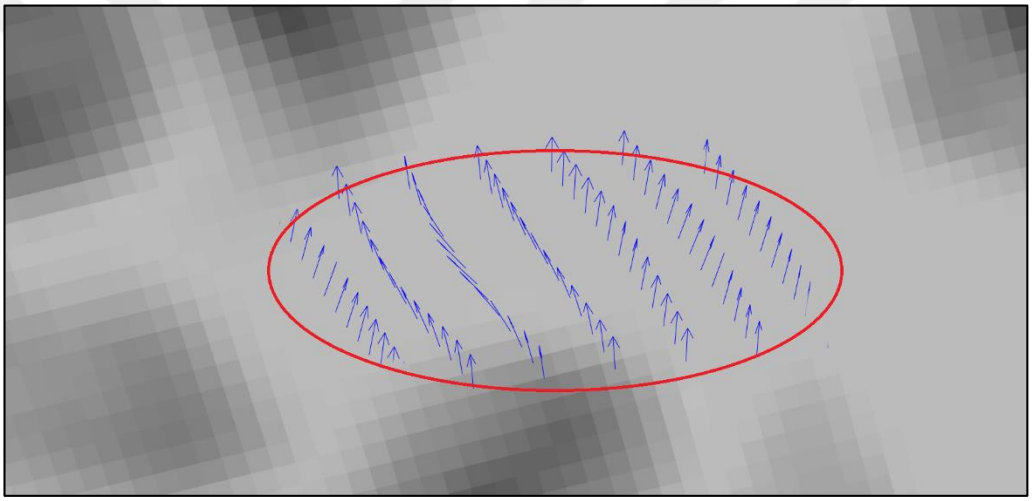

Figure 42: Principal diffusion directions in a cross-sectional profile area from only one subject.

4.1.3.3. Directional Statistics (DS)

Executing statistical analysis exclusively on areas that are defined by tract profiles eliminates voxel-wise comparison. Hence, misalignment problems no longer exist. Hypothesis testing is conducted only at cross-sectional tract profiles that are separated by 2-mm regular intervals. For the set of PDDs embodied in each tract profile j, a parametric directional statistic distribution is fitted. Through such parametrization, the PDDs of all subjects that fit into the tract profile j are projected onto a sphere as shown in Figure 43.

Watson distribution is bi-modal and symmetrical around mean direction. Watson distribution assumes that diametrically opposite points have the same probability. Also the probability density function of axial distributions possesses antipodal symmetry (i.e. f(-l,-m,-n) = g(l,m,n)). The probability distribution of random

vectors that belong to the Watson's family is spherical on sphere. On the other hand, Bingham distribution is bi-modal and elliptical (Cheng et al. 2014; Fisher, Lewis, and Embleton 1993). Bingham distribution is free from symmetrical constrains, hence it provides more advanced distribution fitting options in comparison to the Watson distribution.

After parametric representation through either Watson or Bingham distribution, two group of subjects can be compared by using an eclipse of confidence defined by the p-value. For fitting a single group's data, the mean direction vector of the group is computed. If it lies inside the eclipse of confidence of the targeted distribution, then the null hypothesis is likely, justifying a reasonable fit to the associated directional distribution. On the other hand, if the confidence ellipse around the mean direction does not overlap for a given confidence level then the null hypothesis is unlikely, rejecting the fit. For two groups, the case with different means is indicated by separated cones of confidence, which in turn indicates significant differences. On the other hand, overlapping cones of confidence indicate insignificant differences, hence acceptance of null hypothesis. An example distribution is provided in Figure 34, for 2 group of subjects, for a representation with Bingham distribution.

Details of the Watson, Bingham distributions and eclipse of confidence is given in sections 4.1.1.3. Watson Distribution , 4.1.1.4. Bingham Distribution, 4.1.1.5. Parameter Estimation and Confidence Ellipse.

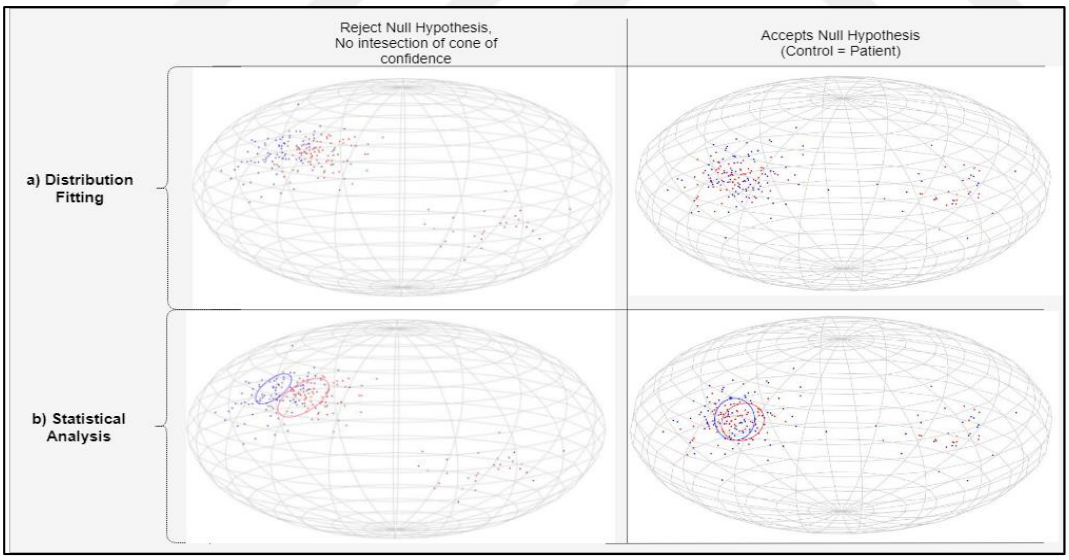

Figure 43: Parameter Estimation and Confidence Ellipses a: Shows vector projections of PDDs on unit sphere for control (blue) and for patient (red); b: First coloum : Shows an example of statistical signifacent difference between populations cone of confidence are not intersects, c: Second coloum: Shows an example for accepting null hypothesis.

4.2. Experiments and Results

4.2.1. Subjects

The control group contained of 14 healthy subjects (8 female and 6 male) with age: 31.71 ±7.62, who had no neurological disease and were not taking any medication. The depression group was consisting of 16 subjects (8 female and 8 male, age: 31.12± 8.95) . The data is collected as part of a local institutional project funded by METU (BAP-07-04-2012). Project management and subject recruitment was handled by a larger project for which results will be published elsewhere.

4.2.2. Data Acquisition

We collected whole brain MRI scans using Siemens MAGNETOM 3 Tesla scanner situated at the Bilkent University UMRAM center. T1-weighted (TR:2500 ms, TE:3 ms, TI: 1000 ms, FA:8°, sagittal plane 1 mm isotropic resolution) T2-weighted (TR:5900 ms, TE:108 ms, FA:120o, Spacing: 2.2) and DTI scans (TR: 8270 ms, TE: 83 ms, FA:90°, Spacing: 2.2, 7 images with b-factor = 0 s/mm2, 45 directions b-factor = 700 s/mm2) are collected from the participants in a single session.

4.2.3. Directional Statistic Distribution Fitting

Initially the hypothesis given in section 3.2 is verified as follows. A set of ROI's given below are selected according to hypothesis criteria.

- ROI I: highly concentrated one-directional WM area (Mid-Posterior Corpus Callosum (FreeSurfer Area: 252)) ,
- ROI II: concentrated and low probability of crossing fibers WM area (White Matter of Left Temporal Pole (FreeSurfer Area: 3033)),
- ROI III: high probability of crossing fibers WM area (White Matter of Left Temporal Pole (FreeSurfer Area: 3033))
- ROI IV: Gray Matter (Right-Thalamus (FreeSurfer Area: 48)) area.

Using only 10 healthy subjects the pipeline has been applied and following test have been done.

To verify hypothesis I, all ROI's are analyzed against bi-polarity. Due to estimation of diffusion tensors and corresponding eigenvector, bi-polarity cannot be escaped as can be seen in Figure 44. The principle diffusion directions are always bi-polar and have nearly equal probability for opposite axis. By default this kind of data cannot be applied to either Fisher or Kent distributions. Hence the data had separated into two modes and one mode had flipped to antipode so that bi-polarity is resolved. However in this case, the uniformity of data along mean direction cannot be

satisfied. This is also one of the assumptions of the distributions. As a result we have enough evidence to reject both distributions and do not test are rejected.

To verify hypothesis II and III, the pipeline described in method section has been finalized for all of the 10 subjects and each ROI. First of all, we must verify that the ROI are selected as intended. As can be seen in Figure 44 (a-b), PDD's of Right Thalamus are almost uniformly distributed on unit sphere. The directions are bi-polar and there is a uniform distribution of declinations. This is grey matter area and as declared in hypothesis III, for this area Watson's distribution is expected to be best fit. Figure 44 (c-d) shows PDD's of Mid Posterior Corpus. As can be seen PDD's are bi-polar and concentrated along fiber tract directions. The distribution is dispersed elliptically. As declared in hypothesis II, for this area Bingham's distribution is expected to be best fit. Figure 44 (e-f) shows PDD's of White Matter of Right Transverse Temporal Gyrus. As can be seen PDD's are bi-polar and concentrated along fiber tract directions. The distribution is dispersed elliptically. As declared in hypothesis II, for this area Bingham's distribution is expected to be best fit. Figure 44 (g-h) shows PDD's of White Matter of Left Temporal Pole. As can be seen PDD's are almost uniformly distributed on unit sphere. The directions are bi-polar and the distribution is dispersed symmetrically around mean direction. This kind of distribution is best fitted with Watson's distribution as declared in hypothesis III.

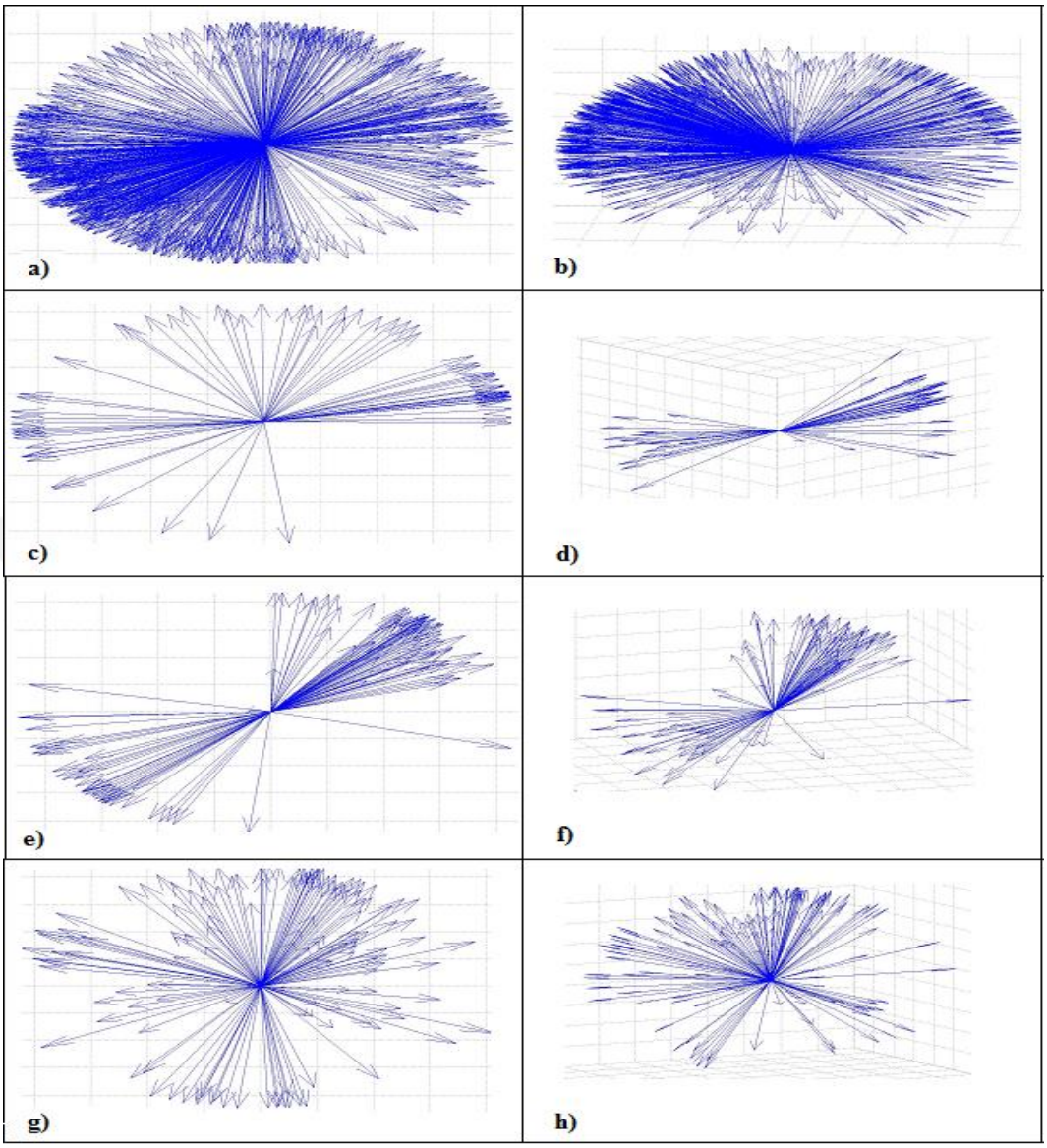

Figure 44: PDD for ROI's (a-b) right thalamus, (c-d) Mid posterior corpus callosum, (e-f) white matter of right transverse temporal gyrus, (g-h) white matter of left temporal pole. (a-c-e-g) shows PDD's projected on x-y plane and (b-d-f-h) is 3D-view.

The dispersion of PDD's are better shown in Figure 45 and Figure 46. Figure 45 shows the ROI's and fiber tracts after deterministic tractography has been finalized (Parker, 2003). Figure 45 a: shows the fiber tracts that start in White Matter of Right Transverse Temporal Gyrus. As can be seen, the tracts are almost uniform and there are mainly two fiber tract directions. Figure 45 b: shows the fiber tracts that start in White Matter of Left Temporal Pole. As can be seen, there is a diversity in the fiber directions, as a result of crossing fibers. Figure 46 emphases this issue, It represents the PDDs' in 2D view for White Matter of Right Transverse Temporal Gyrus (c)

and White Matter of Left Temporal Pole (d). In Figure 46 c, the PDDs' are uniform and in Figure 46 d, the PDDs' are varied along many directions.

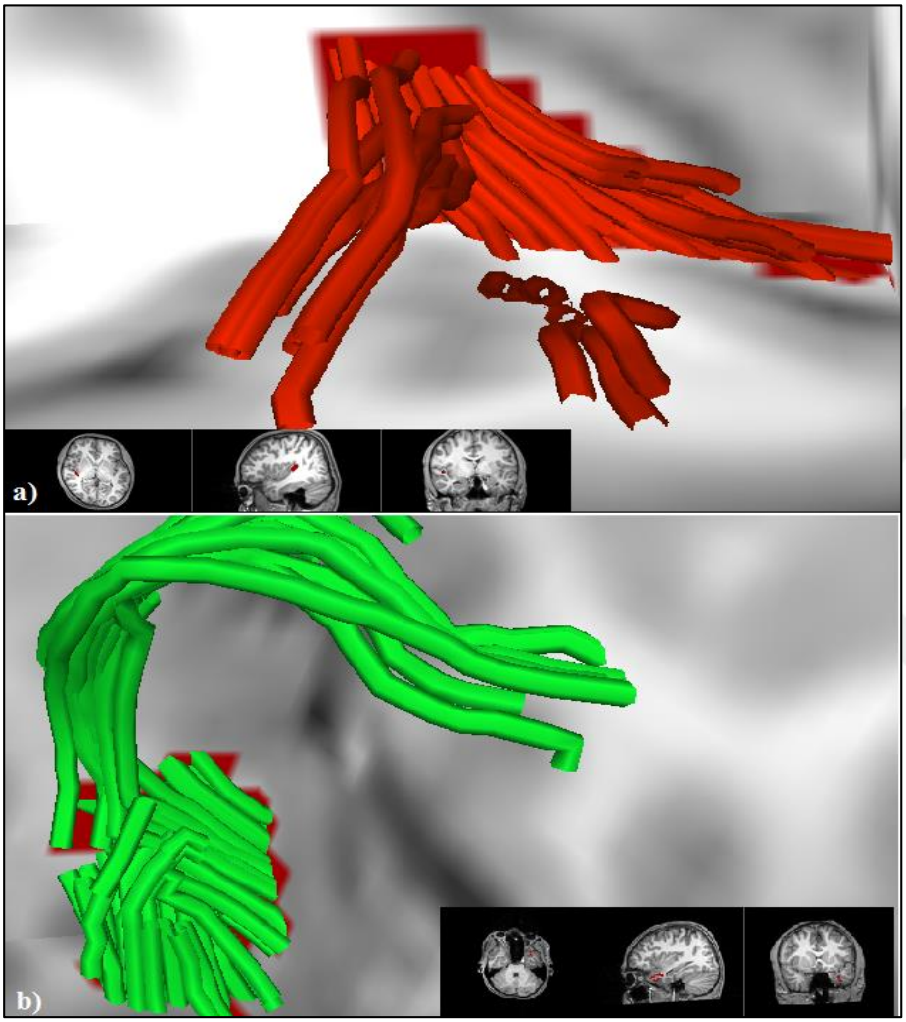

Figure 45: Visualization of Fiber Tracts a: Fiber tracts of white matter of right transverse temporal gyrus, b: Fiber tracts of white matter of left temporal pole.

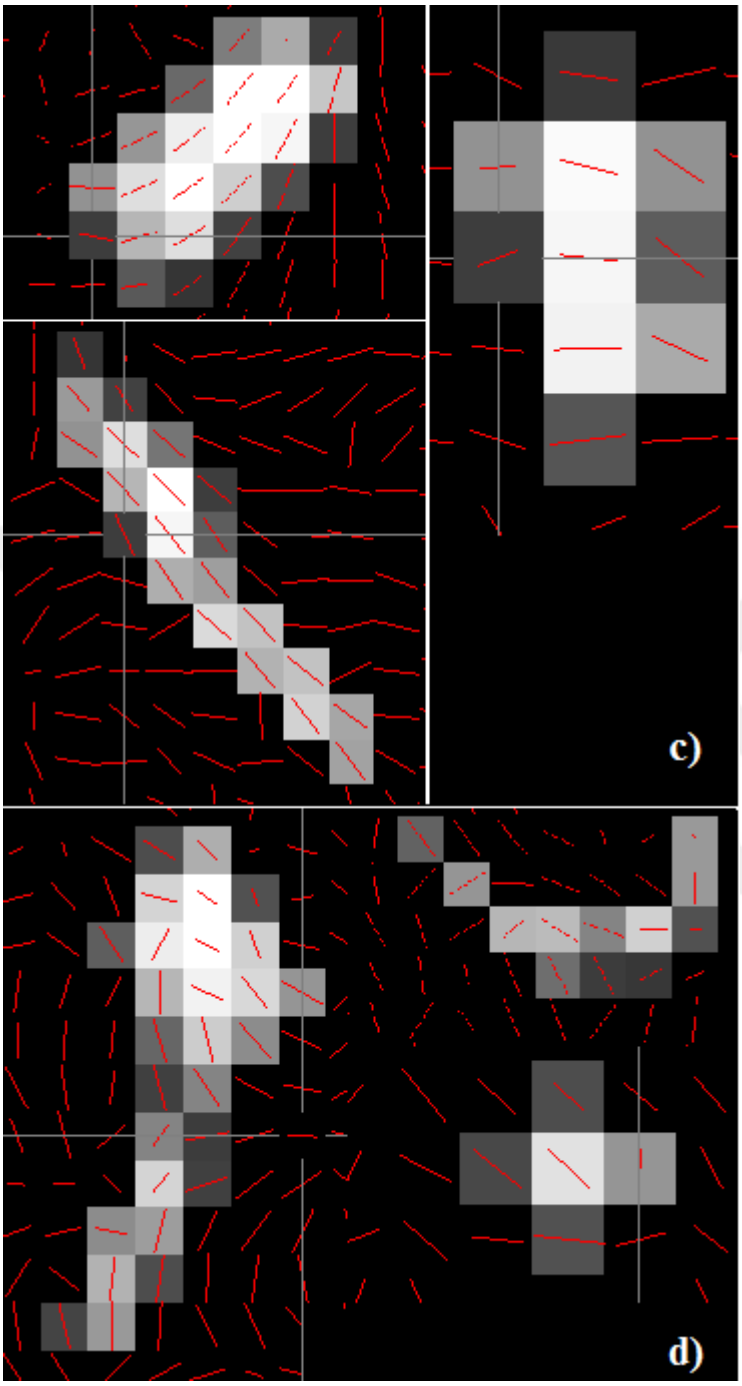

Figure 46: PDDs' in 2D view c: PDD of white matter of right transverse temporal gyrus, d: White matter of left temporal pole.

The ANOVA results for GoF score comparison is shown in Table 1. For ROI I: highly concentrated one-directional WM area (Mid-Posterior Corpus Callosum), Bingham distribution fits better with Bingham (F stat: 17.29, p: 0.0001) k1=-55.02 and k2=-27.28 distribution parameters. The high number of parameters also shows high concentration.

For ROI II: concentrated and low probability of crossing fibers WM area (White Matter of Left Temporal Pole), Bingham distribution fits better with Bingham (F stat: 2.82, p: 0.1) k1=-7.28 and k2=-4.43 distribution parameters. Both results verify hypothesis II: *For WM area that has a low probability of crossing fibers and most of the fibers are concentrated along major fiber directions, Bingham distribution will fit better. Watson distribution will be rejected due to symmetrical constraint around mean direction.*

For ROI III: high probability of crossing fibers WM area (White Matter of Left Temporal Pole) and ROI IV: Gray Matter (Right-Thalamus) area Watson distribution fits better with Watson distribution (F stat: 7, p: 0.012 and F stat: 5.27, p: 0.02 respectively) with kappa:3.53 and 2.05. Both results verify hypothesis III: *For WM area that has high probability of crossing fibers and for GM area, the distribution tends to be symmetrical so Watson distribution will fit better.*

Table 2: GoF scores and ANOVA test results for ROI's (Assuming that chi square test statistics are normal distributed and variances are equal).

ROI Name	Avg. # Voxels in ROI	Tested Hypothesis	Exp. Best Fit	Observed Best Fit
ROI I:	76	Hypothesis II (F stat: 17.29, p: 0.0001)	Bingham	**Bingham distribution (k1=-55.02, k2=-27.38)** Bingham: GoF $\chi 2$: 40.09|38.15|64.19|34.36|39.33|69.10|25.80|32.18|52.21|14.07 Watson: GoF $\chi 2$: 104.4|127.4|107.0|111.1|120.8|209.6|104.5|205.1|98.12|109.1
ROI II:	122	Hypothesis II (F stat: 2.82, p: 0.1)	Bingham	**Bingham distribution (k1=-7.28, k2=-4.43)** Bingham: GoF $\chi 2$: 31.06|97.11|53.12|47.20|55.75|51.06|12.34|35.46|48.20|28.17 Watson: GoF $\chi 2$: 94.60|154.5|138.3|94.44|48.92|52.25|56.23|48.12|79.02|45.01
ROI III:	148	Hypothesis III (F stat: 7, p: 0.012)	Watson	**Watson distribution (kappa=3.53)** Bingham: GoF $\chi 2$: 31.39|61.97|80.91|38.68|63.08|97.95|68.12|76.19|58.26|45.09 Watson: GoF $\chi 2$: 27.75|56.84|26.76|34.02|38.15|31.84|37.12|43.82|39.20|28.15
ROI IV:	1160	Hypothesis III (F stat: 5.27, p: 0.02)	Watson	**Watson distribution (kappa=2.05)** Bingham: GoF $\chi 2$: 111.9|65.46|48.16|56.39|74.86|57.00|67.71|62.34|52.70|48.61 Watson: GoF $\chi 2$: 34.68|48.10|34.42|49.27|56.09|35.99|31.83|39.07|50.47|34.65

4.2.4. Pipeline

In summary the new preprocessing pipeline is given below.

Preprocessing: Nearly 10 min. for each subject

- DICOM – NIFTI Conversion
- BET: Brain extraction for T1, T2, DWI images
- Eddy-Current and Motion Reduction using Diffusion Toolkit

Transformation: Nearly 30 min. for each subject

- T1->T2 and T2->DWI Registration using FSL FLIRT and FNIRT
- Combining T1->T2 and T2->DWI to get T1->DWI

Segmentation and Parcellation: Nearly 12 h for each subject

- T1 image has been segmented and parcellated.

Registration: Nearly 10 min for each subject

- Segmented and parcellated T1 images are transformed into Diffusion space using T1->DWI transformation matrix.

Tensor Estimation: Nearly 10 min for each subject

- Using Diffusion Toolkit, tensors are estimated and DTI image has been generated.

<u>Area (ROI) Selection</u>

- Using John Hopkins Medical School DTI white matter and tract atlas, totally 48 areas has been chosen as ROI.

Atlas Transformation: Nearly 15 min. for each subject

- T2 image has been registered on Atlas template T2 image using FSL FLIRT and FNIRT. The transformation matrix have been stored.
- By reverting T2->Atlas transformation matrix, Atlas->T2 transformation matrix has been generated. By combining with T2->DWI matrix, Atlas->T2->DWI matrix has been generated.

Atlas Registration: Nearly 5 min. for each subject

- Atlas Label maps has been transformed to Diffusion space using Atlas->t2->DWI matrix.

Below the preprocessing steps has been visually described.

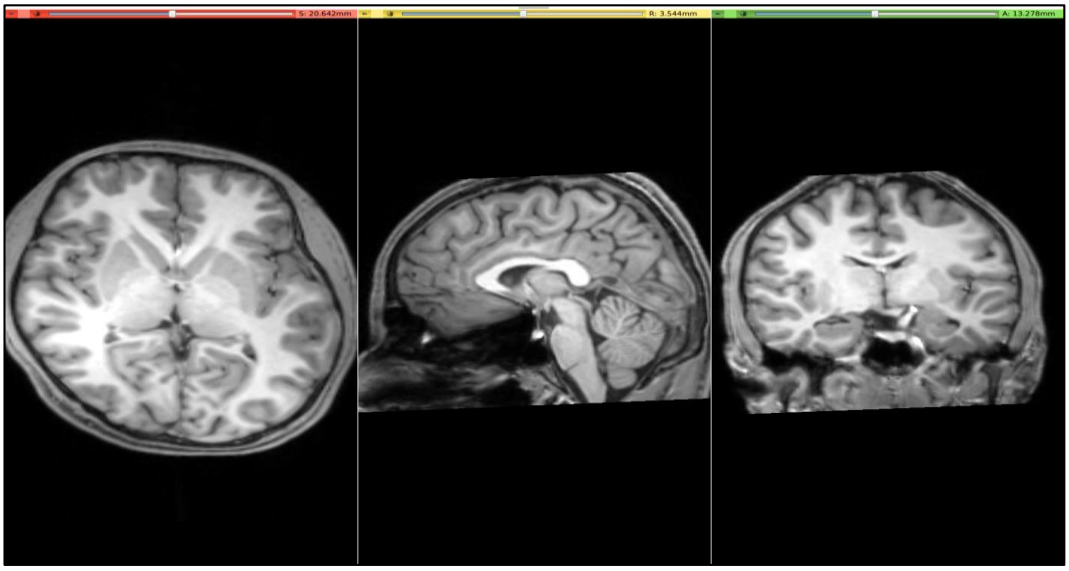

Figure 47: T1 image registration on DWI b0.

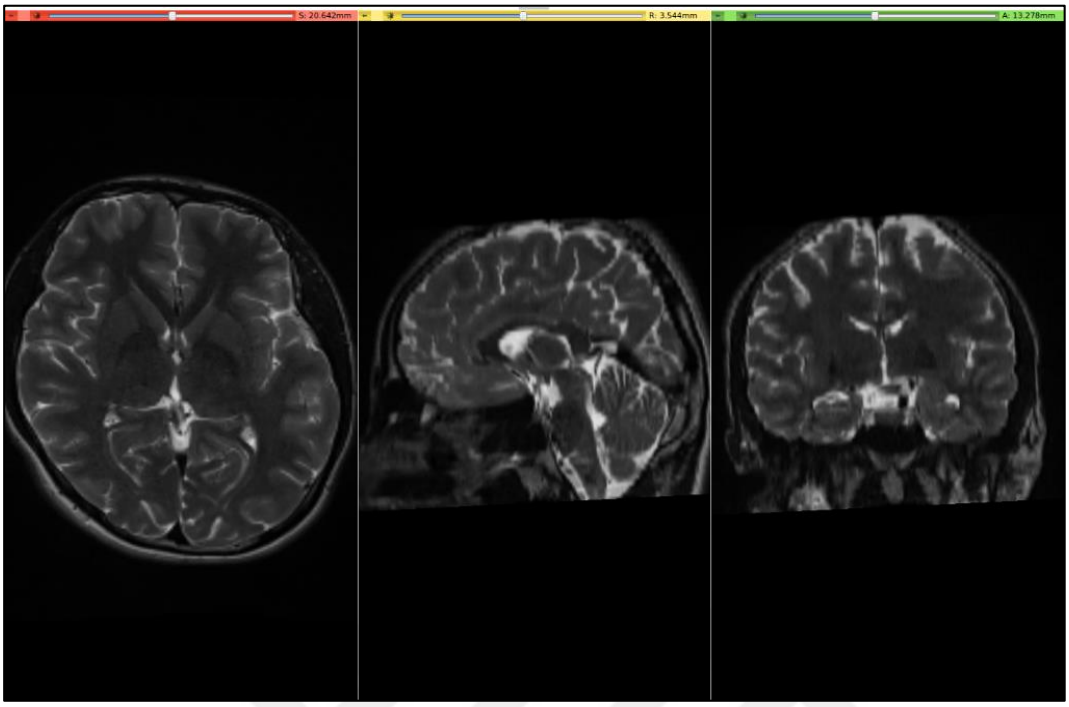

Figure 48: T2 image registration on DWI b0.

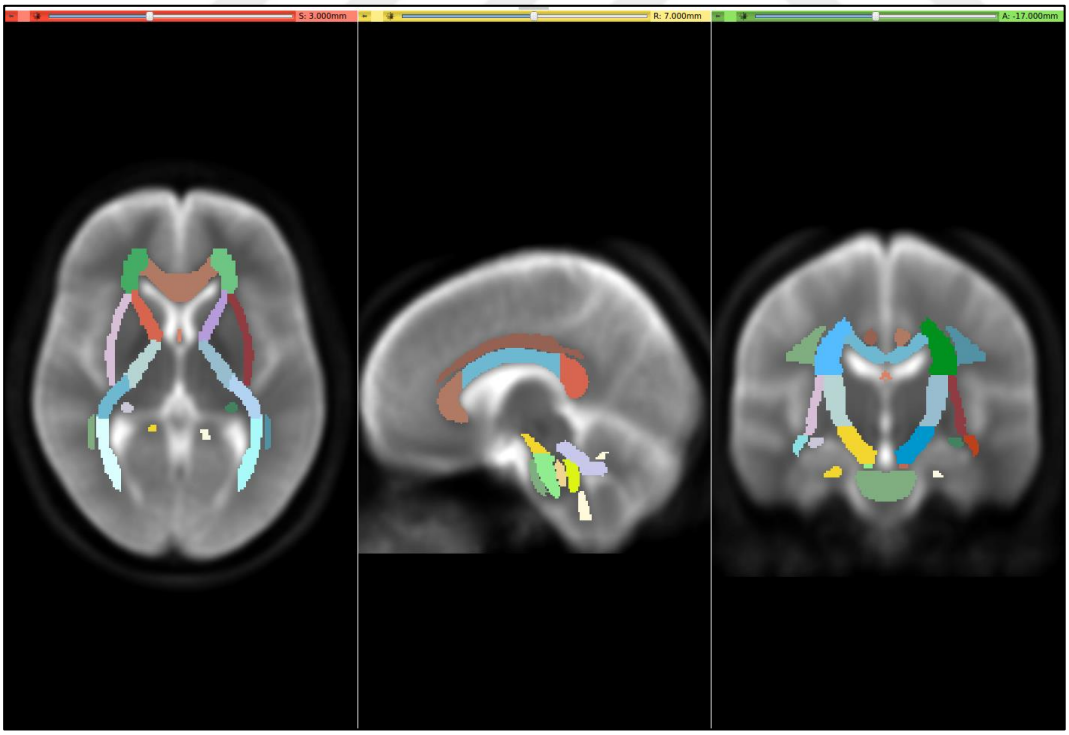

Figure 49: JHU white matter atlas.

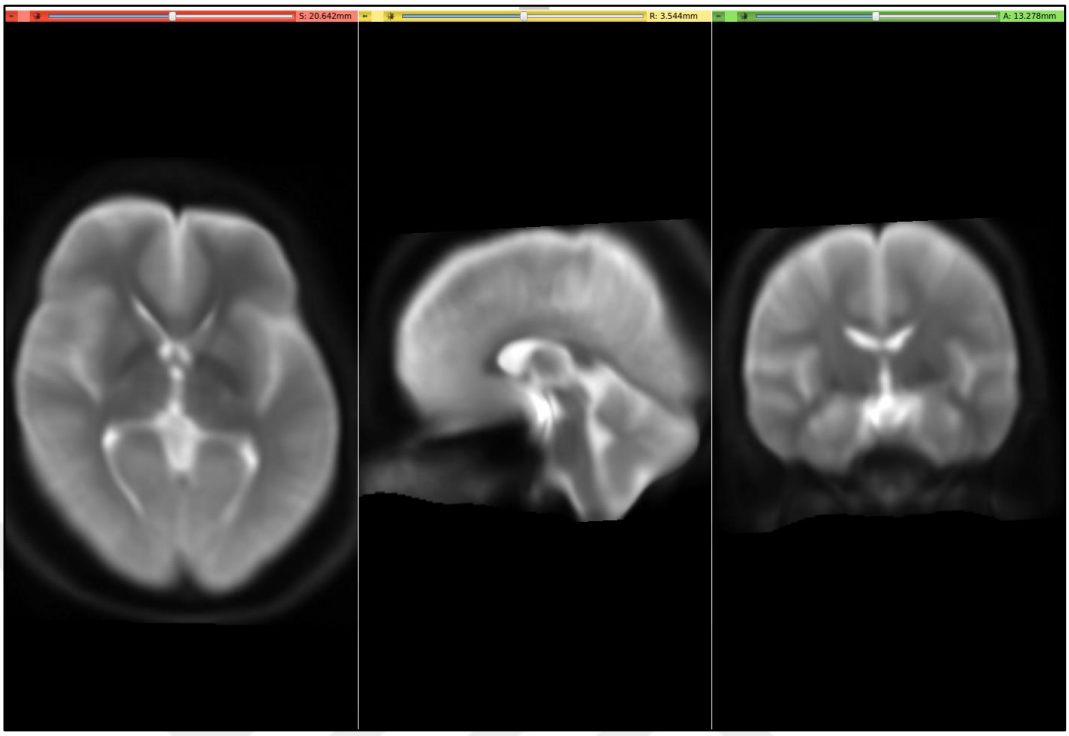

Figure 50: JHU white matter atlas registered on subject's DWI bo image.

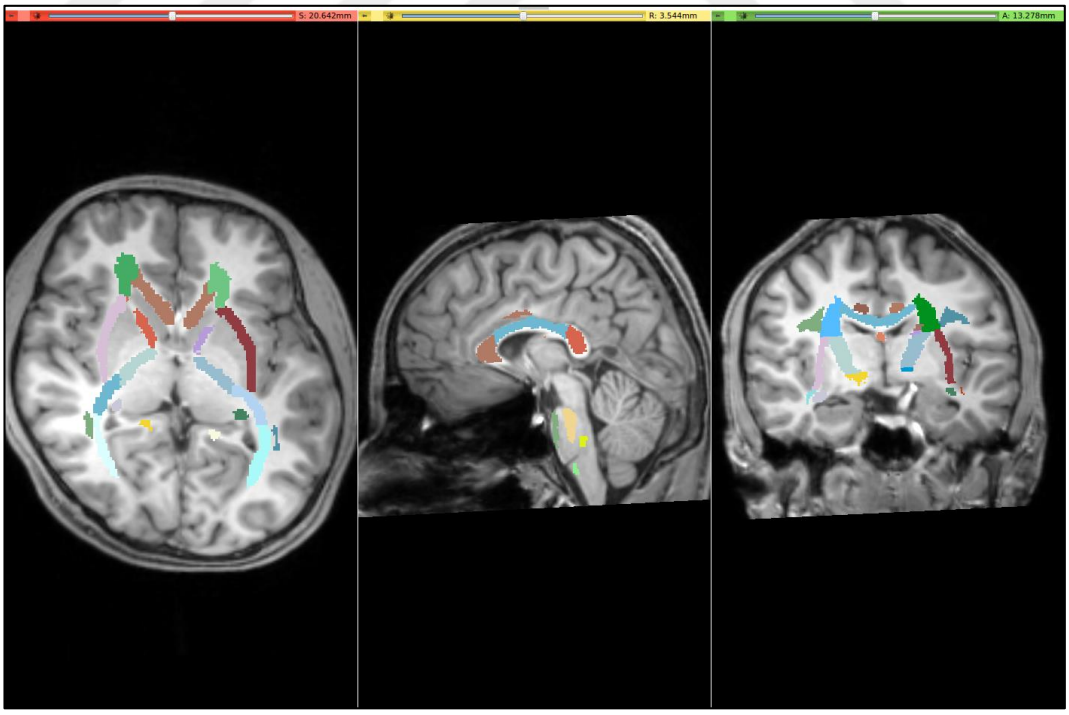

Figure 51: The white matter areas registered on T1 image.

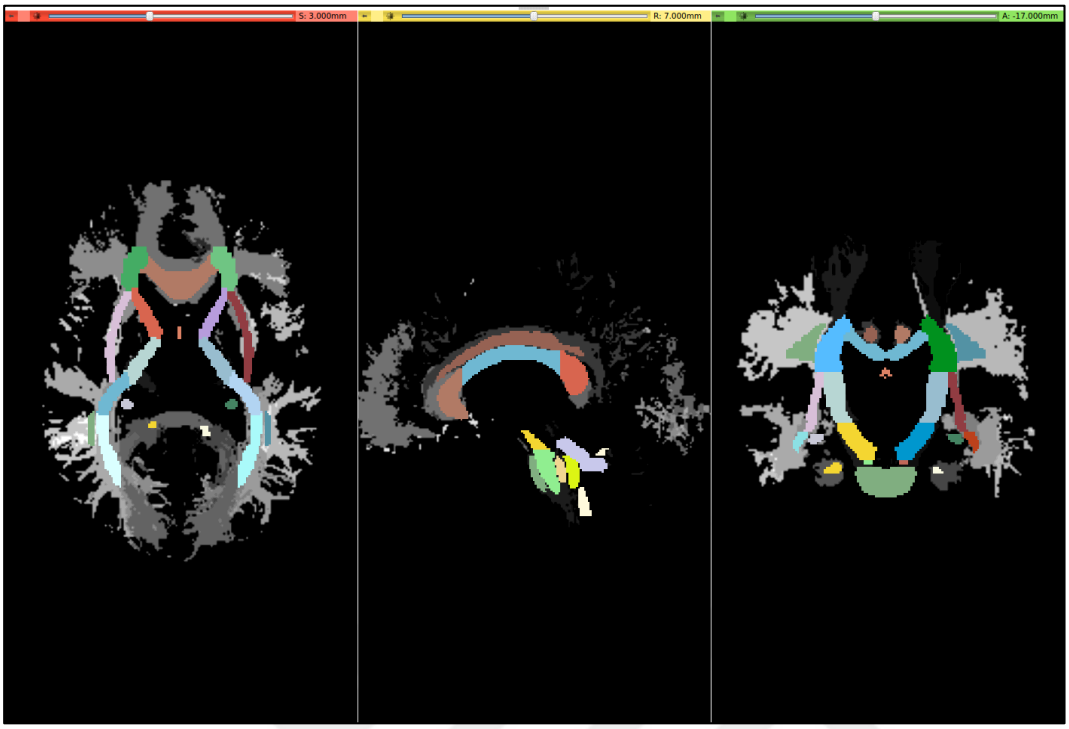

Figure 52: JHU atlas white matter tracts and areas.

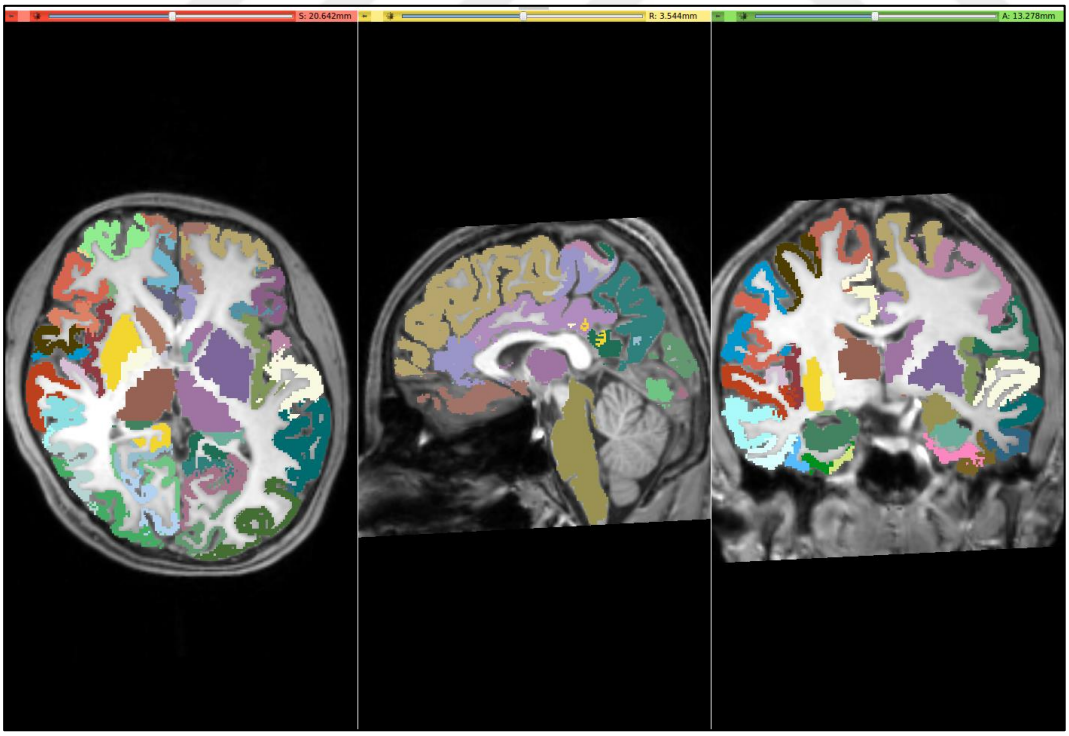

Figure 53: Gray matter areas registered on T1 image.

4.2.5. Results

We have conducted two performance tests to analyze the effectiveness of the proposed method. First, we have analyzed the models generated by TPDS in comparison with VBA and TBSS. Hereby, we have adapted directional statistics to TPDS, TBSS and VBA to compare their overall efficiency in representing vector-based statistical models. This test aims to show the efficiency of tract profiling over voxel based and skeleton based analysis. Second, we have applied the full TPDS algorithm to the two subject populations (i.e. MDD versus Health Controls) and compared the results with network based statistics, NBS. This test aims to show the efficiency of combining tract profiles with directional statistics over conventional methods. In this test, the effects of fiber length in estimating group differences are also evaluated.

Table 3: Region of interest areas.

1	Middle cerebellar peduncle	25	Superior corona radiata R
2	Pontine crossing tract	26	Superior corona radiata L
3	Genu of corpus callosum	27	Posterior corona radiata R
4	Body of corpus callosum	28	Posterior corona radiata L
5	Splenium of corpus callosum	29	Posterior thalamic radiation (include optic radiation) R
6	Fornix (column and body of fornix)	30	Posterior thalamic radiation (include optic radiation) L
7	Corticospinal tract R	31	Sagittal stratum (include inferior longitidinal fasciculus and inferior fronto-occipital fasciculus) R
8	Corticospinal tract L	32	Sagittal stratum (include inferior longitidinal fasciculus and inferior fronto-occipital fasciculus) L
9	Medial lemniscus R	33	External capsule R
10	Medial lemniscus L	34	External capsule L
11	Inferior cerebellar peduncle R	35	Cingulum (cingulate gyrus) R
12	Inferior cerebellar peduncle L	36	Cingulum (cingulate gyrus) L
13	Superior cerebellar peduncle R	37	Cingulum (hippocampus) R
14	Superior cerebellar peduncle L	38	Cingulum (hippocampus) L
15	Cerebral peduncle R	39	Fornix (cres) / Stria terminalis
16	Cerebral peduncle L	40	Fornix (cres) / Stria terminalis
17	Anterior limb of internal capsule R	41	Superior longitudinal fasciculus R
18	Anterior limb of internal capsule L	42	Superior longitudinal fasciculus L
19	Posterior limb of internal capsule R	43	Superior fronto-occipital fasciculus R
20	Posterior limb of internal capsule L	44	Superior fronto-occipital fasciculus L
21	Retrolenticular part of internal capsule R	45	Uncinate fasciculus R
22	Retrolenticular part of internal capsule L	46	Uncinate fasciculus L
23	Anterior corona radiata R	47	Tapetum R
24	Anterior corona radiata L	48	Tapetum L

4.2.5.1. Analysis of the Strengths of VBA, TBSS and TPDS in Tract Modeling

In this test, we used a single group (i.e. healthy subjects). The statistics were derived using three different methods, VBA, TBSS and TPDS, only on white matter areas – not GM ROIs. As seen in Figure 54, the white matter areas that have been segmented using FreeSurfer are mapped to ICBM DTI 81 Atlas (Mori et al. 2008) to allow for inter-subject data aggregation. For VBA analysis, the atlas-based white matter areas are overlayed for all subjects for further processing. For TPDS analysis, tract profiles are generated from the atlas mappings of all subjects. In TBSS, before performing atlas mapping, skeletonized areas are generated from individual subject tracts. The rest of the data processing pipeline is the same for all three methods. At the first step, for each ROI, based on which method is used for defining the tract, PDDs are generated. Then these PDDs are parametrically modeled by two separate directional distributions, namely Bingham and Watson. Finally in the last step, several PDDs are generated to represent the entire group using the newly developed parametrical models and goodness of fit is computed to evaluate how good the chosen model is.

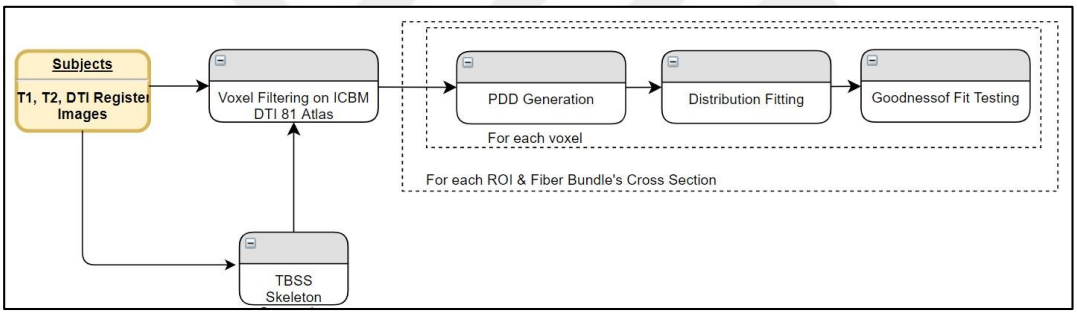

Figure 54: Comparison of VBA/TBSS with TPDS data processing pipeline.

Hereby, to have a common framework for three methods, following goodness of fit analysis has been conducted.

<u>PDD Generation</u>

For each subject, primary diffusion directions are extracted for each voxel inside the given WM area using the primary eigenvector of the diffusion tensor. The WM area differs based on the chosen representation. In VBA, the WM area is extracted based on segmentation of the specific WM ROI. In TBSS, it is based on the skeleton of the tract in the WM ROI. In TPDS, it is embodied within each tract profile that compose the entire tract in the WM ROI. Aggregated data from all subjects compose the data to be fitted for each WM area.

Distribution Fitting

Watson and Bingham distributions were fitted to model each tract using the maximum likelihood method. For each tract, the parameters of the theoretical model were estimated from the pdf at hand. Then this theoretical probability density function was evaluated iteratively using synthetic random vector data for a total of 700 vectors that were almost uniformly distributed along a sphere. Finally, the difference between the estimated pdf and the random pdf is tested for null hypothesis.

Goodness of Fit Testing

Pearson's Chi Square tests have been used for goodness of fit tests to evaluate whether observed frequency distribution differs from the theoretical distribution. Comparison of distributions are done using ANOVA where Chi Square test statistics for each ROI.

In order to apply Pearson's Chi Square tests to test whether observed frequency distribution differs from a theoretical distribution, the following steps are applied on the original data and synthetic random vector data and respective models.

1. For Watson distribution, the sample mean direction, $\bar{R}$, has been evaluated as regular vector sum of the vectors under population of vectors. The mean direction is a unit vector that is in the same direction with R. $\bar{x} = \frac{\sum_i x_i}{R}$, $\bar{y} = \frac{\sum_i y_i}{R}$, $\bar{z} = \frac{\sum_i z_i}{R}$
2. For Bingham distribution, the axis of moment of Inertia of sample, $\bar{t}$, has been evaluated using scatter matrix of the distribution S. For bi-polar case, it is the biggest eigenvector and for girdle case, it is the smallest eigenvector.
3. The transformations $\bar{\theta}, \bar{\phi}$ has been evaluated in order to shift either $\bar{R}$ or $\bar{t}$ to positive z axis.
4. The transformation has been applied to original and synthetic data.
5. The angle θ has been calculated as the angle between positive x axis and the projected vector on x-y plane. $0 < \theta < 2\pi$
6. The observed frequencies and expected frequencies as $\theta_1 < \theta < \theta_2$, where the number frequency bins is 50 and θ_2-θ_1 $\approx 7.2^o$

4.2.5.2. Analysis of the Group Difference Maps generated by NBS and TPDS

In this part, the proposed framework will be applied to test for differences of fiber tract profiles between MDD patients and control subjects. Based on the same fiber tracts and connectivity matrix for healthy volunteers, comparisons will be made with the results of Network Based Statistics. For this purpose, we used the 83x83 connectivity matrix generated at the end of data pre-processing by the connectome mapper

Network Based Statistics

In NBS, for each group, each pairwise association (i, j) between ROI I and ROI j is treated separately. First Fisher's r-to-z transform has been applied to ensure normality. Then, test statistic of interest –which is the normalized number of fiber bundles- is compared between the groups using t-statistic. In order to correct for multiple comparisons, permutation testing was used to select p-value controlled for the FWE for each connected component. For each permutation, the same threshold is applied to define a set of suprathreshold links of connected components. Suprathreshold and the number of permutations was set according to the default parameter settings of NBS.

Track profiling with Directional Statistics

In TPDS, the following procedure is repeated for each possible connection between distinct ROI pairs (i.e. 83x83 times divided by 2). Tract profiles between each ROI i and ROI j are extracted for the healthy and MDD groups. Then for each slice in the tract profiles, significance is tested with a threshold value of $p<0.005$. If there are n contiguous slices that satisfy this, it is indicated that the connection between ROIs i and j is significantly different between the control and patient groups. It is possible that there are multiple clusters of n contiguous slices that satisfy this condition. In order to reflect this information, we prepared a new 83x83 connectivity matrix, which contained the number of significantly different clusters between the two groups that are compared. Therefore, the difference map that is achieved through TPDS reflects a weighted graph. The more the number of significantly different n contiguous slices, the more the weight of the difference map.

Selection of n must be related with a criterion related to the plausible tract lengths in general. In order to eliminate premature tract termination that result from low SNR and low pathway anisotropy [32], 10 mm is the shortest tract length to be considered. Since DTI image has 2.2 mm spacing, choosing n as 4 satisfies this constraint. In other words, at least 4 consecutive cross-sectional areas must be found within a fiber bundle where the PDD of each cross-sectional area belongs to different Bingham distribution for control and MDD groups.

4.2.5.3. Comparison of VBA and TBSS with TPDS using Directional Statistics

As can be seen in Table 4, Among VBA, TBSS and TPDS, the best fitted distribution is more representative in TPDS because the goodness of fit scores are better according to the p values. In addition, based on the results of TPDS, the Bingham distribution is reported to be more favorable than Watson distribution because only 2 out of 48 white matter tracts are represented better with Watson. Obviously, it is evident that TPDS is a better alternative to represent tracts in comparison to VBA and TBSS, because it favors more parametrical fit to the entire set of fiber tracts.

Table 4: Comparison of VBA and TBSS with TPDS (VBA and TBSS have been adapted to run directional statistics).

ROI	VBA Distribution (pvalue)	TBSS Distribution (pvalue)	Tract Profiling Distribution (pvalue)
Middle cerebellar peduncle	**No Fit (0.803)**	**No Fit (0.425)**	Bingham (0.021)
Pontine crossing tract	**No Fit (0.092)**	Bingham (0.043)	Bingham (0.004)
Genu of corpus callosum	Bingham (0.030)	Bingham (0.032)	Bingham (0.007)
Body of corpus callosum	Bingham (0.001)	Bingham (0.001)	Bingham (0.031)
Splenium of corpus callosum	Bingham (0.046)	Bingham (0.036)	Bingham (0.045)
Fornix (column and body of fornix)	**No Fit (0.707)**	**No Fit (0.135)**	Bingham (0.017)
Corticospinal tract R	**No Fit (0.067)**	**No Fit (0.087)**	Bingham (0.048)
Corticospinal tract L	**No Fit (0.541)**	Bingham (0.041)	Bingham (0.025)
Medial lemniscus R	**No Fit (0.706)**	Watson (0.046)	Bingham (0.036)
Medial lemniscus L	**No Fit (0.278)**	**No Fit (0.078)**	**No Fit (0.090)**
Inferior cerebellar peduncle R	Watson (0.019)	Watson (0.037)	Bingham (0.016)
Inferior cerebellar peduncle L	**No Fit (0.970)**	**No Fit (0.570)**	Bingham (0.019)
Superior cerebellar peduncle R	Watson (0.032)	Bingham (0.042)	Bingham (0.045)
Superior cerebellar peduncle L	Watson (0.026)	Bingham (0.044)	Bingham (0.012)
Cerebral peduncle R	**No Fit (0.064)**	Bingham (0.044)	Bingham (0.023)
Cerebral peduncle L	**No Fit (0.078)**	Bingham (0.032)	Bingham (0.022)
Anterior limb of internal capsule R	Watson (0.030)	**No Fit (0.079)**	Watson (0.033)
Anterior limb of internal capsule L	Bingham (0.002)	Bingham (0.038)	Watson (0.025)
Posterior limb of internal capsule R	Watson (0.014)	**No Fit (0.067)**	Bingham (0.008)
Posterior limb of internal capsule L	Bingham (0.017)	Bingham (0.033)	Bingham (0.033)
Retrolenticular part of internal capsule R	Watson (0.034)	**No Fit (0.074)**	**No Fit (0.083)**
Retrolenticular part of internal capsule L	Watson (0.015)	**No Fit (0.065)**	**No Fit (0.106)**
Anterior corona radiata R	**No Fit (0.278)**	Bingham (0.012)	Bingham (0.045)
Anterior corona radiata L	Bingham (0.0012)	Bingham (0.002)	Bingham (0.001)
Superior corona radiata R	Watson (0.043)	Bingham (0.009)	Bingham (0.001)
Superior corona radiata L	**No Fit (0.165)**	Bingham (0.035)	Bingham (0.019)
Posterior corona radiata R	Watson (0.002)	Bingham (0.017)	Bingham (0.002)
Posterior corona radiata L	Watson (0.001)	Bingham (0.019)	Bingham (0.006)
Posterior thalamic radiation R	Bingham (0.003)	Bingham (0.002)	Bingham (0.024)
Posterior thalamic radiation L	Bingham (0.006)	Bingham (0.002)	Bingham (0.009)
Sagittal stratum R	**No Fit (0.188)**	**No Fit (0.488)**	Bingham (0.032)
Sagittal stratum L	**No Fit (0.065)**	**No Fit (0.265)**	Bingham (0.047)
External capsule R	Bingham (0.006)	Bingham (0.006)	Bingham (0.001)
External capsule L	Bingham (0.001)	Bingham (0.001)	Bingham (0.001)
Cingulum (cingulate gyrus) R	Bingham (0.015)	Bingham (0.033)	Bingham (0.003)
Cingulum (cingulate gyrus) L	Bingham (0.002)	Bingham (0.001)	Bingham (0.001)
Cingulum (hippocampus) R	Watson (0.004)	Bingham (0.004)	Bingham (0.001)
Cingulum (hippocampus) L	**No Fit (0.118)**	Bingham (0.019)	Bingham (0.041)
Fornix (cres) / Stria terminalis	Bingham (0.004)	**No Fit (0.050)**	Bingham (0.009)
Fornix (cres) / Stria terminalis	Bingham (0.012)	**No Fit (0.128)**	Bingham (0.005)
Superior longitudinal fasciculus R	Watson (0.002)	Bingham (0.043)	Bingham (0.021)
Superior longitudinal fasciculus L	Watson (0.025)	Bingham (0.040)	Bingham (0.011)
Superior fronto-occipital fasciculus R	Bingham (0.003)	Bingham (0.018)	Bingham (0.001)
Superior fronto-occipital fasciculus L	Bingham (0.044)	Bingham (0.026)	Bingham (0.006)
Uncinate fasciculus R	**No Fit (0.483)**	**No Fit (0.091)**	Bingham (0.003)
Uncinate fasciculus L	**No Fit (0.896)**	Bingham (0.039)	Bingham (0.002)
Tapetum R	**No Fit (0.595)**	**No Fit (0.092)**	Bingham (0.092)
Tapetum L	**No Fit (0.535)**	**No Fit (0.103)**	Bingham (0.004)

A close inspection of Table 4 reveals that in terms of representing a given WM tract parametrically, TBSS is superior to VBA, and TPDS is superior to TBSS. It is evident that VBA contains more noise than TBSS and TPDS, because it contains the entire WM area from all subjects. Due to high noise, VBA fails to represent some of the tracts parametrically. On the other hand, TBSS is better than VBA, because it removes the areas -hence noise associated in these parts- that lie outside the fiber bundles which constitute the skeleton. However, TBSS is not better than TPDS, because it smooths out the tracts while forming the skeleton and loses specificity. Overall, the tract profiles computed in TPDS are selective in choosing representative samples of the DWI's that are more informative, because outliers are removed while computing the medial line. Since the data points all belong to the same tract and on the same cross-section over medial line, very similar diffusion properties are expected for each analysis point. This tends to eliminate all negative effects of misalignment of images and partial volume effect. Due to this property, the computational effectiveness of TPDS is higher than other methods, because the model can be decided with much less number of data points.

The advantage of the Bingham distribution might be explained through the ease of fitting a griddle distribution in comparison to fitting a homogeneous mean direction distribution. The griddle distribution allows for more parameters, hence it makes the development of a more general model possible. Furthermore, the computational accuracy of the Bingham distribution is better because the tracts represented with this distribution fit to the PDD of the actual tracts with a smaller p value.

4.2.5.4. Comparison of the Group Differences in Connectivity Maps Using Network Based Statistics and TPDS

In NBS, with corrected $p<0.005$, 7 regions and 8 connections have been observed to contain lower FA in MDD. Particularly the connections in the right hemisphere, between superior frontal cortex and rostral/caudal components of the anterior cingulate cortex, caudate and inferior parietal cortices had lower FA in MDD. These connections are shown in Figure 55 as green lines.

In TPDS, significantly different connections between the healthy and MDD groups are seen in Figure 55 as red lines. The thickness of the lines reflects the weights, or in other words the number of cross sectional areas above the threshold n (eg. A weight value of 1 indicates that there exist only one slice cluster with significantly different n contiguous tract profiles, whereas a weight value of 6 indicates there exist 6 disjoint clusters of n contiguous tract profiles that are significantly different). The right hemisphere differences reported by NBS, namely frontal (superior frontal and rostral middle frontal), medial (caudal and rostral anterior cingulate) are also detected by our method. But additionally, TPDS revealed differences between the healthy and MDD populations in limbic, temporal cortex, occipital cortex and hippocampal connections, as well as a few left hemisphere areas such as amygdala, hippocampus and thalamus.

The strength of the tract profile structure lies in the reduction of the misalignment problem. Furthermore, observations of the directional changes become more specific because contributions of the local changes can be reported along the tract not by the contribution of isolated voxels but by several slices across the two ROIs. Therefore the proposed directional statistics comparison is expected to be a superior differentiator for especially long tracts.

In order to verify this, the following analysis has been done. For each tract connecting 83 different regions, z-score of each the length is plotted against z-score of the number of significantly different profile slices. For this purpose, the maximum overlapping shape (skeleton) is used. When regression lines are fitted to investigate the relationship with tract length and the number of different clusters, it is seen that the likelihood of finding clusters of voxels that differ in long tracts are higher in directional statistics. This has been also tested using a linear regression model, where it has been found that the z-score of tract length significantly correlated with z-score of the number of significantly different profile slices ($p<0.05$, Adjusted R-Squared: 0.00162) as seen in Figure 56. Although the effect size is small, we can indicate that TPDS is a powerful method to find differences in two populations, especially as the tract lengths get longer.

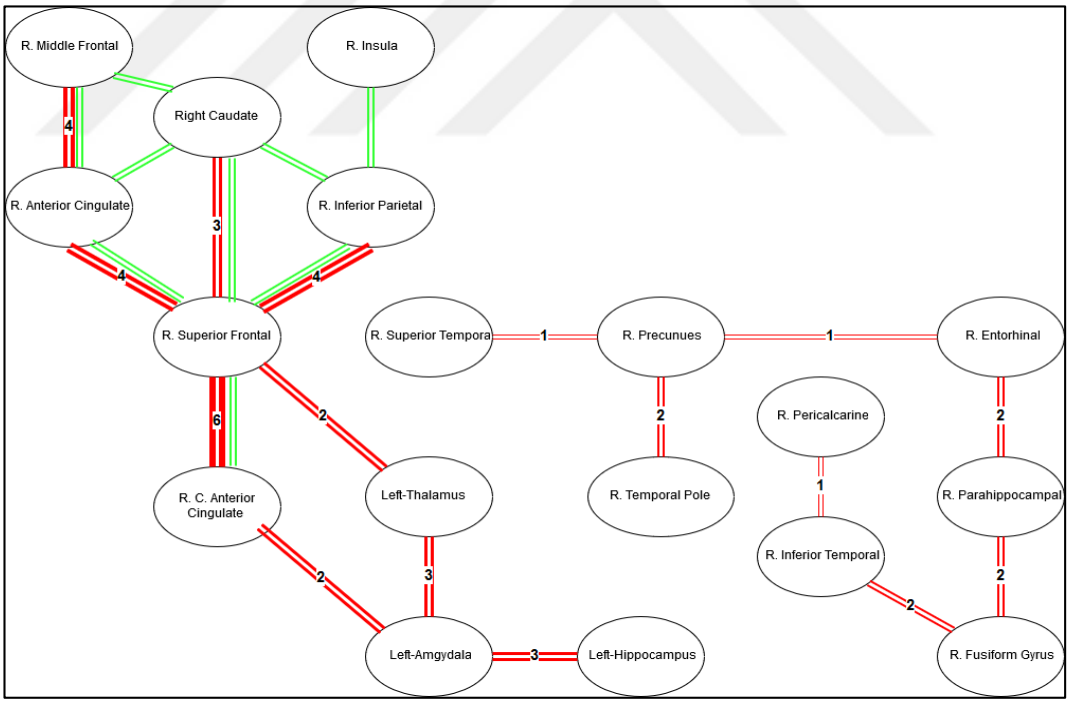

Figure 55: Map of ROIS with statistically different connectivity between control and patient groups. Green lines represent the common connections that are found different between the groups using NBS. Red lines represent the significantly different connections detected by the directional statistics using tract profiling.

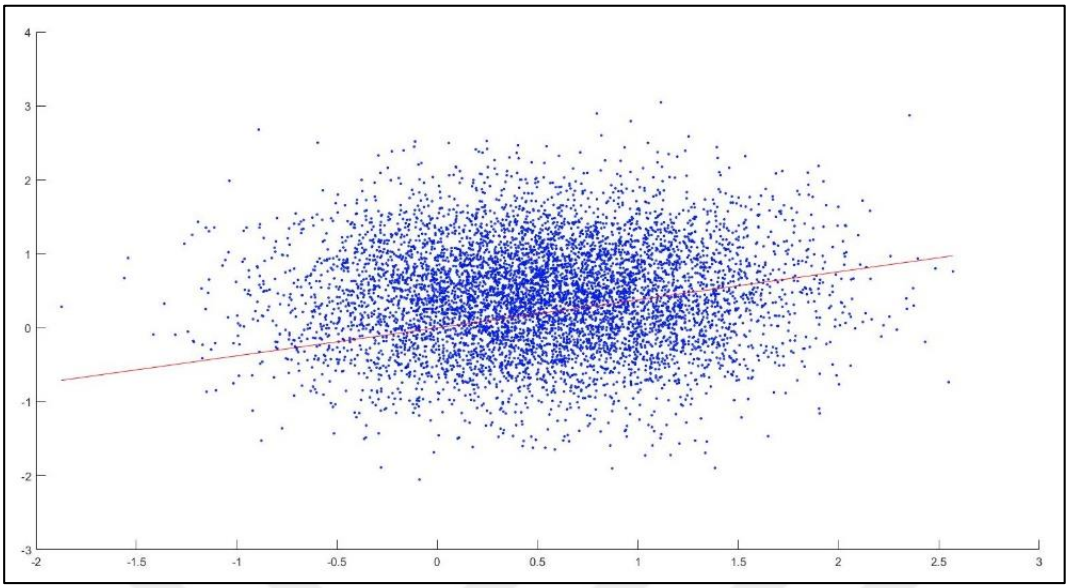

Figure 56: Scatter diagram of z-score of tract lengths versus significantly different clusters.

CHAPTER 5

CONCLUSION AND FUTURE WORK

In this study, we proposed novel frameworks for WM fiber connectivity analysis using a histogram based method and a tract profile based method with directional statistics (TPDS). In contrast with other group studies (Goodlett et al. 2009b) that are based on FA values, directional statistics deals with compact Riemannian manifolds, which allow observations regarding local diversities of principal diffusion directions of voxels in different groups of subjects.

The first method is histogram based group analysis that focus on developing a group analysis method that uses connectivity as well as diffusibility information (fractional anisotropy). Other than FA values, any other scalar metrics can be used. A fully automatized pipeline has been developed. Histogram based statistical group analysis method is a novel technique that cross matches FA values with tract lengths. This method has been implemented by extending the pipeline and applied on the real data. As far as I know, the method is unique that uses probabilistic tractograpy, cross matches FA according to fiber tracts lengths and apply statistical group comparison. The pipeline has been applied on limited set of MDD data and the analysis on Amygdala connections shows that entorinal cortex, hippocampus and insula connections are effected by MDD. For entorinal cortex for lower FA values (0.10-0.30) there is a pattern that for the MDD patients fiber tracts regardless of the tract length FA values are significantly bigger than control subjects. And for hippocampus and insula, nearly all range of FA values, it can be seen that the number of fiber tracts of control subjects are significantly bigger than MDD patients (Metin and Gokcay 2013).

On the other hand, in the second method, we used a pipeline implementation which can be regarded as quantitative tractography. We analyzed diffusion properties on the exact tracts and derived the statistics over sample points taking neighborhood cells into consideration. A similar method has been offered by Corouge et al. (2006) where diffusion properties along the fiber tracts, called fiber property profiles, were extracted. In that study, fiber tract parameterization was based on an arc length parameter, starting from each fiber's intersection with an "origin" plane. Goodlett et al. (2009a) also proposed a similar tract profiling approach, where diffusion properties are calculated along the tract for each fiber bundle. Our method introduces 3 main improvements to these quantitative tractography methods. First,

we are not just limiting the method with known anatomical fiber bundles but we can derive statistics from any pair of connected grey matter areas. Second, we have introduced skeletonization and pruning to allow for applying statistics only within common areas across the groups. Third, we introduced vector analysis using directional statistics instead of scalar analyses such as FA, MD etc.

There exist other methods which use directional statistics in DTI (Schwartzman, Dougherty, and Taylor 2005b) (Hutchinson et al. 2012). However, these methods analyze group differences based on ROIs, not fiber tracts, ignoring the underlying connectivity. We have devised the tract profiling algorithm to operate on relevant voxels among the fibers that connect each ROI obtained from fully automatic brain segmentation and parcellation. Local registration errors are reduced after calculating cross-sectional area of the fibers, and finding medial lines (i.e. profiles) to continue tract analysis. Afterwards, Bingham distribution, which is the most general form of directional distribution is used for tract based directional analysis, ensuring minimum parametric assumptions about the dataset. To the best of our knowledge this approach have not been implemented in group analysis of DTI before.

Neurite orientation dispersion and density imaging (NODDI) is a novel neurite imaging and analysis framework that provide sensible neurite density and orientation dispersion estimates (Zhang et al. 2012). Unlike FA, NODDI analyzes density and orientation dispersion separately. NODDI uses orientation distribution function (ODF), defined as Watson distribution which constrains the dispersion about the dominant orientation (Zhang et al. 2012). However, Bingham distribution fits better to diffusion properties, in comparison to Watson. Bingham-NODDI extends NODDI method by generalizing it with Bingham distribution to cover anisotropic orientation dispersions of neurites (Tariq et al. 2016) . Similarly, in our study, we found that modeling ODF using Bingham distribution explains the data better regardless of the tract identification, be it through VBA, TBSS or our method, TPDS. A major difference between our approach and NODDI is in the estimation of the dispersion. The modeling we used to implement the Bingham distribution estimates dispersion in the vicinity of the dominant orientation, separately for the primary and secondary dispersion orientations. This eliminates the key limitation of NODDI, which fails to model complex neurite configurations such as those arising from fanning and bending axons. On another front, just like ours, orientation dispersion (ODI) generated by the NODDI method can be also used with TBSS method instead of FA metric (Timmers et al. 2016)(Taoka et al. 2020). In this aspect, the main difference between our method and NODDI is in extending fiber dispersion along the tracts that connect 2 ROIs. By allowing such extension, our method enables using fiber dispersions as track characteristics and analyzing disease related effects on connectivity of the tracks other than the voxel itself.

We have demonstrated that in addition to scalar diffusibility changes, analyzing principal diffusion directions along a tract detects local changes better than scalar values. The strength of the directional statistics based analysis we proposed lies in its applicability to TBSS and VBA as well; it is not limited to tract profiles.

However, in directional statistics, the misalignment problem though the tract becomes more critical compared to scalar statistics like FA. Voxel-based analysis needs to register the subject's images to a common coordinate frame. However, the fiber tracts do not accurately align during this process due to variation in tract size and shape. Especially long-range fiber tracts contain more shape variation across subjects (Wassermann et al. 2011), so they are more prone to such misalignment. This problem is still valid for TBSS because even the voxel skeletons do not ensure that all relevant voxels correspond to the same tract (De Groot et al. 2013).

As seen from the results of the first set of performance tests, tract profiles are superior structures for resolving the shape differences in comparison to VBA and TBSS, because tract profiles are better in terms of fitting a model to PDD vectors. We investigated the goodness of fit characteristics of VBA and TBSS respectively on all WM areas and on skeletonized WM areas using directional statistics. We found that several tracts in VBA and TBSS are rejected to fit to the most general Bingham distribution which contains minimum assumptions about the data. In comparison when tract profiling is used, most tracts could be fit parametrically, except a few. A parametrical model is advantageous in data processing, since it facilitates population-based comparisons.

The aforementioned tests also show how directional statistics can be adapted to the widely used analysis methods such as TBSS or VBA. Instead of FA values, PDD vectors can be used over each voxel within the skeleton. FA metric uses the eigenvalues of the underlying diffusion characteristics of the voxel and defines only the amount of diffusion asymmetry, where PDD uses the first eigenvector of the diffusion characteristic. FA metric is sensitive to the underlying fiber architecture and correlates with PDD changes in disease conditions. However, FA does not have a direction attribute. Different orientations might result in the same FA value simply because orientational changes of the diffusion property of the voxel might not result in FA changes, when there is a difference in eigenvector orientation but not its value. So FA metric is not as sensitive as PDD in differentiating diffusion characteristics along the fiber track. As presented in chapter 4 , Bingham distribution fits better to describe the differences in majority of white matter tracks. Further studies should be conducted to ease adaptation of directional statistics to TBSS skeletons and also to resolve issues related to the multiple comparison problem.

PDD analysis using directional statistics is not a summary statistic of each track but a measurement of diffusional properties of the fiber bundle connecting a pair of ROIs. The statistics of each fiber track voxel are summarized by many points using directional statistics along the fiber bundle. Fiber bundle skeletonization and normalization of PDD over tract cross sections allows for error-correction and noise cancellation that might arise from tractography artifacts or misalignment. This should also be valid for trajectory changes of tracts under disease related conditions, as long as a prominent disfiguration or an abnormal morphological change caused by a tumor deviation does not severely divert the alignment of the fiber bundles. In

such a case, a lot of false positives may affect the model along the fiber bundles, hindering the correct estimation of PDDs along the actual, but diverted tract.

During the second set of performance tests, the results of tract profiling directional statistics (TPDS) and NBS are compared to see whether these methods report the differences between the healthy and MDD populations consistently. We found that most of the right hemisphere specific connectivity differences reported earlier in MDD have been detected by both of these approaches. The results are much more consistent among the shorter tracts such as frontal connections of the anterior cingulate. However, TPDS reveals additional connectivity differences mainly among longer tracts such as those between temporal and occipital cortex as well as those that contain areas with low FA values and higher crossing fibers such as amygdala, hippocampus and thalamus. Another strength of TPDS is due to its revelation about weights.

These findings are also consistent with MDD models proposed by Drevets (Drevets, Price, and Furey 2008) and Mayberg (Mayberg 2003) where MDD can be defined through a Limbic-cortical dysregulation model. In this model, Limbic–thalamo–cortical (LTC) circuits, involving the amygdala, thalamus, and orbital and medial PFC, and limbic–cortical–striatal–pallidal–thalamic (LCSPT) circuits are the mainly affected areas. These connections are found be affected both using NBS and TPDS. Additionally, TPDS revealed temporal, parietal and occipital cortex connections that are different in MDD. Mainly the differences on Inferior Fronto-Occipital tracts can be also supported by other DTI studies that report significantly decreased FA values among MDD patients (Cheng et al. 2014).

The ROIS that are reported to have statistically significant connectivity differences in MDD versus healthy participants are consistent with the two well-known lateralization models of emotion. According to the right hemisphere hypothesis, right hemisphere is dominant in emotional processing (Alves, Fukusima, and Aznar-Casanova 2008). On the other hand, the valence hypothesis posits that left hemisphere processes positive (or approach related) information, but the right hemisphere processes negative (or avoidance related) information (Alves, Fukusima, and Aznar-Casanova 2008). Within the context of MDD, hypoactivity in left hemisphere fronto-striatal loops indicate lack of downregulation of the sub-cortical areas. TPDS –but not NBS- reported differences in the connectivity of Left hemisphere amygdala, thalamus and hippocampus consistent with the valence hypothesis. Furthermore, the abundant presentation of right hemisphere ROIs support the right hemisphere hypothesis indicating that the connectivity within the right hemisphere may be a biomarker for MDD. TPDS revealed a larger right hemisphere network which was sidestepped by NBS. This network is predominantly composed of the basal temporal lobe structures as well as occipital ROIs such as precuneus and pericalcarine. Differences in the temporal and parietal functionality in MDD is reported less in comparison to front striatal structures, however, there is a growing body of literature that focuses on the hypoactivity of the right hemisphere temporal areas in MDD (Bruder, Stewart, and McGrath 2017). The detection of such

ROIs by TPDS is supportive of these studies reported in (Bruder, Stewart, and McGrath 2017). Finally, several rsfMRI biomarkers of MDD are reported in (Drysdale et al. 2017). After clustering these biomarkers through machine learning techniques, four different subtypes of MDD can be derived, based on four different clusters of ROIs. Unfortunately, the temporal areas of the brain are excluded in this study, due to a lack of data collection from several participating research sites. However, the ROI network reported by both NBS and TPDS in Figure 55 is also reported in (Drysdale et al. 2017), verifying our results in a much larger sample size.

In their meta-analysis over 231 patients with MDD and 261 comparison participants, Yi Liao et. al. (2013) found 4 consistent locations of decreased FA: white matter in the right frontal lobe, right fusiform gyrus, left frontal lobe and right occipital lobe. Mainly right inferior longitudinal fasciculus, right inferior fronto-occipital fasciculus and right posterior thalamic radiation involved in such changes (Liao et al. 2013). This covers most of the connection pairs we have found especially Right fusiform gyrus connections with R. Inferior Temporal, Parahipppocampal and temporal gray matter are important because NBS method failed to reveal all of these areas consistent with the meta-analysis.

In another meta-analysis (Wen et al. 2014), reduced FA is reported in the DLPFC and uncinate fasciculus (UF) of patients with late life depression (Wen et al. 2014). Those regions are part of frontostriatal and limbic networks consistent with our findings. This is also consistent with NBS analysis, especially the connections colored in green.

Another recent meta-analysis study have analyzed WM anisotropy and diffusivity in 1305 MDD patients and 1602 healthy controls (age range 12–88 years) from 20 samples worldwide (van Velzen et al. 2020). On the adults, lower FA was observed in 16 of the 25 ROIs. The largest changes have been found mainly in anterior corona radiata (ACR), corona radiata (CR), corpus callosum (CC), genu of the corpus callosum (GCC), body of the corpus callosum (BCC) and anterior limb of the internal capsule (ALIC). Significantly lower FA was also observed in the superior fronto-occipital fasciculus (SFO), sagittal stratum (SS), internal capsule (IC), posterior corona radiata (PCR), superior corona radiata (SCR), inferior fronto-occipital fasciculus (IFO), fornix/stria terminalis (FXST), external capsule (EC), and cingulate gyrus of the cingulum bundle (CGC). It is quite important to note that most of these regions are better fitted by TPDS in comparison to TBSS and VBA. Superior fronto-occipital fasciculus (Left-Right), Sagittal stratum (Left-Right), Superior corona radiata (Left-Right), Posterior corona radiata (Left-Right), Superior fronto-occipital fasciculus (Left-Right), Inferior fronto-occipital fasciculus (Left-Right), External capsule (Left-Right), Fornix (cres) / Stria terminalis (Left-Right), Cingulum (Left-Right) are all better modeled using TPDS. This is also true for Anterior and Superior Corona Radiata where only Right Anterior Corona Radiata are modelled better with TBSS skeleton. The parts of corpus callosum is on the other hand fitted better as Genu of corpus callosum for TPDS, Body of corpus callosum for VBA and Splenium of corpus callosum for TBSS.

To conclude, we have shown that by analyzing principal diffusion directions (PDD) using directional statistics, more insight is gained about fiber tracts regarding population differences. While other connectivity-based analysis methods may disregard the differences between longer fibers, TPDS becomes more robust as fiber tract length increases. In areas with low FA values, distribution of PDDs among the fiber tracts can differentiate connectivity-based dysfunctions better, due to the power of directional statistics. When we implemented TPDS in two subject populations, one healthy, the other with MDD, we found several WM tracts differences that are not reported in other methods such as NBS and TBSS. It is imperative to use TPDS on other subject populations and with more subjects to justify its strength in comparison to other methods that perform WM tract-based group analysis.

5.1. Future Work

Although in this study only voxel-wise analysis has been done, directional statistics can encapsulate much more information that empowers all of the areas described. Because it is based on statistics of vectors/directions and deals with observations on compact Riemannian manifolds, directional statistics can be used for not only voxel-wise and connectivity related group studies but also tractography, outlier detection and fiber clustering. In the future, these applications can be considered to enhance group studies and develop a better understanding of the structural correlates of clinical diagnoses. The directional statistics analysis suggested here can also be applied by augmenting the existing methods, namely TBSS and VBA. Such an addition to the existing methods is valuable because it opens up the possibility to use parametric fitting along with directional statistics. The proposed method could also be extended considering second and third directions of the diffusion tensor. This can be modeled separately, fitting different distribution model for each direction and analyzing the statistical changes of each direction in disease conditions.

REFERENCES

Agartz, I., Andersson, J. L. R. & Skare, S. (2001). Abnormal brain white matter in schizophrenia: A diffusion tensor imaging study. NeuroReport, 12, 2251–2254.

Alexopoulos, G. S., Kiosses, D. N., Choi, S. J., Murphy, C. F. & Lim, K. O. (2002). Frontal white matter microstructure and treatment response of late-life depression: a preliminary study. Am. J. Psychiatry, 159, 1929–1932.

American Psychiatric Association. (2000). Diagnostic and statistical manual of mental disorders (DSMIV-TR). (4th Ed.). Arlington: American Psychiatric Publishing.

Arsigny, V., Fillard, P., Pennec, X. & Ayache, N. (2005). Fast and simple calculus on tensors in the log-Euclidean framework. Proc Med Image Comput Comput-Assist Intervent – MICCAI, 3749, 115–222.

Ashburner, J. & Friston, K. J. (2000). Voxel-based morphometry – The methods. NeuroImage, 11, 805–821.

Ballmaier, M., Toga, A. W., Blanton, R. E., Sowell, E. R., Lavretsky, H., Peterson, J., Pham, D. & Kumar, A. (2004). Anterior cingulate, gyrus rectus, and orbitofrontal abnormalities in elderly depressed patients: An MRI-based parcellation of the prefrontal cortex. Am. J. Psychiatry, 161, 99–108.

Bansal, R., Staib, L. H., Plessenb, K. J., Xua, D., Royal, J. & Peterson, B. S. (2007). Voxel-wise comparisons of the morphology of diffusion tensors across groups of experimental subjects. Neuroimaging, 156, 225–245.

Barnea-Goraly, N., Kwon, H., Menon, V., Eliez, S., Lotspeich, L. & Reissa, A. L. (2004). White matter structure in autism: preliminary evidence from diffusion tensor imaging. Biological Psychiatry, 55(3), 323-326.

Basser, P. J. & Pierpaoli, C. (1996). Microstructural and physiological features of tissues elucidated by quantitative-diffusion-tensor MRI. J. Magn. Reson. B, 111, 209–219.

Basser, P. J., Pajevic, S., Pierpaoli, C., Duda, J. & Aldroubi, A. (2000). In vivo fiber tractography using DT-MRI data. Magn. Reson. Med., 44, 625–632.

Batchelor, P. G., Hill, D. L. G., Atkinson, D., Calamante, F. & Conelly, A. (2002). Fiber tracking by solving the diffusion-convection equation. Proc. International Soc. Magn. Reson. Med., 1135.

Batchelor, P., Calamante, F., Tournier, J. D., Atkinson, D., Hill, D. L. & Connelly, A. (2006). Quantification of the shape of fiber tracts. Magn. Reson. Med., 55, 894–903.

Beaulieu, C. (2002). The basis of anisotropic water diffusion in the nervous system: A technical review. NMR Biomed, 15, 435–455.

Behrens, T. E., Johansen-Berg, H., Woolrich, M. W., Smith, S. M., Wheeler-Kingshott, C. A., Boulby, P. A., Barker, G. J., Sillery, E. L., Sheehan, K., Ciccarelli, O., Thompson, A. J., Brady, J. M. & Matthews, P. M. (2003). Non-invasive mapping of connections between human thalamus and cortex using diffusion imaging. Nat. Neurosci., 6, 750–757.

Benjamini, Y. & Yekutieli, D. (2001). The control of the false discovery rate in multiple testing under dependency. Annals of Statistics, 29(4), 1165–1188.

Bonekamp, D., Nagae, L. M., Degaonkar, M., Matson, M., Abdalla, W. M., Barker, P. B., Mori, S. & Horska, A. (2007). Diffusion tensor imaging in children and adolescents: Reproducibility, hemispheric, and age-related differences. NeuroImage 34, 733-742.

Brody, A. L., Saxena, S., Silverman, D. H., Alborzian, S., Fairbanks, L. A., Phelps, M. E., Huang, S. C., Wu, H. M., Maidment, K. & Baxter Jr., L. R. (1999). Brain metabolic changes in major depressive disorder from pre- to post-treatment with paroxetine. Psychiatry Res., 91, 127–139.

Brody, A. L., Saxena, S., Stoessel, P., Gillies, L. A., Fairbanks, L. A., Alborzian, S., Phelps, M. E., Huang, S. C., Wu, H. M., Ho, M. L., Ho, M. K., Au, S. C., Maidment, K. & Baxter Jr., L.R. (2001). Regional brain metabolic changes in patients with major depression treated with either paroxetine or interpersonal therapy: Preliminary findings. Arch Gen Psychiatry, 58(7), 631-640.

Brun, A. (2006). Manifold learning and representations for image analysis and visualization. Thesis eksik

Brun, A., Knutssona, H., Park, H. J., Shenton, M. E. & Westin, C. F. (2004). Clustering fiber traces using normalized cuts. MICCAI LNCS, 3216, 368–375.

Buchsbaum, M. S., Tang, C. Y., Peled, S., Gudbjartsson, H., Lu, D., Hazlett, E. A., Downhill, J., Haznedar, M., Fallon, J. H. & Atlas, S. W. (1998). MRI white matter diffusion anisotropy and PET metabolic rate in schizophrenia. NeuroReport, 9, 425–430.

Burns, J., Job, D., Bastin, M. E., Whalley, H., Macgillivray, T., Johnstone, E. C. & Lawrie, S. M. (2003). Structural disconnectivity in schizophrenia: A diffusion tensor magnetic resonance imaging study. The British Journal of Psychiatry, 182(5), 439-443.

Castaneda, A. E., Tuulio-Henriksson, A., Marttunen, M., Suvisaari, J. & Lonnqvist, J. (2008). A review on cognitive impairments in depressive and anxiety disorders with a focus on young adults. J. Affect. Disord., 106, 1–27.

Cohen, J. D., Botvinick, M. & Carter, C. S. (2000). Anterior cingulate and prefrontal cortex: who's in control?. Nat. Neurosci., 3, 421–423.

Conturo, T. E., Lori, N. F., Cull, T. S., Akbudak, E., Snyder, A. Z., Shimony, J. S., McIntyre, R. C., Burton, H. & Rachel, M. E. (1999) . Tracking neuronal fiber pathways in the living human brain. Proc. Natl. Acad. Sci., 96, 10422–10427.

Cook, P. A., Bai, Y., Nedjati-Gilani, S., Seunarine, K. K., Hall, M. G., Parker, G. J. & Alexander, D. C. (2006). Camino: Open-source diffusion-MRI reconstruction and processing. 14th Scientific Meeting of the International Society for Magnetic Resonance in Medicine, Seattle, WA, USA.

Corouge, I., Fletcher, P. T., Joshi, S., Gilmore, J. H. & Gerig, G. (2005). Fiber tract-oriented statistics for quantitative diffusion tensor MRI analysis. Medical Image Computing and Computer Asisted Intervention (MICCAI 2005) LNCS, 3749, 131-139.

Corouge, I., Gouttard, S. & Gerig, G. (2004). Towards a shape model of white matter fiber bundles using diffusion tensor MRI. Proceedings of International Symposium on Biomedical Imaging (ISBI), 1(5), 344–347.

Cotter, D. A. (2003). Neuropathology of mood disorders. Mol Psychiatry, eksik

Counsell, S., Allsop, J., Harrison, M., Larkman, D., Kennea, N., Kapellou, O., Cowan, F., Hajnal, J., Edwards, A. & Rutherford, M. (2003). Diffusion-weighted imaging of the brain in preterm infants with focal and diffuse white matter abnormality. Pediatrics, 112(1), 1–7.

Cullen, K. R., Klimes-Dougan, B., Muetzel, R., Mueller, B. A., Camchong, J., Houri, A., Kurma, S. & Lim, K. O. (2010). Altered white matter microstructure in adolescents with major depression: a preliminary study. J. Am. Acad. Child Adolesc. Psychiatry, 49, 173–183.

Ding, Z., Gore, J. C. & Anderson, A.W. (2003). Classification and quantification of neuronal fiber pathways using diffusion tensor MRI. Mag. Reson. Med., 49, 716–721.

do Carmo, M. P. (1992). Riemannian geometry. Boston, MA: Birkhauser.

Drevets, W. (2001). Neuroimaging and neuropathological studies of depression: Implications for the cognitive emotional manifestations of mood disorder. Curr. Opin. Neurobiol., 11, 240–249.

Drevets, W. C., Price, J. L. & Furey, M. L. (2008). Brain structural and functional abnormalities in mood disorders: Implications for neurocircuitry models of depression. Brain Struct. Funct., 213, 93–118.

Ellis, C. M., Simmons, A., Jones, D. K., Bland, J., Dawson, J. M., Horsfield, M. A., Williams, S. C. R. & Leigh, P. N. (1999). Diffusion tensor MRI assesses corticospinal tract damage in ALS. Neurology, 53, 1051–1058.

Eriksson, S. H., Rugg-Gunn, F. J., Symms, M. R., Barker, G. J. & Duncan, J. S. (2001). Diffusion tensor imaging in patients with epilepsy and malformations of cortical development. Brain, 124, 617–626.

Fields, R. D. (2008). White matter in learning, cognition and psychiatric disorders. Trends Neurosci., 31, 361–370.

Fillard, P. & Gerig, G. (2003). Analysis tool for diffusion tensor MRI. MICCAI, 12, 967–968.

Fisher, N. I., Lewis, T. & Embleton, B. J. J. (1993). Statistical analysis of spherical data. UK: Cambridge University Press.

Fisher, R. A. (1953). Dispersion on a sphere. Proc. Roy. Soc. London Ser. A., 217, 295–305.

Fletcher, P. T. & Joshi, S. (2004). Principal geodesic analysis on symmetric spaces: Statistics of diffusion tensors. In Comput. Vis. Math. Methods Med. Biomed, Image Anal., ECCV 2004 Workshops CVAMIA MMBIA, Prague, Czech Republic.

Flöel, A., de Vries, M. H., Scholz, J., Breitenstein, C. & Johansen-Berg, H. (2009). White matter integrity in the vicinity of Broca's area predicts grammar learning success. NeuroImage, 47, 1974–1981.

Foong, J., Maier, M., Clark, C. A., Barker, G. J., Miller, D. H. & Ron, M. A. (2000). Neuropathological abnormalities of the corpus callosum in schizophrenia: A diffusion tensor imaging study. J. Neurol. Neurosurg. Psychiatry, 68, 242–244.

FSL, http://www.fmrib.ox.ac.uk/fsl/ Last accessed: 18.02.2019.

Gaffney, S. & Smyth, P. (2003). Curve clustering with random effects regression mixtures. (Edt.: Bishop, C. M. & Frey, B. J.). In Proc. Ninth Int. Workshop on AI and Stat., Florida, USA.

Gembris, D., Schumacher, H. & Suter, D. (2001). Solving the diffusion equation for fiber tracking in the living human brain. Proceedings of the International Society for Magnetic Resonance in Medicine, Glasgow, Scotland.

Gerig, G., Gouttard, S. & Corouge, I. (2004). Analysis of brain white matter via fiber tract modeling. Proc. IEEE Int. Conf. EMBS, 54, 4421–4424.

Gilmore, J. H., Lin, W., Corouge, I., Vetsa, Y. S., Smith, J. K., Kang, C., Gu, H., Hamer, R. A., Lieberman, J. A. & Gerig, G. (2007). Early post-natal development of corpus callosum and corticospinal white matter assessed with quantitative tractography. American Journal of Neuroradiology, 28(9), 1789-1795.

Giorgio, A., Watkins, K. E., Chadwick, M., James, S., Winmill, L., Douaud, G., De Stefano, N., Matthews, P. M., Smith, S. M., Johansen-Berg, H. & James, A. C. (2010). Longitudinal changes in grey and white matter during adolescence. Neuroimage. 49(1), 94-103.

Glauche, V., Sach, M., Koch, M., Heimbach, B., Winkler, G., Nolte, U., Fintersbusch, J., Frahm, J., Weiller, C. & Buchel, C. (2001). Morphometry on diffusion tensor data. NeuroImage 13, 128.

Goldapple, K., Segal, Z., Garson, C., Lau, M., Bieling, P., Kennedy, S. & Mayberg, H. (2004). Modulation of cortical–limbic pathways in major depression: Treatment specific effects of cognitive behavioral therapy compared to paroxetine. Arch. Gen. Psychiatry, 61, 34–41.

Goodlett, C. B., Fletcher, P. T., Gilmore, J. H. & Gerig, G. (2009). Group analysis of DTI fiber tract statistics with application to neurodevelopment. NeuroImage, 45(1), 133-142.

Guo, A. C., Petrella, J. R., Kurtzberg, J. & Provenzale, J. M. (2001). Evaluation of white matter anisotropy in krabbe disease with diffusion tensor MR imaging: Initial experience. Radiology, 218(3), 809-815.

Hae-Jeong, P. (2005). Quantification of white matter using diffusion-tensor imaging. International Review of Neurobiology, 66.

Hageman, N. S., Toga, A. W., Narr, K. L. & Shattuck, D. W. (2009). A diffusion tensor imaging tractography algorithm based on navier–stokes fluid mechanics. IEEE Transactions on Medical Imaging, 28(3).

Hagmann, P., Jonasson, L., Maeder, P., Thiran, J.-P., Wedeen, V. J. & Meuli, R. (2006). Understanding diffusion MR imaging techniques: From scalar diffusion-weighted imaging to diffusion tensor imaging and beyond. RadioGraphics, 26, 205-223.

Hagmann, P., Thiran, J. P., Jonasson, L., Vandergheynst, P., Clarke, S., Maeder, P. & Meuli, R. (2007). DTI mapping of human brain connectivity: Statistical fibre tracking and virtual dissection. Neuroimage, 19, 545–554.

Harrison, P. J. (2002). The neuropathology of primary mood disorder. Brain, 125(7), 1428-1449.

Hecke, W. V., Leemans, A., De Backer, S., Jeurissen, B., Parizel, P. M. & Sijbers, J. (2010). Comparing isotropic and anisotropic smoothing for voxel-based DTI analyses: A simulation study. Human Brain Mapping, 31, 98–114.

Hedehus, M., Sullivan, E. V., de Crespigny, A., Moseley, M. E., Lim, K. O. & Pfefferbaum, A. (1999). Low white matter anisotropy in chronic alchoholism revealed with diffusion tensor imaging. Int. Soc. Magn. Reson. Med., 2, 932.

Heiervang, E., Behrens, T., Mackay, C., Robson, M. & Johansen-Berg, H. (2006). Between session reproducibility and between subject variability of diffusion MR and tractography measures. NeuroImage, 33(3), 867–877.

Hermoye, L., Saint-Martin, C., Cosnard, G., Lee, S.K., Kim, J., Nassogne, M.C., Menten, R., Clapuyt, P., Donohue, P. K., Hua, K., Wakana, S., Jiang, H., van Zijl, P. C. & Mori, S. (2006). Pediatric diffusion tensor imaging: Normal database and observation of the white matter maturation in early childhood. NeuroImage, 29(2), 493-504.

Herrmann, L. L., Le Masurier, M. & Ebmeier, K. P. (2008). White matter hyperintensities in late life depression: a systematic review. J. Neurol. Neurosurg. Psychiatr., 79, 619–624.

Hutchinson, E. B., Rutecki, P. A., Alexander, A. L. & Sutula, T. P. (2012). Fisher statistics for analysis of diffusion tensor directional information. J Neurosci Methods., 206(1), 40-45.

Johnston-Wilson, N. L., Sims, C. D., Hofmann, J. P., Anderson, L., Shore, A. D., Torrey, E. F. & Yolken, R. H. (2000). Disease-specific alterations in frontal cortex brain proteins in schizophrenia, bipolar disorder, and major depressive disorder. The Stanley Neuropathology Consortium. Mol Psychiatry, 5, 142–149.

Jones, D. K. & Cercignani M., (2010). Twenty-five Pitfalls in the Analysis of Diffusion MRI Data. NMR in Biomedicine, 23, 803-820.

Jones, D. K., Catani, M., Pierpaoli, C., Reeves, S. J., Shergill, S. S., O'Sullivan, M., Golesworthy, P., McGuire, P., Horsfield, M. A., Simmons, A., Williams, S. C. & Howard, R. J. (2006). Age effects on diffusion tensor magnetic resonance imaging tractography measures of frontal cortex connections in schizophrenia. Hum. Brain Mapp., 27, 230–238.

Jones, D. K., Simmons, A., Williams, S. C. & Horsfield, M. A. (1999). Non-invasive assessment of axonal fiber connectivity in the human brain via diffusion tensor MRI. Magn. Reson. Med., 42, 37–41.

Jones, D. K., Symms, M., Cercignani, M. & Howard, R. (2005). The effect of filter size on VBM analyses of DT-MRI data. NeuroImage, 26, 546–554.

Kennedy, S. H., Evans, K. R., Kruger, S., Mayberg, H. S., Meyer, J. H., McCann, S., Arifuzzman, A. I., Houle, S. & Vaccarino, F. J. (2001). Changes in regional brain glucose metabolism measured with positron emission tomography after paroxetine treatment of major depression. Am. J. Psychiatry, 158, 899–905.

Kent, J. (1982). The Fisher–Bingham distribution on the sphere. J Royal Stat Soc, 44, 71–80.

Kerns, J. G., Cohen, J. D., MacDonald, A. W., Cho, R. Y., Stenger, V. A. & Carter, C. S. (2004). Anterior cingulate conflict monitoring and adjustments in control. Science, 303, 1023–1026.

Khurd, P., Verma, R. & Davatzikos, C. (2006). On characterizing and analyzing diffusion tensor images by learning their underlying manifold structure. Proceedings of the 2006 Conference on Computer Vision and Pattern Recognition Workshop, 17-22 June 2006, New York, USA.

Kieseppa, T., Eerola, M., Mantyla, R., Neuvonen, T., Poutanen, V. P., Luoma, K., Tuulio-Henriksson, A., Jylha, P., Mantere, O., Melartin, T., Rytsala, H., Vuorilehto, M. & Isometsa, E. (2010). Major depressive disorder and white matter abnormalities: a diffusion tensor imaging study with tract-based spatial statistics. Journal of Affective Disorders, 120, 240–244.

Klingberg, T., Hedehus, M., Temple, E., Salz, T., Gabrieli, J. D. E., Moseley, M. E. & Poldrack, R. A. (2000). Microstructure of temporo- parietal white matter as a basis for reading ability: Evidence from diffusion tensor magnetic resonance imaging. Neuron, 25, 493–500.

Koch, M. A., Norris, D. G. & Hund-Georgiadis, M. (2002). An investigation of functional and anatomical connectivity using magnetic resonance imaging. Neuroimage, 16, 241–250.

Kubicki, M., Park, H., Westin, C., Nestor, P., Mulkern, R., Maier, S., Niznikiewicz, M., Connor, E., Levitt, J., Frumin, M., Kikinis, R., Jolesz, F., McCarley, R. & Shenton, M. (2005). DTI and MTR abnormalities in schizophrenia: Analysis of white matter integrity. NeuroImage, 26(3), 1109-1118.

Kubicki, M., Westin, C.-F., Maier, S., Frumin, M., Nestor, P., Salisbury, D., Kikinis, R., Jolesz, F., McCarley, R. & Shenton, M. (2002). Uncinate fasciculus findings in schizophrenia: A magnetic resonance diffusion tensor imaging study. American Journal of Psychiatry, 159(5), 813–820.

Kuhn, H. W. (1955). The Hungarian method for the assignment problem. Nav. Res. Logist., 2, 83–97.

Le Bihan, D. (2003). Looking into the functional architecture of the brain with diffusion MRI. Nat Rev Neurosci, 4, 469–480.

Lim, K. & Helpern, J. (2002). Neuropsychiatric applications of DTI— a review. NMR in Biomedicine, 15(2), 587–593.

Lim, K. O., Hedehus, M., Moseley, M. E., de Crespigny, A., Sullivan, E. V. & Pfefferbaum, A. (1999). Compromised white matter tract integrity in schizophrenia inferred from diffusion tensor imaging. Arch. Gen. Psychiatry, 56, 367–374.

Ma, N., Li, L., Shu, N., Liu, J., Gong, G., He, Z., Li, Z., Tan, L., Stone, W. S., Zhang, Z., Xu, L. & Jiang, T. (2007). White matter abnormalities in first-episode, treatment-naive young adults with major depressive disorder. Am. J. Psychiatry, 164, 823–826.

MacDonald, A. W., Cohen, J. D., Stenger, V. A. & Carter, C. S. (2000). Dissociating the role of the dorsolateral prefrontal and anterior cingulate cortex in cognitive control. Science, 288, 1835–1838.

Maddah, M., Grimson, W. E. L., Warfield, S. K. & Wells, W. M. (2008). A unified framework for clustering and quantitative analysis of white matter fiber tracts. Medical Image Analysis, 12, 191–202.

Mahnaz, M., Wells, W. M., Warfield, S. K., Westin, C.-F. & Grimson, W. E. L. (2007). Probabilistic clustering and quantitative analysis of white matter fiber tracts, IPMI 2007. LNCS, 4584, 372–383.

Mardia, K. V. & Jupp, P. E. (2000). Directional statistics. New Jersey: John Wiles and Sons.

Martin, K., Papadakis, N., Huang, C., Hall, L. D. & Carpenter, T. (1999). The reduction of the sorting bias in the eigenvalues of the diffusion tensor. Magnetic Resonance Imaging, 17(6), 893–901.

Mayberg H. S., Brannan, S. K., Tekell, J. L., Silva, J. A., Mahurin, R. K., McGinnis, S. & Jerabek, P. A. (2000). Regional metabolic effects of fluoxetine in major depression: serial changes and relationship to clinical response. Biol. Psychiatry, 48, 830– 843. [END]

Mayberg, H. S. (2003). Modulating dysfunctional limbic-cortical circuits in depression: Towards development of brain-based algorithms for diagnosis and optimised treatment. British Medical Bulletin, 65, 193-207.

Mayberg, H. S. (2006). Defining neurocircuits in depression. Psychiatric Annals, 36, 4, 259.

Mayberg, H. S., McIntosh, A. R., Seminowicz, D. A., Goldapple, K., Kennedy, S., Segal, Z. & Rafi-Tarib, S. (2004). Limbic–frontal circuitry in major depression: a path modeling metanalysis. NeuroImage, 22, 409–418.

McClintock, S. M., Husain, M. M., Greer, T. L. & Cullum, C. M. (2010). Association between depression severity and neurocognitive function in major depressive disorder: a review and synthesis. Neuropsychology, 24, 9–34.

Metin, Mehmet Ozer, and Didem Gökçay. 2013. "Preliminary Results on Statistical Group Analysis of Probabilistic Tractography: Application to Major Depression Disorder." In INCF Neuroinformatics Congress in Stockholm, Sweden.

Metin, Mehmet Ozer, and Didem Gökçay. 2014. "Direction Statistics Methods Evaluation for Principal Diffusion Directions." In Human Brain Mapping, Barcelona.

Metin, Mehmet Ozer, and Didem Gökçay. 2021. "Diffusion Tensor Imaging Group Analysis Using Tract Profiling and Directional Statistics". Frontier Neuroscience (2021) Mar 22;15:625473. doi: 10.3389/fnins.2021.625473. PMID: 33828445; PMCID: PMC8019824

Mori, S., Crain, B. J., Chacko, V. P & van Zijl, P. C. (1999). Three-dimensional tracking of axonal projections in the brain by magnetic resonance imaging. Ann. Neurol., 45, 265–269.

Mori, S., Oishi, K., Jiang, H., Jiang, L., Li, X., Akhter, K., Hua, K., Faria, A. V., Mahmood, A., Woods, R., Toga, A. W., Pike, G. B., Neto, P. R., Evans, A., Zhang, J., Huang, H., Miller, M. I., van Zijl, P. & Mazziotta, J. (2008). Stereotaxic white matter atlas based on diffusion tensor imaging in an ICBM template. Neuroimage, 40, 570–582.

Nagy, Z., Westerberg, H., Skare, S., Andersson, J. L., Anders, L., Flodmark, O., Elisabeth, F., Kirsten, H., Birgitta, B., Hans, F., Hugo, L. & Torkel, K. (2003). Preterm children have disturbances of white matter at 11 years of age as shown by diffusion tensor imaging. Pediatric Research, 54(5), 672–679.

Nobuhara, K., Okugawa, G., Minami, T., Takase, K., Yoshida, T., Yagyu, T., Tajika, A., Sugimoto, T., Tamagaki, C., Ikeda, K., Sawada, S. & Kinoshita, T. (2004). Effects of electroconvulsive therapy on frontal white matter in late-life depression: a diffusion tensor imaging study. Neuropsychobiology, 50, 48–53.

Nobuhara, K., Okugawa, G., Sugimoto, T., Minami, T., Tamagaki, C., Takase, K., Saito, Y., Sawada, S. & Kinoshita, T. (2006). Frontal white matter anisotropy and symptom severity of late-life depression: a magnetic resonance diffusion tensor imaging study. J. Neurol. Neurosurg. Psychiatr., 77, 120–122.

O'Donnell, L. & Westin, C.F. (2005). White matter tract clustering and correspondence in populations. (Edt.: Duncan, J.S. & Gerig, G.). LNCS, 3749, 140–147.

O'Donnell, L. J., Westin, C.-F. & Golby, A. J. (2009). Tract-based morphometry for white matter group analysis. NeuroImage, 45, 832-844.

Oishi, K., Zilles, K., Amunts, K., Faria, A., Jiang, H., Li, X., Akhter, K., Hua, K., Woods, R., Toga, A. W., Pike, G. B., Rosa-Neto, P., Evans, A., Zhang, J., Huang, H., Miller, M. I., van Zijl, P. C., Mazziotta, J. & Mori, S. (2008). Human brain white matter atlas: identification and assignment of common anatomical structures in superficial white matter. Neuroimage, 43, 447–457.

Ongür, D., Ferry, A. T. & Price, J. L. (2003). Architectonic subdivision of the human orbital and medial prefrontal cortex. J Comp Neurol, 460, 425–449.

Pagani, E., Filippi, M., Rocca, M. & Horsfield, M. (2005). A method for obtaining tractspecific diffusion tensor MRI measurements in the presence of disease: Application to patients with clinically isolated syndromes suggestive of multiple sclerosis. NeuroImage, 26(1), 258–265.

Park, H.-J., Westin, C.-F., Kubicki, M., Maier, S., Niznikiewicz, M., Baer, A., Frumin, M., Kikinis, R., Jolesz, F., McCarley, R. & Shenton, M. (2004). White matter hemisphere asymmetries in healthy subjects and in schizophrenia: a diffusion tensor MRI study. NeuroImage, 23, 213–223.

Parker, G. J. M. & Alexander, D. C. (2005). Probabilistic anatomic connectivity derived from the microscopic persistent angular structure of cerebral tissue. Philosophical Transactions of the Royal Society B, 360, 893-902.

Parker, G. J. M., Haroon, H. A. & Wheeler-Kingshott, C. A. M. (2003). A framework for a streamline-based probabilistic index of connectivity (PICo) using a structural interpretation of MRI diffusion measurements. Journal of Magnetic Resonance Imaging, 18, 242-254.

Parker, G., Wheeler-Kingshott, C. & Barker, G. (2002). Estimating distributed anatomical connectivity using fast marching methods and diffusion tensor imaging. IEEE Transactions on Medical Imaging, 21(5), 505–512.

Pennec, X., Fillard, P. & Ayache, N. (2006). A Riemannian framework for tensor computing. Int J Comput Vis, 66, 41–66.

Pfefferbaum, A., Sullivan, E. V., Hedehus, M., Moseley, M. & Lim, K. O. (1999). Brain gray and white matter transverse relaxation time in schizophrenia. Psychiatry Res. Neuroimaging, 91, 93–100

Phillips, M. L., Drevets, W. C., Rauch, S. L. & Lane, R. (2003). Neurobiology of emotion perception II: Implications for major psychiatric disorders. Biol Psychiatry, 54, 515–528.

Pizzagalli, D., Pascual-Marqui, R. D., Nitschke, J. B., Oakes, T. R., Larson, C. L., Abercrombie, H. C., Schaefer, S. M., Koger, J. V., Benca, R. M. & Davidson, R. J. (2001b). Anterior cingulate activity as a predictor of degree of treatment response in major depression: Evidence from brain electrical tomography analysis. Am. J. Psychiatry, 158, 405-415.

Poupon, C., Clark, C. A., Frouin, V., Regis, J., Bloch, I., Le Bihan, D. & Mangin, J. (2000). Regularization of diffusion-based direction maps for the tracking of brain white matter fascicles. Neuroimage, 12, 184–195.

Regenold, W. T., Phatak, P., Marano, C. M., Gearhart, L., Viens, C. H. & Hisley, K. C. (2007). Myelin staining of deep white matter in the dorsolateral prefrontal cortex in schizophrenia, bipolar disorder, and unipolar major depression. Psychiatry Res., 151, 179–188.

Rueckert, D., Sonoda, L., Hayes, C., Hill, D., Leach, M. & Hawkes, D. (1999). Nonrigid registration using free-form deformations: application to breast MR images. IEEE Trans. Med. Imag, 18(8), 712– 721.

Rugg-Gunn, F. J., Eriksson, S. H., Symms, M. R., Barker, G. J. & Duncan, J. S. (2001). Diffusion tensor imaging of cryptogenic and acquired partial epilepsies. Brain, 124, 627–636.

Schlösser, R. G. M., Wagner, G., Koch, K., Dahnke, R., Reichenbach, J. R. & Sauer, H. (2008). Fronto-cingulate effective connectivity in major depression: A study with fMRI and dynamic causal modeling. NeuroImage, 43, 645–655.

Schwartzman, A., Dougherty, R. F. & Taylor, J. E. (2005). Cross-subject comparison of principal diffusion direction maps. Magn Reson Med.,53(6), 1423-1431.

Shimony, J. S., Snyder, A. Z., Lori, N. & Conturo, T. E. (2002). Automated fuzzy clustering of neuronal pathways in diffusion tensor tracking. Proc. Int. Soc. Mag. Reson. Med, 10, 856.

Simon, T., Ding, L., Bish, J., McDonald-McGinn, D., Zackai, E. & Gee, J. (2005). Volumetric, connective, and morphologic changes in the brains of children with chromosome 22q11.2 deletion syndrome: an integrative study. NeuroImage, 25, 169-180.

Smith, S. M., Jenkinson, M., Johansen-Berg, H., Rueckert, D., Nichols, T. E., Mackay, C. E., Watkins, K. E., Ciccarelli, O., Cader, M. Z., Matthews, P. M. & Behrens, T. E. J. (2006). Tract-based spatial statistics: Voxelwise analysis of multi-subject diffusion data. NeuroImage, 31, 1487–1505.

Sokolov, B. P. (2007). Oligodendroglial abnormalities inschizophrenia, mood disorders and substance abuse.Comorbidity, shared traits, or molecular phenocopies?. Int. J. Neuropsychopharmacol, 10, 547–555.

Steel, R. M., Bastin, M. E., McConnell, S., Marshall, I., Cunnigham-Owens, D. G., Lawrie, S. M., Johnstone, E. C. & Best, J. J. K. (2001). Diffusion tensor imaging (DTI) and proton magnetic resonance spectroscopy (1H MRS) in schizophrenic subjects and normal controls. Psychiatry Res. Neuroimaging, 106, 61–170.

Stejskal, E. O. & Tanner, J. E. (1965). Spin diffusion measurements: Spin echoes in the presence of a time-dependent field gradient. J. Chem. Phys., 42, 288–292.

Sydykova, D., Stahl, R., Dietrich, O., Ewers, M., Reiser, M. F., Schoenberg, S. O., Moller, H.-J., Hampel, H. & Teipel, S. J. (2007). Alzheimer's disease: A diffusion tensor imaging and voxel-based morphometry study. Cerebral Cortex, 17(10), 2276-2282.

Taylor, W. D., MacFall, J. R., Payne, M. E., McQuoid, D. R., Provenzale, J. M., Steffens, D. C. & Krishnan, K. R. (2004). Late-life depression and microstructural abnormalities in dorsolateral prefrontal cortex white matter. Am. J. Psychiatry, 161, 1293–1296.

Taylor, W. D., MacFall, J. R., Steffens, D. C., Payne, M. E., Provenzale, J. M. & Krishnan, K. R. (2003). Localization of ageassociated white matter hyperintensities in late-life depression. Prog. Neuropsychopharmacol. Biol. Psychiatry, 27, 539–544.

Tekin, S. & Cummings, J. L. (2002). Frontal–subcortical neuronal circuits and clinical neuropsychiatry: An update. J. Psychosom. Res., 53, 647–654.

Vago, D. R., Epstein, J., Catenaccio, E. & Stern, E. (2011). Identification of neural targets for the treatment of psychiatric disorders: the role of functional neuroimaging. Neurosurgery Clinics of North America, 22(2), 279-305.

Van der Vaart, A. (2000). Asymptotic statistics. UK: Cambridge University Press.

Vangberg, T., Kristoffersen, A., Tuch, D., Dale, A., Skranes, J., Brubakk, A.M., Larsson, H. & Harald-Seth, O. (2005). White matter diffusion anisotropy in adolescents born prematurely. Proc. Int. Soc. of Magnetic Resonance in Medicine, 296.

Wakana, S., Caprihan, A., Panzenboeck, M. M., Fallon, J. H., Perry, M., Gollub, R. L., Hua, K., Zhang, J., Jiang, H., Dubey, P., Blitz, A., van Zijl, P. & Mori, S. (2007). Reproducibility of quantitative tractography methods applied to cerebral white matter. NeuroImage, 36(3), 630–644.

Watson, G. S. & Williams, E. J. (1956). On the construction of significance tests on the circle and the sphere. Biometrika, 43, 344-352.

Whitcher, B., Wisco, J. J., Hadjikhani, N. & Tuch, D. S. (2007). Statistical group comparison of diffusion tensors via multivariate hypothesis testing. Magn. Reson. Med., 57(6), 1065-1074.

Yang, Q., Huang, X., Hong, N. & Yu, X. (2007). White matter microstructural abnormalities in late-life depression. Int. Psychogeriatr., 19, 757–766.

Yuan, Y., Zhang, Z., Bai, F., Yu, H., Shi, Y., Qian, Y., Zang, Y., Zhu, C., Liu, W. & You, J. (2007). White matter integrity of the whole brain is disrupted in first-episode remitted geriatric depression. NeuroReport, 18, 1845–1849.

Yushkevich, P. A., Zhang, H., Simon, T. J. & Gee, J. C. (2008). Structure-specific statistical mapping of white matter tracts. NeuroImage, 41(2), 448–461.

Zhang, H., Yushkevich, P. A., Alexander, D. C. & Gee, J. C. (2006). Deformable registration of diffusion tensor MR images with explicit orientation optimization. Medical Image Analysis, 10(5), 764-785.

Zhang, W., Olivi, A., Hertig, S. J., van Zijl, P. & Mori, S. (2008). Automated fiber tracking of human brain white matter using diffusion tensor imaging. Neuroimage, 42, 771–777.

Zhang, Y., Zhang, J., Oishi, K., Faria, A. V., Jiang, H., Li, X., Akhter, K., Rosa-Neto, P., Pike, G. B., Evans, A., Toga, A. W., Woods, R., Mazziotta, J. C., Miller, M. I., van Zijl, P. C. M. & Mori, S. (2010). Atlas-guided tract reconstruction for automated and comprehensive examination of the white matter anatomy. NeuroImage, 52, 1289–1301.

Zhua, X., Wanga, X., Xiaoa, J., Zhonga, M., Liaob, J. & Yao, S. (2011). Altered white matter integrity in first-episode, treatment-naive young adults with major depressive disorder: A tract-based spatial statistics study. Brain Research, 1369(19), 223-229.

Zou, K., Huang, X., Li, T., Gong, Q., Li, Z., Ou-yang, L., Deng, W., Chen, Q., Li, C., Ding, Y. & Sun, X. (2008). Alterations of white matter integrity in adults with major depressive disorder: a magnetic resonance imaging study. J. Psychiatry Neurosci., 33, 525–530.

APPENDICES

APPENDIX A

DIFFISION TENSOR IMAGING

Diffusion tensor imaging (DTI) is a magnetic resonance imaging (MRI) technique based on measuring the Brownian motion of water molecules and has been used to study white matter fiber structures of human brain in vivo. DTI has been used in discover anatomical connectivity and functional coupling between regions of the brain, as well as in clinical applications such as neurosurgery planning and brain disorder diagnosis.

DTI measures the self diffusion of water in biological tissue. Since tissue structure locally affects the Brownian motion of water molecules, DTI can identify coherent organization of tissue. Neural fiber tracts contain parallel axons whose membranes restrict diffusion, so the self-diffusion of water is most probable along the tracts. It is likely that in addition to axonal direction and myelination, other physiologic processes, such as axolemmelic flow, extracellular bulk flow, capillary blood flow, and intracellular streaming, may contribute to white matter anisotropy. Thus in DTI imagery of the brain, the local structure of the diffusion tensor can be treated as an approximation to the local neural fiber structure.

Diffusion tensor images (DTI) based on diffusion weighted images (DWI). DWI is a magnetic resonance sequence that is able to construct a probability density function (PDF) at each voxel that estimates the 3-D displacement probability of water due to diffusion along the applied magnetic gradient. DWI images contain information about the anatomy essential for quantifying white matter architecture and connectivity patterns. DWI images reveal details about the connectional and microstructural anatomy of the living human brain that are inaccessible to any other in vivo imaging modality. DTI is in fact constructed from DWI. Diffusion weighted image (DWI) volumes from six or more noncollinear magnetic gradient directions are used to construct a diffusion tensor at each voxel by modeling the diffusion PDF as an anisotropic Gaussian function. Diffusion tensor images (DTI), in particular, describe the local diffusion process or the 3D probability profile of water diffusion

in tissue using a 3×3 symmetric positive definite matrix at each voxel. As a result DTI can be regarded as low-pass, Gaussian approximation to the actual microscopic structure of the neuroanatomy, but it provides a fast and non-invasive anatomical measurement.

1.1. Basics of Diffusion:

Diffusion imaging makes use of the variability of "Brownian motion" of water molecules in brain tissue. Brownian motion refers to the random movement of molecules. Water molecules are in constant motion, and the rate of movement or diffusion depends on the kinetic energy of the molecules and is temperature dependent. Figure 56(a) shows the diffusion-driven random trajectory (red line) of a single water molecule during diffusion. The dotted white line (vector r) represents the molecular displacement during the diffusion time interval, between t1 = 0 and t2 = Δ. The displacement distribution for free water molecules is a Gaussian (bell-shaped) function. At 37°C, with a diffusion time interval of Δ = 50 msec, the characteristic distance (standard deviation of the Gaussian distribution) typically is 17 μm, which means that about 32% of the molecules have moved at least this far, whereas only 5% of them have traveled farther than 34 μm (Le Bihan, 2003). Figure 1 shows a typical displacement distribution due to diffusion in a one-dimensional model. For each displacement distance r (x-axis) there is a corresponding probability n/N (y-axis), which is the proportion of molecules within a voxel that were displaced that distance within a time interval Δ (the duration of the diffusion experiment).

In systems with a concentration gradient of diffusing molecules, diffusion leads to a net displacement of the diffusing molecules. In isotropic solutions (i.e. solutions without a concentration gradient) the probability of displacement of molecules is equal in all directions, and the mean molecular displacement is zero. The mobility of the molecules can be characterized by a physical constant, the diffusion coefficient, i.e. D. In case of a pure liquid this is also called self-diffusion coefficient. D is related to the root mean square displacement (RMS), which is the root of the mean displacement of a molecule over a given time. The Einstein relation that describes this relation in 1-D is: $RMS = \sqrt{2Dt_{diff}}$ where tdiff is the time over which the diffusion is measured (diffusion time). The diffusion coefficient is closely related to the size of molecules, and temperature (T) according to the Stokes-Einstein equation:

$$D = (kT)/f$$

in which k the Bolzmann constant, T the absolute temperature and f the friction coefficient, which depends on the size of the particle and the viscosity of the fluid. However when a container limits the diffusion, the molecules are reflected when they reach a boundary. In this situation, the diffusion distance increases linearly with the square root of time only for short diffusion times and reaches a plateau at longer

times. In biological tissues, physical barriers often restrict diffusion. These barriers can be membranes and organelles, which are generally partially permeable. This leads to an intermediate situation, where the diffusion distance increases in proportion to the square root of time (for long diffusion times), but the diffusion distances are much smaller than for free diffusion. The diffusion coefficient measured by nuclear magnetic resonance (NMR) is also called apparent diffusion coefficient (ADC). This coefficient takes into account that it is not a measure of the 'intrinsic' diffusion coefficient (D), but a coefficient that depends on the interactions of the diffusing molecule with the cellular structures over a given diffusion time. The ADC can be described as follows: $ADC = D/\lambda^2$ In this equation D is the intrinsic diffusion coefficient and λ is the tortuosity, which is a measure of the hindrance imposed by physical barriers.

Diffusion in a homogeneous medium is well described as having a Gaussian distribution. Depending on the type of molecule, the temperature of the medium, and the time allowed for diffusion, the distribution will be wider or narrower. The spread of the Gaussian distribution is controlled by a single parameter: variance (σ2). Variance, in turn, depends on two variables, so that σ2 = 2 · D · Δ, where D, the diffusion coefficient, characterizes the viscosity of the medium or the ease with which molecules are displaced. The diffusion coefficient for water at 37°C is approximately D = 3 · 10−9 m2/sec.

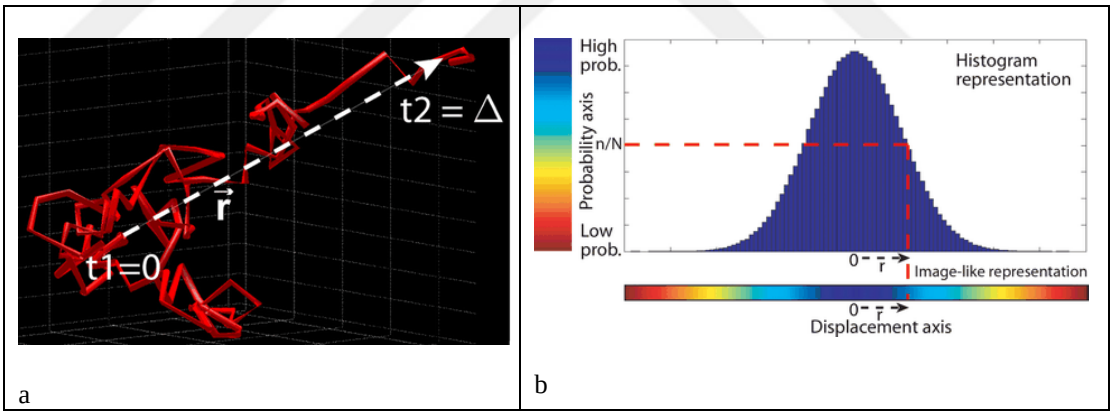

Figure 1. Displacement distribution function (Hagmann et al., 2006)

When molecules are agitated by thermal energy alone (ie, when molecular displacement takes place through the process of diffusion), the displacement distribution is centered. This means that the average or net displacement of the molecular population is zero. Factors other than heat also may contribute to molecular displacement. For example, a pressure gradient in a pipe may affect molecular displacement. In an ideal setting with no turbulence and no friction, all molecules undergo the same nonzero displacement r. However if molecules are

displaced over a nonzero average distance (by applying a pressure gradient), this type of displacement is called flux.

Biological tissues are highly heterogeneous media that consist of various compartments and barriers of different diffusivities. In terms of its architecture, a tissue can be regarded as a porous structure made up of a set of more or less connected compartments in a network-like arrangement. The movement of water molecules during diffusion-driven random displacement is affected by compartmental boundaries and other molecular obstacles in such a way that the actual diffusion distance is reduced compared with unrestricted diffusion. The characteristic of neuronal tissue is its fibrillar structure. Neuronal tissue consists of tightly packed and coherently aligned axons that are surrounded by glial cells and that often are organized in bundles. As a result, the micrometric movements of water molecules are hindered to a greater extent in a direction perpendicular to the axonal orientation than parallel to it. Consequently, molecular displacement parallel to the fiber typically is greater than that perpendicular to it. When diffusive properties change with the direction of diffusion, the dominant condition is anisotropy, and the associated displacement distribution is no longer isotropic and Gaussian, like that in unrestricted diffusion, but cigar shaped.

The synthetic generated examples are given in Figure 2. In (a) water molecules are placed within impermeable spheres that may simulate the situation a water molecule in a glass of water. The distribution is similar to that in unrestricted diffusion but narrower because there are barriers that hinder molecular displacement. The glass of water a population can be homology with semipermeable spheres with a membrane that water molecules can cross with some resistance. Such intermediate conditions will produce a displacement distribution that is not as narrow as that for a volume containing impermeable spheres but narrower than that for a volume with free diffusion. In (b) shows the diffusion probability density function within a voxel in which all the axons are aligned in the same direction. The displacement distribution is cigar shaped and aligned with the axons. It could resemble the fiber bundles of neurological tissues. The distribution may be even more complicated if the underlying tissue contains fibers with various orientations (c). The diffusion probability density function within a voxel that contains two populations of fibers intersecting at an angle of 90°. The molecular displacement distribution produces a cross shape (Hagmann et al, 2006).

Experimental evidence suggests that the tissue component predominantly responsible for the anisotropy of molecular diffusion observed in white matter is not myelin, as one might expect, but rather the cell membrane. The degree of myelination of the individual axons and the density of cellular packing seem merely to modulate anisotropy. Furthermore, axonal transport, microtubules, and neurofilaments appear to play only a minor role in anisotropy measured at MR imaging (Beaulieu C., 2002).

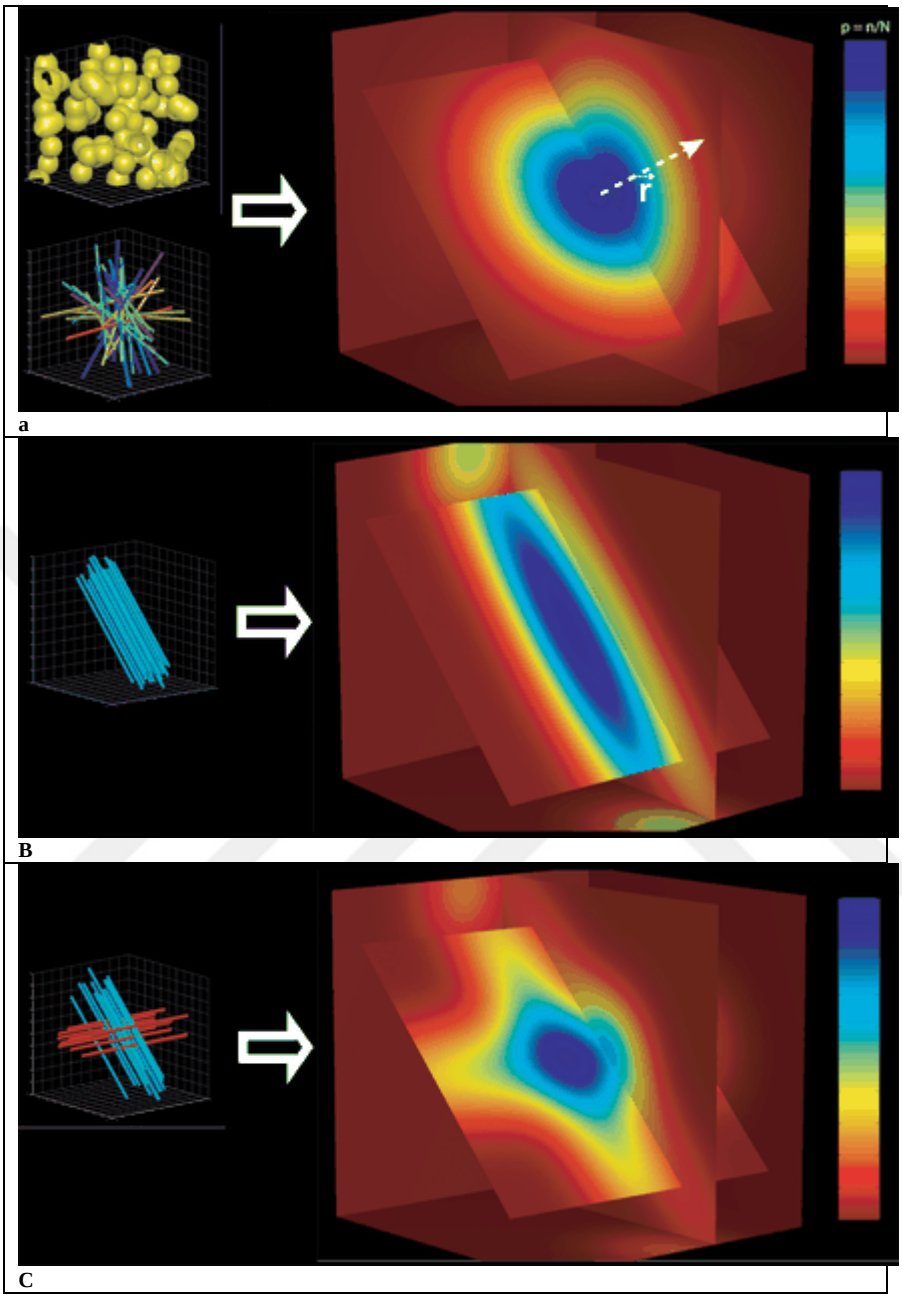

Figure 2. A synthetic Diffusion within a single voxel (Hagmann et al., 2006)

1.2. Diffusion Weighted Imaging (DWI)

To depict the displacement distribution, diffusion must be linked to the signal intensity measured at MR imaging. Under a magnetic field Bo, spinning protons undergo precession around the axis parallel to the magnetic field Bo with the rate of precession given by the Lamor equation:

$f = \gamma B_0$

in which γ is the gyromagnetic ratio in MHz/Tesla for the spin under consideration. An external 90 radiofrequency (RF) pulse alternating with Lamor frequency excites the net magnetization of the spins to lie in the transverse plane perpendicular to Bo and renders all spins coherent in phase (the excitation process). After the RF signal is turned on, the transverse component of the net magnetization decays exponentially as individual protons dephase with a relaxation time constant, T2, which varies depending on the tissue characteristics (the relaxation process). To generate the T2-weighted image, the divergence in the magnitude of tissue-specific free- induction decay of the transverse magnetization is detected. This T2-weighted imaging, as are most other structural MRI techniques, is based on the assumption that the excitation and relaxation processes of a spin occur at stationary positions, changing only in the orientation of the spin.

On the other hand, the diffusion-weighted imaging (DWI) utilizes the spin translation under the gradient magnetic field. The gradient magnetic field has both strength and direction that can be represented by a vector G (i.e., d B(x)/dx, where B(x) is the magnetic field at the location x, shown in Figure 3). The phase accumulation of a spin for time duration δ under a constant magnet field gradient G can be written as a function of the spin location x(t), as

$$\Theta = \gamma \int_0^{\delta} G.x(t)dt$$

When x(t) is stationary for the time duration δ, the phase accumulation is simply proportional to the multiplication of the magnitude of G and position xG, a projected position of x along the direction of G. When a spin moves along the direction of the magnetic-field gradient, phase accumulation becomes more complex, depending on the path x on which the spin moves. As shown in Figure 3, translation along the gradient magnetic field direction will lead a spin through a varying magnetic field. The spin will have a higher or lower precession frequency when it moves along a higher or lower field. When multitudes of spinning protons move randomly along the magnetic-field gradient, the accumulated phases of spins for a given duration will shift incoherently. The phase incoherence due to the random motion of spinning protons is detected as a decrease in the transverse magnetization signal (Hae-Jeong Park, 2005).

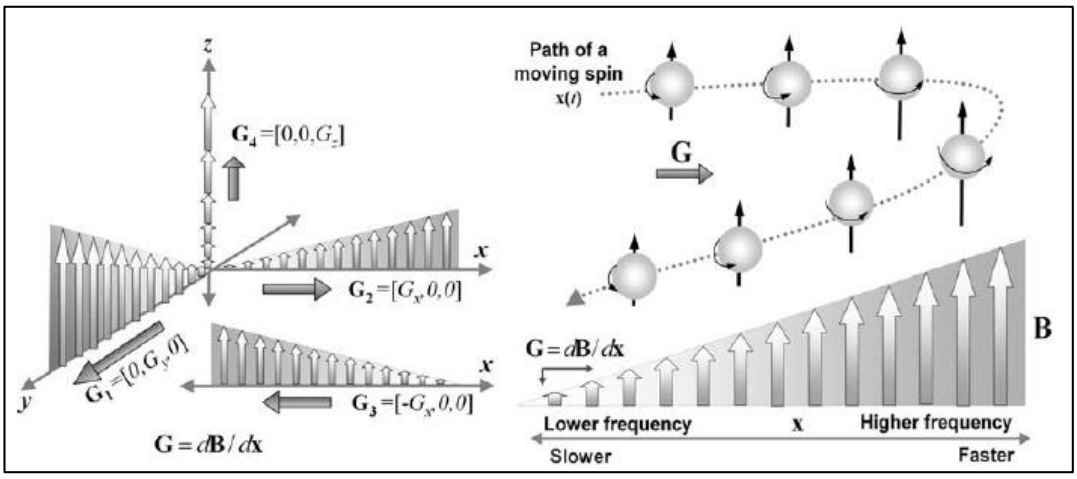

Figure 3. Nonstationary spin in the magnetic- field gradient in diffusion weighted imaging (Hae-Jeong Park, 2005)

There are various methods of DWI, but in this section only two of the most common methods will be discussed: gradient-echo DWI and spin-echo DWI. In the gradient-echo DWI two magnetic fields of identical strength and duration but of opposite directional gradients are used. As shown in Figure , after a 90o excitation RF pulse, all randomly phased stationary spins align and stay in phase under the homogeneous magnetic field. When the first gradient magnetic pulse is applied, the precession frequencies of protons depend on their location, as the strength of the magnetic field is proportional to the location of the spin. Spins in a weak magnetic field rotate slowly, whereas precession is faster in a strong magnetic field. During the time period of Δ, the phase difference between spins accumulates. When the first gradient is turned off, all spins run with the same frequency, and thus the phase difference is sustained until they experience a new gradient pulse. When the second magnetic-field gradient pulse (with the same strength and duration but in the opposite gradient direction from the first one) is applied, it will cause the spins that were rotating faster at the previous gradient field to rotate more slowly, and vice versa. At the end of the second gradient, all stationary spins will have a coherent phase, which leads to a peak signal amplitude in the receiver coil. When spins under the gradient magnetic field move along the gradient direction (lower panel of Figure 4), the spins will gain or lose the frequency according to their path. Therefore, the second gradient will not completely rephase the translating spins as a result attenuated signal of the net magnetization is detected due to their incomplete rephase.

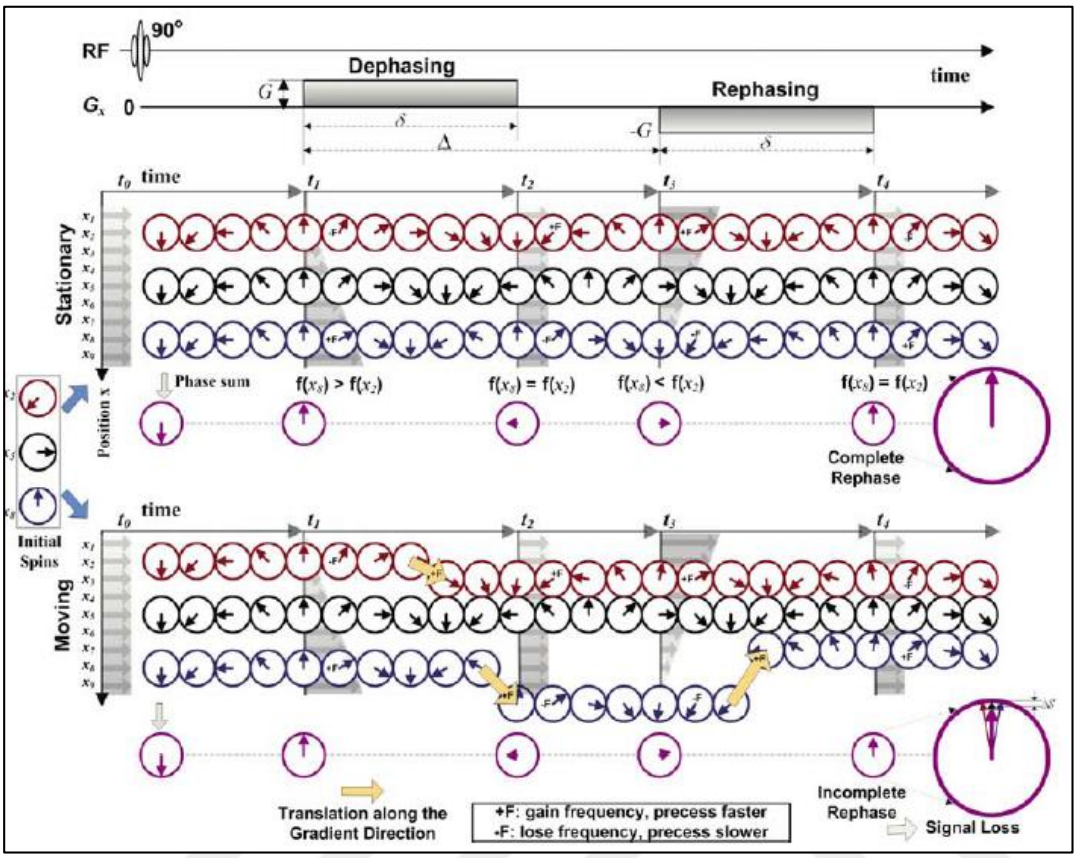

Figure 4. Gradient-Echo DWI (Hae-Jeong Park, 2005)

The spin-echo pulse sequence (Stejskal and Tanner, 1965), as shown in Figure 5, uses one strong identical diffusion-weighting gradient pulse on each side of the 180o refocusing pulse. The first pulsed gradient accumulates phase shifts for all spins, depending on their position and motion during the application of the first gradient. The 180o pulse inverts the phase of the spins, and the second gradient will induce another phase shift, thus canceling out the phase shifts for the stationary spins (the upper six spins in Figure 5). Spins that have changed positions during the time period (the lower six spins in Figure 5) will experience different phase shifts due to the two gradient pulses, and thus they will not become completely refocused. This incomplete phase realignment will consequently lead to signal attenuation.

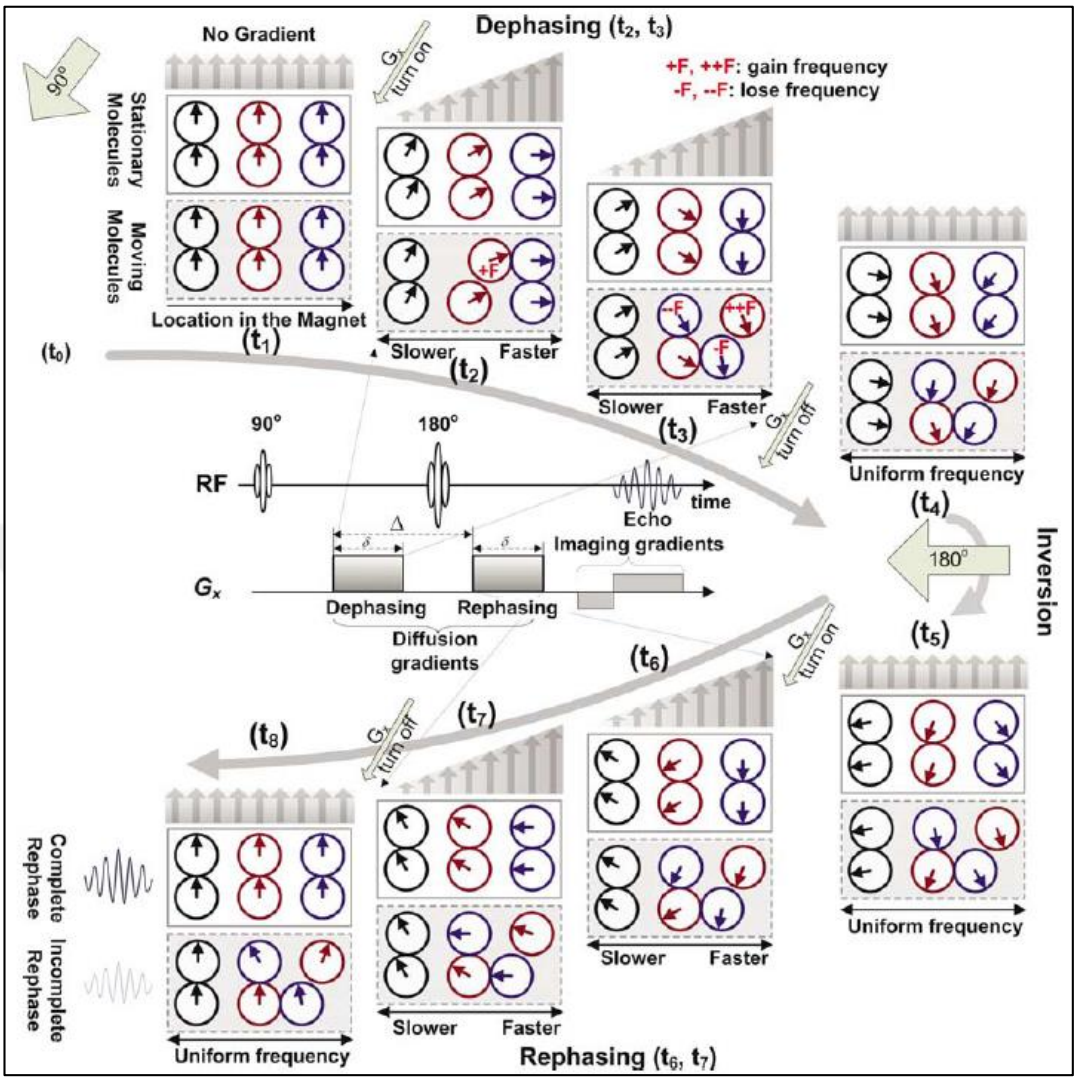

Figure 5. Spin – Echo DWI (Hae-Jeong Park, 2005)

Signal attenuation due to water diffusion can be defined by the relationship between the diffusion-weighted signal, S, and the non-diffusion-weighted signal, S0, as below (Stejskal and Tanner, 1965):

$$S = S_0 \exp(-bD)$$

$$b \cong \gamma^2 |G|^2 \delta^2 (\Delta - \frac{\delta}{3})$$

where the gradient factor, b, is determined by the diffusion-sensitizing gradient having strength |G| for the duration δ, with the time delay Δ between the two diffusion-gradient pulses. γ is the gyromagnetic ratio of proton of the water molecule (42 MHz/Tesla). The non-diffusion-weighted signal, S0, is a T2-weighted signal at

the echo time (TE), i.e., the time from RF excitation pulse to the center of the echo being received. The diffusion coefficient D reflects molecular ‘‘diffusivity’’ along the direction of the magnetic-field gradient G. Since the diffusion coefficient D, measured at a voxel can also be affected by many things like tissue perfusion, the partial volume averaging effects, and other experimental errors, mostly “Apparent diffusion coefficient (ADC)” is calculated as follows. With the previously determined b value for NMR acquisition and the measured diffusion weighted signal S, it is necessary to acquire the diffusion-weighted images with at least two different b-values. The ADC, D, can be derived from two DWIs as follows:

$$S(b_0) = S_0 \exp(-b_0 D)$$

$$S(b_1) = S_0 \exp(-b_1 D)$$

$$D = -\frac{1}{b_1 - b_0} \ln \frac{S(b_1)}{S(b_0)}$$

The ADC D is the slope representing the logarithmic difference of attenuation according to the different b-values. In practice, instead of acquiring two different b values, researchers often choose b0 to be zero, which yields S(b0) = S0, a T2-weighted image without diffusion weighting. Therefore, ADC D can be found by acquiring a DWI at a single b-value and a non-diffusion-weighted T2 reference image.

1.3. Diffusion Model (Tensor Model) Estimation

In ADC imaging, diffusion is assumed to follow a free-diffusion physical model and is described by an isotropic Gaussian distribution. This model often is too simplistic, especially if the orientation of axonal bundles is interested where the diffusion is anisotropic (not the same in all directions). A model to capture diffusion properties as well as the direction an orientation of anisotropy is needed. One of the most commonly used model fitting technique for DWI images is Diffusion Tensor Imaging (Tensor Model Estimation) which was originally developed by (Basser et al., 1996) for three-dimensional assessment of diffusion data in vivo, achieved by measurement of DWIs along at least six directional gradients. DTI is a three-dimensional technique that uses the diffusion tensor instead of a single diffusion coefficient in the DWI. Signal attenuation due to the diffusion under the magnetic-field gradient G = [Gx Gy Gz] becomes:

$$S = S_0 \exp(-b.D) = S_0 \exp(-\sum_{i=1}^{3}\sum_{j=1}^{3} b_{ij} D_{ij}), \quad i,j = x,y,z$$

Where bij = γ2δ2 (Δ – δ/3) GiGj , I,j=x,y,z for the spin-echo sequences is an element of the gradient factor matrix b. An isotropic diffusion can be derived simply by replacing the tensor matrix D with DI, i.e., the identity matrix multiplied by diffusivity D.

So the formula above can be written as;

$$\ln\left[\frac{S}{S_0}\right] = -b.D$$

Where b = [bxx byy bzz 2bxy 2bxz 2byz] and D = [Dxx Dyy Dzz Dxy Dxz Dyz], For the derivation of the diffusion tensor matrix D with six independent variables, at least six equations are required. Therefore, at least six diffusion measurements along the noncollinear noncoplanar gradient directions, plus one nondiffusion weighted measurement as the reference datum, are required in order to obtain the complete solution. There are three widely used methods used for estimating the tensor in the literature. Ordinary least squares (OLS), weighted linear least squares (WLLS) and nonlinear least squares (NLLS).

With Ordinary least squares method, ln(DWI) = ln(I0)- BmD where L is an Nx1 column vector containing the log of the diffusion-weighted intensities for each of N measurements, and B is gradient vector depends on magnitude and duration of the diffusion encoding gradients, if we write P as [Dxx Dyy Dzz Dxy Dxz Dyz ln(I0)] then L=BP and with reverse solution P=(BtB)-1BtL, which can be calculated easily.

In WLLS, D can be found from the standard linear least squares solution P =(Bt∑-1B)-1Bt∑-1L where L is an Nx1 column vector containing the log of the diffusion-weighted intensities for each of N measurements and ∑ represents the covariance matrix of the data points that are fitted. However the situation is not such simple. Due to high noise ratio (Johnson noise, Eddy currents, motion including periodic beat of CSF with blood flow, partial volume effect, etc.) The direct solution could resolve in non symmetric non positive definite matrix (with negative eigenvalues) and by the definition of tensor model, tensors must be symmetric positive definite matrix so there could be no direct solution but an estimate of it.

One of the common estimation method is gradient descent algorithm constructed as I(q) = I0 e –b(q) . D + noise where I(q) is observed value at q step. The problem reduces to finding the symmetric non-negative definite matrix D that minimizes the error functional (cost function) E(D, J) = ½ ∑ w(q) (I0 e –b(q) . D - I(q))2. Generally, estimate D, adjust through a gradient step to find new estimate for D until D converges. Construct gradient step to guarantee D is always positive definite (no negative eigenvalues). This is called nonlinear least squares (NLLS) method for diffusion weighted images.

1.4. Tractography

The fiber-tracting algorithms virtually create a trace of a particle by following the local fiber orientation as defined by the diffusion-tensor field. It is based on the assumption that local fiber orientation (for each voxel) is parallel to the major eigenvector of the diffusion tensor. A number of fiber-tracting algorithms have been developed (Basser et al., 2000; Conturo et al., 1999; Jones et al., 1999; Mori et al., 1999; Poupon et al., 2000) since the introduction of DTI.

One of the main problem of fiber tractography is smoothly connecting each discrete voxel to the adjacent one in the principal direction given by the local diffusion tensor. Jumping from one voxel to the neighboring voxel, however, may result in nonsmoothed and erroneous trajectories. To prevent the errors caused by discrete quantization of the tensor field, fiber tracking is generally conducted on the continuous representation of the tensor field. In the continuous tensor field, the trajectory and its tangent vector (i.e., the major eigenvector) can be calculated not only restrictedly at the regular discrete voxel but also anywhere in the three-dimensional continuous field, This can be accomplished through the interpolation of the tensor field using linear interpolation, Lagrange polynomials, or B-spline functions.

Although there are various methods, the overall algorithm for general fiber tractography can be constructed and given in Figure 6.

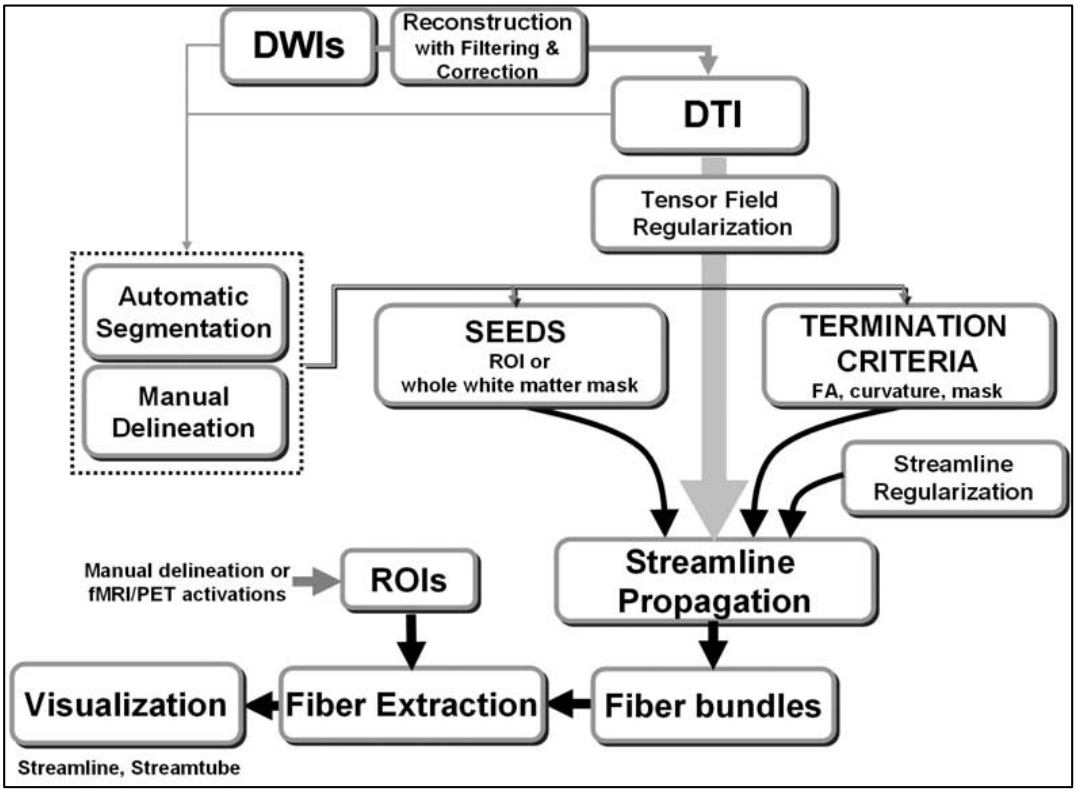

Figure 6. Diagram of general fiber tractography (Hae-Jeong Park, 2005)

1.4.1. Deterministic / Streamline Fiber Tractography

One of the most common used tractography method is deterministic / streamline method where fiber tracts can be computed by propagation of an anterograde and a retrograde streamline from an initial seed point in the direction of the major eigenvector for a small spatial step. The points on the trajectory r(s) can be derived by dr(s) / ds = v(s) where v(s) is a unit tangent vector to r(s) at the time s. With the

initial condition, r(s = 0) = r0, called the seed point, the solution for this differential equation can be derived by an iterative process: rs+1 = rs+h.vs

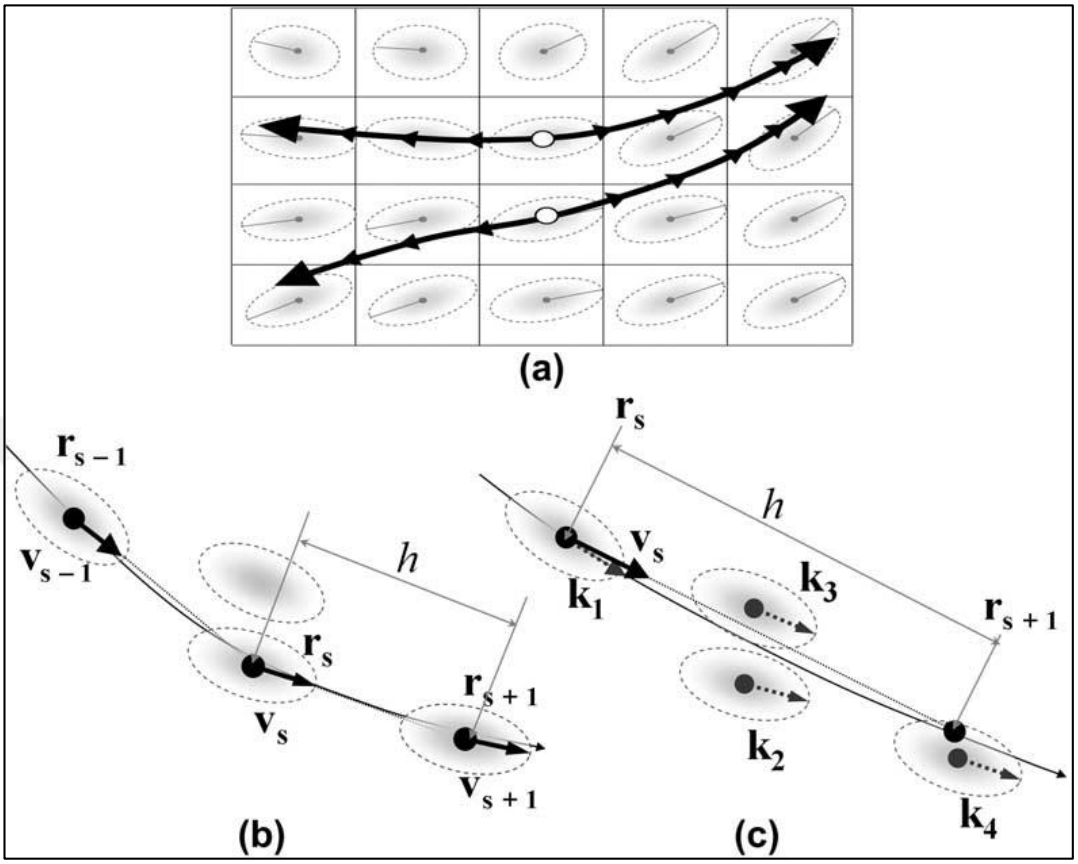

Figure 7. The basic streamline algorithms in the continuous tensor field (Hae-Jeong Park, 2005)

There are mainly two different equation solver algorithm for this equation. The simplest algorithm for solving the equation is the Euler method, which utilizes the major eigenvector as the propagation direction rs+1= rs + h.e1(rs) where e1 (rs) is the major eigenvector at point rs. The algorithm can be seen in Figure 7b. However, the Euler method can suffer from large accumulated errors unless the step h is small enough to prevent the error. The most well-known integration solver is the fourth-order Runge–Kutta method. To obtain the propagation direction, v(s), four tangent vectors at neighboring points are evaluated as can be seen in Figure 7c. once at the initial point, twice at the trial midpoints, and once at the trial endpoint.

The streamline techniques are deterministic in the sense that they utilize the eigenvector field reduced from the tensor field and do not allow for uncertainty of fiber direction. In the streamline technique, therefore, there is no mechanism to evaluate how reliably the path represents the true pathway or to evaluate how much more probable the connectivity from a seed point to a certain point is, compared to any other certain point.

1.4.2. Probabilistic / Connectivity Based Fiber Tractography

More recent approaches are statistical in nature and take into consideration all of the diffusion information with the assumption that the probability of a fiber's propagating in a given direction is proportional to the corresponding diffusion coefficient. In contrast to the streamline approach, which is a one-to-one mapping, all probabilistic approaches have in common that a single initial seed can have multiple end-points or a probability map, which makes it possible to evaluate the relative connectivity between the regions.

Fiber Tractography with Solving Diffusion Equations: Some authors try to solve fiber tractography by the help of natural diffusion calculation such as heat and fluid diffusion. These diffusion characteristics can be represented as a partial differential equation and solving them also solves the diffusion problem by finding fiber tractography by solving PDEs where the diffusion coefficients of the heat equation equal the diffusion coefficients of the diffusion tensor. The solution can be obtained by iterative simulation of a peak concentration as it diffuses inside the brain based on the heat equation (Gembris et al., 2001) or based on the heat equation with a convection term to enhance the anisotropy of the diffusion equation (Batchelor et al., 2002). Hageman et al. try to solve the problem using the dynamics of a viscous fluid described by the second-order nonlinear Navier–Stokes equations by linear partial differential equations (PDE). The Navier–Stokes equations govern flow for a viscous Newtonian fluid, a fluid whose internal stress forces are linearly related to its strain forces (Hageman et al., 2009).

Fast-Marching Tractography: Parker et al. proposes a front propagation method called fast-marching tractography wherein the interface or front propagates in the direction of high diffusibility. The variable rate of the propagation is governed by the directionality of the tensor. In the direction of the major eigenvector, e1, the front propagates faster than the direction of the other two eigenvectors, e2 and e3. The front, started at a seed point, will cross regions in the brain at different times, and this generates a map of the arrival time at all points in the brain from the seed point. From this arrival-time map, the path of connection from a seed point to any point in the volume can be calculated by finding the minimum cost path back to the seed point from that point. Although this method is performed on the eigenvector field as the streamline approach is, its one-to-many mapping is the element that provides the evaluation of relative connectivity (Parker et al., 2002).

The Monte Carlo Random-Walk Simulation: During the diffusion process, a particle performs a random walk through the medium. A Monte Carlo random-walk simulation (Hagmann et al., 2003; Koch et al., 2002) is based on this particle phenomenon with a local transition probability. The probability of transition in a given direction is chosen depending on the local diffusion coefficient along the propagation direction. The particle moves for a short time by stepping along a random direction, which is determined according to the transition probability at the initial location. In each iterative step, a new direction is randomly sampled and the

new transition-probability distribution is determined by the diffusion tensor at each location. Toward the new direction, the virtual particle propagates with a diffusivity corresponding to the direction. Particles will move with a higher probability when traveling along the fiber direction than when they travel perpendicular to it. In a number of such random walks starting from a region, the frequency that some other region has been reached can be used as a relative measure of the anatomical connectivity between the two regions. In order to constrain the random-walk process with the global properties of the fiber trajectory, hybrid approaches have been designed in order to find the optimal path between a pair of regions by combining the a priori information on the path curvature with the information from the diffusion-tensor data (Hagmann et al., 2003).

The Probabilistic Approach Using Uncertainty: Constructing the diffusion tensor from the diffusion-weighted data is a model fitting technique that tries to fit of a local diffusion model to the diffusion-weighted data at each voxel. The underlying distribution is Gaussian. However, uncertainty exists in the relationship between the diffusion measurements and the underlying fiber structures. Noise in the NMR signal can be one source of this uncertainty. Behrens et al. presented a method for the treatment of these uncertainties. They formulated the local uncertainty in the parameters of the generative diffusion model at a voxel level, in the form of posterior probability density functions on these parameters. Global connectivity is based on the probabilistic tractography, which incorporates every possible fiber orientation at every voxel with the probability given by the measured diffusion-tensor data (Behrens et al., 2003).

APPENDIX B

B-SPLINE CURVES

A B-spline curve is defined for a collection of n +1 control points $\{Q_i\}_{i=0}^{n}$ by

$$X(t) = \sum_{i=0}^{n} N_{i,d}(t) Q_i$$

The control points can be any dimension but all of the same dimension. d is the degree of the curve and $N_{i,d}(t)$ is *B-spline basis functions* , where t_i is scalar for 0 $0 \leq i \leq n + d + 1$ where $t_i \leq t_{i+1}$. t is referred as a knot.

$$N_{i,j}(t) = \frac{t - t_i}{t_{i+j} - t_i} N_{i,j-1}(t) + \frac{t_{i+j+1} - t}{t_{i+j+1} - t_{i+1}} N_{i+1,j-1}(t)$$

and it starts with

$$N_{i,0}(t) = \begin{cases} 1, t_i \leq t \leq t_{i+1} \\ 0 \quad , otherwise \end{cases}$$

The knot vector can be classified as either open or periodic. If open, the knots are either uniform or nonuniform. Periodic knot vectors have uniformly spaced knots. Uniform knots are

$$t = \begin{cases} 0, 0 \leq i \leq d \\ \dfrac{i - d}{n + 1 - d}, d + 1 \leq i \leq n \\ 1, n + 1 \leq i \leq n + d + 1 \end{cases}$$

APPENDIX C

SOURCE CODE AND INSTRUCTIONS

The source code developed in these studies has been open sourced and publicly available. Here are the repositories and descriptions for each.

https://github.com/ozermetin/DirectionalStatistics : main repository for directional statistics method

https://github.com/ozermetin/camino : forked from Camino project, additional TPDS modules are added.

https://github.com/ozermetin/automationscripts : various automation scripts for the pipeline, including some Matlab modules.

https://github.com/ozermetin/KentStatistics : repository for Kent statistics

https://github.com/ozermetin/cmp : Connectome Mapper fork

https://github.com/ozermetin/cmp_nipype: Connectome Mapper nipype plugin fork

https://github.com/ozermetin/connectomeviewer Connectome Viewer fork

https://github.com/ozermetin/VTK VTK fork

https://github.com/ozermetin/ets Enthought Tool Suite fork

https://github.com/ozermetin/Slicer Slicer fork

CURRICULUM VITAE

PERSONAL INFORMATION

Surname, Name : Metin, Mehmet Özer

Email :

EDUCATION

Doctor of Philosophy in Medical Informatics, 2018

Middle East Technical University, ANK, TR

Master of Science in Computer Engineering, 2007

Middle East Technical University, ANK, TR

Bachelor of Science in Computer Engineering, 2002

Middle East Technical University, ANK, TR

WORK EXPERIENCE

- Chief Innovation Technology Officer, Comodo Security Solutions NJ, US, 2022 – Present
- SVP Engineering, Comodo Security Solutions, NJ, US, 2019 – 2022
- VP Cyber Security Solutions, Comodo Security Solutions NJ, US, 2017 – 2019
- Director Of Enterprise and Cloud Product Development, Comodo Security Solutions NJ, US, 2014 – 2017
- Security Projects Manager, Anelarge, ANK, TR, 2008 – 2014
- Software Architect, Siemens Enterprise Communications, ANK, TR, 2007 – 2008

TEZ İZİN FORMU / THESIS PERMISSION FORM

ENSTİTÜ / INSTITUTE

Fen Bilimleri Enstitüsü / Graduate School of Natural and Applied Sciences ☐

Sosyal Bilimler Enstitüsü / Graduate School of Social Sciences ☐

Uygulamalı Matematik Enstitüsü / Graduate School of Applied Mathematics ☐

Enformatik Enstitüsü / Graduate School of Informatics ☒

Deniz Bilimleri Enstitüsü / Graduate School of Marine Sciences ☐

YAZARIN / AUTHOR

Soyadı / Surname : METIN
Adı / Name : Mehmet Özer
Bölümü / Department : Tıp Bilişimi

TEZİN ADI / TITLE OF THE THESIS (**İngilizce** / English): A TECHNICAL FRAMEWORK FOR GROUP STUDIES OF DIFFUSION TENSOR IMAGING

TEZİN TÜRÜ / DEGREE: **Yüksek Lisans** / Master ☐ **Doktora** / PhD ☒

1. **Tezin tamamı dünya çapında erişime açılacaktır. /** Release the entire work immediately for access worldwide. ☒
2. **Tez iki yıl süreyle erişime kapalı olacaktır.** / Secure the entire work for patent and/or proprietary purposes for a period of **two years**. * ☐
3. **Tez altı ay süreyle erişime kapalı olacaktır.** / Secure the entire work for period of **six months**. * ☐

** Enstitü Yönetim Kurulu kararının basılı kopyası tezle birlikte kütüphaneye teslim edilecektir. /*
A copy of the decision of the Institute Administrative Committee will be delivered to the library together with the printed thesis.

Yazarın imzası /

Tarih / Date .....
(Kütüphaneye teslim ettiğiniz tarih. Elle doldurulacaktır.)
(Library submission date. Please fill out by hand.)

Tezin son sayfasıdır. / This is the last page of the thesis/dissertation.